THE ANNALS OF "DUNAREA DE JOS" UNIVERSITY OF GALATI

Fascicle IX
METALLURGY AND MATERIALS SCIENCE

Table of Content

OBTAINING AND CHARACTERIZATION OF VITROCERAM BY CHEMICAL DOPED ZnO FOR ART MOSAIC

I. SANDU[1,2], C. BEJINARIU[3], A.V. SANDU[2,3],
V. VASILACHE[1], I.G. SANDU[3], M. BRÂNZILĂ[1]

[1]"Al.I.Cuza" University of Iaşi, ARHEOINVEST Interdisciplinary Platform
[2]Romanian Inventors Forum, Iaşi,
[3]"Gh. Asachi" Technical University of Iaşi, Science and Engineering Materials
email: sandu_i03@yahoo.com

ABSTRACT

This paper presents the obtaining and the characterization of ZnO doped vitroceramic, used as photo and termoresistive pigment for art mosaic. The coprecipitation involves two sequential steps, first of ions $Zn^{2+}_{(aq)}$, $Cr^{3+}_{(aq)}$, $Co^{3+}_{(aq)}$ and $Mn^{3+}_{(aq)}$, as oxihydroxides in predetermined molar reports: 98:0,6:0,7:06, followed by maturation, forced filtration and redispersion of the granules in distilled water, after which, by ion exchange is precipitated as intergranular film of $Sb^{3+}_{(aq)}$ and $Bi^{3+}_{(aq)}$ ions. After forced filtration and drying, the material is subjected gradually to a thermal process, according to a curve with three levels: 20 - 110℃, 110 - 360℃ şi 360 - 950℃, with a heating rate of 3℃/min., each level keeping a constant temperature while varying between 4 and 8h for nanostructures processes of crystals reform. The vitroceramic was characterized by SEM-EDX, microFTIR and termic derivatography, after treatment at 110℃ and respectively 950℃, underlining uniformity of grains and revealing their heterojonctional structure in cross-section.

KEYWORDS: vitroceramic material, pigment, mosaic, SEM-EDX, IR, microFTIR, TG/DTA/DTG/DSC

1. Introduction

Zinc oxides doped as frit pigment for artistic mozaic are polycrystalline ceramics containing minor dopants and additives [1, 2].

The zinc oxide is a synthetic white pigment used in paintings after 1834 [3].

Compared to titanium dioxide (introduced in the market for painting much later, after 1916) it has the advantage of low cost manufacturing, but compared to it and other inorganic pigments, it has an important number of disadvantages, such as low coverage degree (transparent in thin layers), variable degree of white in time under the influence of environmental factors, low photo- and temperature resistance, while as vitroceramic pigment it has a high reactivity, it induces the thermoluminescent effect and manifests incompatibility to a number of other types of metal oxide pigments.

However, as a ceramic pigment, zinc oxide has several advantages by doping the granules and their surface additive: it can be stabilized both photochemically and thermoresistively, it can get very

different stable shades, indexed CIE L*a*b* [4], can be used as a pigment for oil or water painting and also to achieve artistic mosaics and stained glass. Compared to frit pigments, particularly used to achieve polychrome based mortars finishes, mosaics and stained glass art, ceramic pigments have several major advantages: high climate and mechanical resistance, compatibility with organic and inorganic binders and glass [5, 6].

Speculating data from scientific research to get the material for ceramic varistors based on zinc oxide, there have been performed different studies on the doping processes of ZnO grains and their surface additive, in order to obtain chromophore structures with stable photochemical and thermal shades which by glazing glass process allow obtaining tessers for mosaics and stained glass, thus elaborating a first procedure for obtaining a green pigment for this purpose [5]. As in the varistor case too, the question arises to optimize the two processes: the doping and the additive.

With the only difference that in case of new vitroceramic pigments there are requirements to be

respected, to obtain uniform coloring, photo- and thermoresistance, compatible with the glass glazing performance. Since the two processes are difficult to control and vitroceramic pigments field is not sufficiently known, this paper seeks the submission of relevant information from literature used in developing technology for obtaining a varistor ceramics based on zinc oxide, in order to allow interpretation of experimental data obtained on newly synthesized vitrocerams, involving two stages: doping of zinc oxide by coprecipitation Zn^{2+}ions in mixture with other cations of transitional metals, likely forming chromophore structures, and the addition of granules resulting from coprecipitation on these structures surface of cations of block "p" metals to form uniform and continuous intergranular films, photochemically and thermal by stable and strong reactive at surface, able to interact with glass by the glazing processes.

2. Theoretical aspects on the obtaining of vitroceram

The precise role of the oxidic components of vitroceramic material used up to date in manufacturing pigments technology for art mosaic is difficult to assess [7-11]. Except for zinc oxide, considered a major phase, the others are grouped in dopants or additives. Their involvement by inserting in the crystallites structure of ZnO in these technologies clearly indicates the need to create two types of structures with different functions.

Precipitation processes by which those structures are obtained are based on two types of insertions: *subtractive* or *intercrystalline doping*, forming polychromatic phases and surface or interface (intergranular) additive, where they get into *congruents, eutectics* and *intermediate phases*. By doping, white zinc oxide turns colored, while the additive forms on the surface grain or intergranular, clusters, adductions or connecting nanostructural bridges. Hence, obtaining pigments such vitroceram likely to be further glazed on glass, requires two sequential processes: first, a doping one to form chromophore groups, then the surface additive one, to form the reactive film with a dual role: stabilization of the chromophore and glazing.

E.g., for the green pigments, the first obtained are the doped ZnO grains, mainly with MnO and CoO, after which they are submitted to Bi_2O_3 and Sb_2O_3 additive, forming the intergranular film reactive to the subsequent glazing process. Manganese and cobalt oxides bring back the color of zinc oxide granules by producing photochemical by and thermally stable chromophore structures [8, 12, 13], while those of bismuth and antimony supply uniform distribution, continuity and density of intergranular film,

allowing stabilization of chromophores and glazing [7, 12]. As seen, the role of doping and of the additives is largely evident, but the processes taking place in the two stages of production: the precipitation/polymerization and the calcination/sintering/vitrifying, are much more complex, develop different crystalline, eutectic and congruent phases, technologically unmanageable.

It is known that zinc oxide is a very poor type "n" extrinsic semiconductor, that by doping with block "d" metal oxides from the center of the first series of transition in stable oxidation states (Cr_2O_3, MnO, Fe_2O_3, CoO, NiO), becomes electronically conductive by populating with electrons the Additional Donor Band (ADB), the thermoluminescent effect being diminished.

On insertion by additive of thus obtained granules with oxides of block "p" (Bi_2O_3, Sb_2O_3, PbO, SiO_2), a series of polycrystalline dielectric structures result, with electron depletion of the additive band, transforming it into an Additional Acceptor Band (AAB) and taking a big distance from the Valence Band (VB), allowing their glazing and bindering on the glass. Furthermore, the low voltage resistivity increases due to $ZnO-Bi_2O_3$ eutectic formed after sintering/vitrifying processes at temperatures above 750°C [14] that allow stabilizing of the shade and fading of the thermoluminescent effect. As Bi_2O_3 is non-dispersible in ZnO at room temperature coprecipitation processes, it will segregate, be on the surface of a ZnO grain, or at interface between two ZnO grains, having the shape of an amorphous 1-2 nm film rich in bismuth oxide [15]. Previous studies [1, 2, 5, 16-19] showed that the distribution, uniformity and granulometry of polycrystalline structures on the surface of the doped zinc oxide granules depends on bismuth oxide content, which increases the film grain, leading to its discontinuity.

In contrast, antimony oxide, which is a grain growth inhibitor, forms with zinc oxide spinels and pirochlore type phases at the grains surface, which provides continuity and uniformity to the intergranular film [20-22]. Thus, antimony oxide serves to bind the granules of zinc oxide and allows, when obtaining tessers for mosaics or stained glasses art, vitroceramic pigment adhesion to glass surface by glazing.

Regarding the transitional metal oxides, the cobalt and manganese have a well known role in granules of zinc oxide coloration [5, 7, 10]. These oxides are dispersable in ZnO solution, as they are kinetic and thermodynamic compatible, having the same oxidation state (II). Both cobalt oxide and the manganese one are colored materials, that allow the sintering to give chromophore structures with zinc oxide. Very important for ceramic pigments used in the mosaics and stained glass, is the distribution and

uniformity of colored granules, but also the intergranular film thickness and continuity [5].

It is absolutely necessary that both phases - precipitation/polymerization and the sintering/vitrifying one, at the most lowest temperature, give optimal distributions of colored microgranules and intergranular films. An important role in structural reform of intergranular polycrystalline film in the sintering/vitrifying processes have the spinel structures and pirochlore type phases that inhibit granules growth and compactize them at temperatures higher than 950°C [7], up to 1100°C [5].

Previous studies [21, 22] focused on the role of certain dopants concentration on certain tinctorial and thermoluminescent properties. It was noted that doping achieved through colloidal milling physical processes is effectively lower at the sintering-vitrifiying, while the one achieved by the processes of precipitation / polymerization remains constant [7, 23]. A comparative analysis of the transitional metal oxides behavior used in doping processes in terms of kinetic and thermodynamic compatibility with zinc oxide, which is typical amphoter, taking into account the three types of reactivity: acid-basic (which is dominant), complexing and redox, allow their grouping in the following alkalinity series: $CrO>MnO>FeO>CoO>NiO$; Mn_2O_3 (weak basic)$>Cr_2O_3$ (amphoteric)$> Fe_2O_3$(very weak acid)$>Co_2O_3$(weak acid)$>Ni_2O_3$(weak acid).

These series allow assessing the stability of double, mixed or saline oxides likely to appear at the precipitation or the sintering/vitrifying precesses. Thus, the next two double oxides are very stable: Fe_3O_4 (feroferic oxide, $FeO.Fe_2O_3$) and Mn_3O_4 (manganomanganic oxide, $MnO.Mn_2O_3$) and three saline oxides: $ZnCr_2O_4$, $ZnNi_2O_4$, $ZnCo_2O_4$, followed by the less stable, saline oxides type: $ZnMn_2O_4$ (coming from amphoteric oxide and a very weak basic one) and $ZnFe_2O_4$ (derived from an amphoteric oxide and a very weak acid) and then the unstable ones, double oxides type: Cr_3O_4, Ni_3O_4 and Co_3O_4. If during the processes of precipitation only the very stable are formed, the sintering-vitrifying processes are also likely to form some less stable oxides. It is interesting that some occur in the precipitation phase, but disappear at sintering-vitrifying, or vice versa, are formed at high temperatures, but reversible change at the cooling in primary byproducts occurs.

Since the kinetics of these processes is much more complex, further there are introduced some issues from the specialized literature related to the interactions that take place in the two phases, the precipitation and sintering-vitrifying, having carefully formed components and structural features of intergranular films.

Together with the formation of zinc oxide doped particles, their surface resulting in a series of congruents spinel $Zn_7Sb_2O_{12}$ type and pyrochlore type phases, bismuth oxide-rich in the form of 1-2 nm thick intergranular films. Moreover, to highlight the role of oxides in the two processes, besides the main components for doping (CoO and MnO) and the additive (Bi_2O_3 şi Sb_2O_3), were used in small quantities other transition metal oxides too, stable in +III oxidation state, such as Cr_2O_3 [16], Fe_2O_3, Co_2O_3 and Ni_2O_3 [20], giving rise in precipitation to ZnO interactions, somewhat different of oxides in the oxidation state +II. They interact better with zinc oxide in sinterizing-vitrifying. Thus, thermal processes enable a series of reactions leading to congruents and different polycrystalline phases [8]. Final composition of the final microstructure depends on the existence and development of such reactions occurring in sintering and vitrifying, and also on selecting an optimal strategy for achieving a structure with exactly the tinctorial and bindering desired properties [28]. It is known that hue and bindering capacity by glazing is directly proportional to the average grain size of ZnO [29, 30]. It is therefore necessary a rigurous control of microstructural development degree of conductive grains and intergranular film, both in precipitation stage and in the sintering-vitrifying one. In 1975, *Wong* [31] first suggested a possible reactions sequence involving formation of a pyrochlore-type compound $Bi_2(Zn_{4/3}Sb_{2/3})O_6$. At higher temperatures, this phase reacts with ZnO pellet, which is easily accessible in the matrix bulk, to form a spinel-type compound and a liquid phase rich in bismuth oxide. So, zinc oxide replaced in pyrochlore an equivalent amount of bismuth oxide, without disrupting the substructure ($Zn_{4/3}Sb_{2/3}$), according to the reaction:

$$Bi_2(Zn_{4/3}Sb_{2/3})O_6 + ZnO \rightarrow Zn(Zn_{4/3}Sb_{2/3})O_4 + Bi_2O_{3(liq)} \qquad (1)$$
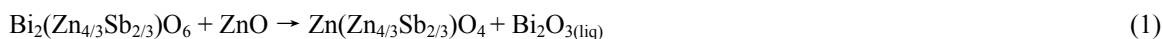
The presence of liquid phase leads to film densification, zinc oxide grain is reduced and spinel formed will act as grain growth inhibitor [16].

Later, in 1980, *Inada* [32] proposed a similar sequence of reactions in two stages, that occurs in a ternary oxide system, first at temperatures below 900°C and the second, between 900°C to 1050°C, according to the following reactions:

$$2ZnO + 3/2Bi_2O_3 + 3/2Sb_2O_3 + 3/2O_2 \rightarrow Zn_2Bi_3Sb_3O_{14} \qquad (2)$$
$$2Zn_2Bi_3Sb_3O_{14} + 17ZnO \rightarrow 3Zn_7Sb_2O_{12} + 3Bi_2O_{3(liq)} \qquad (3)$$
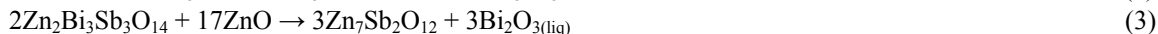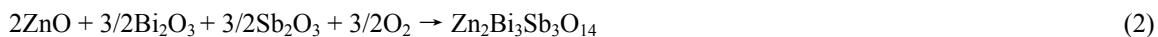
According to Inada, the reaction (3) is reversible on cooling, although the presence of certain doping, as the oxides of Cr, Mn, Co and Ni, tend to stabilize the spinel structure and to prevent their decomposition in pyrochlore type phases. There is a disagreement between the chemical composition of pyrochlore-type phases proposed by Inada and suggested by Wong. Prevalence of the first reaction was confirmed in 1989 by *Kim et al.* [33] and recently reaffirmed by *Mergen & Lee* (1997) [34]. *Kim* states that both the binary systems of reaction (ZnO-Sb$_2$O$_3$ and ZnO-Bi$_2$O$_3$), and the ternary (ZnO-Sb$_2$O$_3$-Bi$_2$O$_3$), allow dielectric film densification, being closely related to the formation of pyrochlore type phases and the liquid ones (eutectic).

A very important role plays the relationship between the Sb oxide and Bi oxide. For Sb$_2$O$_3$/Bi$_2$O$_3$ = 1, it will correspond to stoechiometry of pyrochlore phase formation.
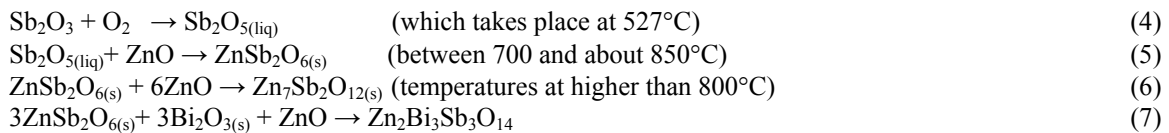
A ratio greater than unity leads to the formation of liquid phases (around 740°C), as a result of interaction between ZnO and Bi$_2$O$_3$ with formation of eutectic [33, 35]. On the other hand, a lower ratio than 1 delays eutectic liquefaction at higher temperatures, up to pyrochlore phase decomposition (reaction 3).

Based on previous studies from the 1990s on the influence of nature and the doping concentration, of sintering-vitrifying temperature, of heating and cooling rates on the development and microstructural reform of vitroceram, *Olsson* [5] suggested the existence of an additional reaction that explains the increasing of volumetric fraction for spinelic structures at Sb$_2$O$_3$/Bi$_2$O$_3$ ratios > 1.

In 1996, *Leite et al.* [37] proposed the following sequence of reactions to explain the role of additives in the formation of intergranular dielectric film:

$$Sb_2O_3 + O_2 \rightarrow Sb_2O_{5(liq)} \qquad \text{(which takes place at 527°C)} \tag{4}$$
$$Sb_2O_{5(liq)} + ZnO \rightarrow ZnSb_2O_{6(s)} \qquad \text{(between 700 and about 850°C)} \tag{5}$$
$$ZnSb_2O_{6(s)} + 6ZnO \rightarrow Zn_7Sb_2O_{12(s)} \text{ (temperatures at higher than 800°C)} \tag{6}$$
$$3ZnSb_2O_{6(s)} + 3Bi_2O_{3(s)} + ZnO \rightarrow Zn_2Bi_3Sb_3O_{14} \tag{7}$$

The last sequence takes place at temperatures between 700°C and 900°C.

Based on previous work of *Kim et al.* [36] and *Krasevec et al.* [38], who suggested a mechanism of evaporation-condensation of antimony oxide at about 500°C, *Leite et al.* [37] proposed that at first Sb(III) oxide is oxidised to Sb(V), which is liquid at this temperature. Further, pentoxide vaporizes, and the vapors condense over ZnO solid particles to form intermediate phases of rutile type, ZnSb$_2$O$_6$. Such a phase, whose existence was mentioned above by

Inada[32] and *Kim et al.* [33], and, then reacts with ZnO adjacent particles to form spinel structures or with ZnO and Bi$_2$O$_3$, when appear the pyrochlore phases, which later transform into spinels (reaction 3). However, the presence of oxide of Sb(V) is controversial because the compound decomposes at around 380°C, releasing oxygen.

Thus, *Ott et al.* [22] and *Kumari et al.* [39] rejected this hypothesis and rewrote reactions (4) and (5) into a single one:

$$ZnO + Sb_2O_3 + O_2 \rightarrow ZnSb_2O_{6(s)} \text{ (which takes place between 600 and 800°C)} \tag{8}$$
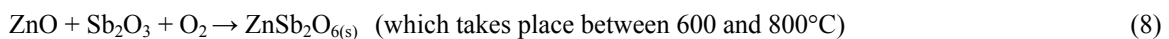
Ott et al. have noted, however, the presence of spinel structures ZnSb$_2$O$_{6(s)}$ is unclear, since the

direct reaction itself could explain the additional formation of spinel [22], according to the process:

$$7ZnO + Sb2O3 + O2 \rightarrow Zn_7Sb_2O_{12(s)} \text{(at temperatures above 800°C)} \tag{9}$$
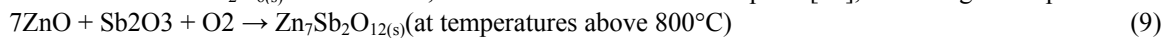
This option was rejected by *Kumari et al.* [39], who proposed the following rection taking place in the binary system:

$$ZnO + Sb_2O_3 + O_2 \rightarrow ZnSb_2O_{6(s)} \text{ (temperatures at higher than 600°C)} \tag{10}$$
$$ZnSb_2O_{6(s)} + 1,33ZnO \rightarrow Zn_{2.33}Sb_{0.67}O_{4(s)} + 0,67Sb_2O_3 + 0,67O_2 \tag{11}$$
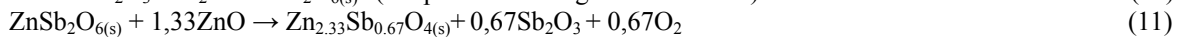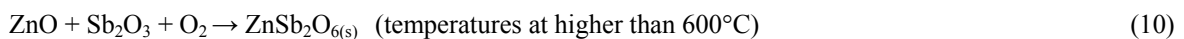
Reactions that would take place at temperatures above 800°C, whereas that after 900°C a structural

reform should take place, according to the reaction:

$$3Zn_{2.33}Sb_{0.67}O_{4(s)} \rightarrow Zn_7Sb_2O_{12(s)} \tag{12}$$

By trimerizing Zn2.33Sb0.67O4$_{(s)}$, which is nestoechiometric, it results a stoichiometric spinel structure, corresponding to the formula Zn$_7$Sb$_2$O$_{12(s)}$, but with a cubic symmetry instead of an orthorhombic

one. Spinel transformation could be avoided by the presence of some soluble additives.

Reactions from (1) to (12) are some of the proposals in the specialized literature to explain the

formation of the intergranular film during the sintering-vitrifying process.

Lack of accurate descriptions of the entire vitroceramic manufacturing process has imposed the writing of this paper, focused primarily on highlighting the phenomena that occur both in the precipitation-polymerization processes and at the sintering-vitrifying, taking into account the formation from pure oxides of eutectic type phases, pyrochlore, spinel and intermediate phases.

3. Experimental Part

Chemical Analysis

A newly synthesized product was analyzed by classical chemical methods, determining by mass atomic spectroscopy the metal cations as key components on the basis of which the composition of oxides was calculated. Hygroscopic and chemically bound water was determined by gravimetric methods, subjecting the sample to a static heat treatment. This correlates, as we shall see, with data obtained by thermal derivatography.

SEM-EDX

The researches have been carried out with a SEM VEGA II LSH scanning electronic microscope manufactured by the TESCAN Co., the Czech Republic, coupled with an EDX QUANTAX QX2

detector manufactured by the BRUKER / ROENTEC Co., Germany.

TG/DTA

In the thermal analysis was used a Thermobalance Linseis STA PT1600, which allows fast heating and cooling rates as well as a highly precise temperature control. The temperature range was from 20 to 1000°C. The device is fully controlled by computer.

Micro-FT-IR and IR

The spectra have been recorded with a FT-IR Spectrophotometer coupled to a HYPERION 1000 microscope, both pieces of equipment from Bruker Optic, Germany.

FT-IR spectrometer is a TENSOR 27, which is an advanced flexible bentchtop instrument suitable for routine applications as well as laboratory research. TENSOR 27 is designed for measurements mainly in the mid – infrared region.

The IR spectra have been recorded with a IR Spectrophotometer SPECORD M, between 200 – 4000 cm^{-1}, information correlated to spectra obtained by microFTIR.

4. Results and Discutions

The pigment of vitroceramic type, newly synthesized, with green-pale color, was first characterized by chemical analysis (Table 1).

Table 1. *Data on the chemical composition of newly synthesized vitroceramic*
Chemical compozition in main components as oxide

Chemical compound, (%)		Samples I	Samples II
ZnO	Theoretical	87.77	88.55
	Practical	87.752	87.932
MnO	Theoretical	0.77	0.62
	Practical	0.760	0.617
CoO	Theoretical	1.63	1.23
	Practical	1.606	1.221
Cr_2O_3	Theoretical	1.65	1.33
	Practical	1.628	1.309
Sb_2O_3	Theoretical	3.14	3.17
	Practical	3.106	3.148
Bi_2O_3	Theoretical	5.05	5.10
	Practical	4.991	5.059
$H_2O_{(higroscopic)}$	Theoretical	-	-
	Practical	6.964	0.586
$H_2O_{(chimic)}$	Theoretical	-	-
	Practical	1.193	0.117

Samples I – pigment after precipitation stage with ammonia solutions;
Samples II – pigment sintering and vitrifying stage.

By comparing the theoretical ratio of main components with the chemical analysis data, these results allowed a confirmation, so that it was achieved the total coprecipitation of all chemical compounds,

the values obtained by chemical analysis being very close to the theoretical ones.Product composition in the two stages of processing does not differ greatly, the only component that has wide variations being the

water under the two forms, hygroscopic or physically bound water and the constitution water or chemically bound water.

Therefore, the product was further characterized by SEM-EDX, IR spectroscopy and thermal derivatography.

a   *b*
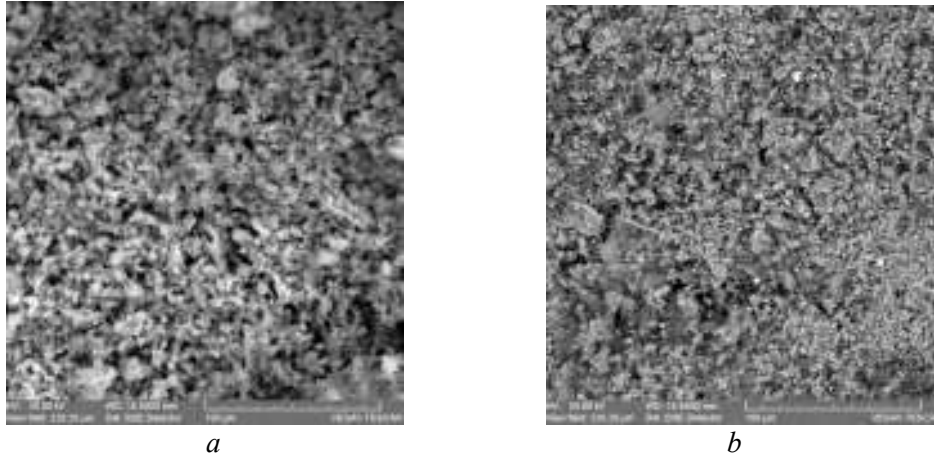
Fig.1. *SEM image of newly sinthesized vitroceram, 1000X BSE:*
a – before vitrifying-sinterizing; b – after vitrifying-sinterizing.

a

b
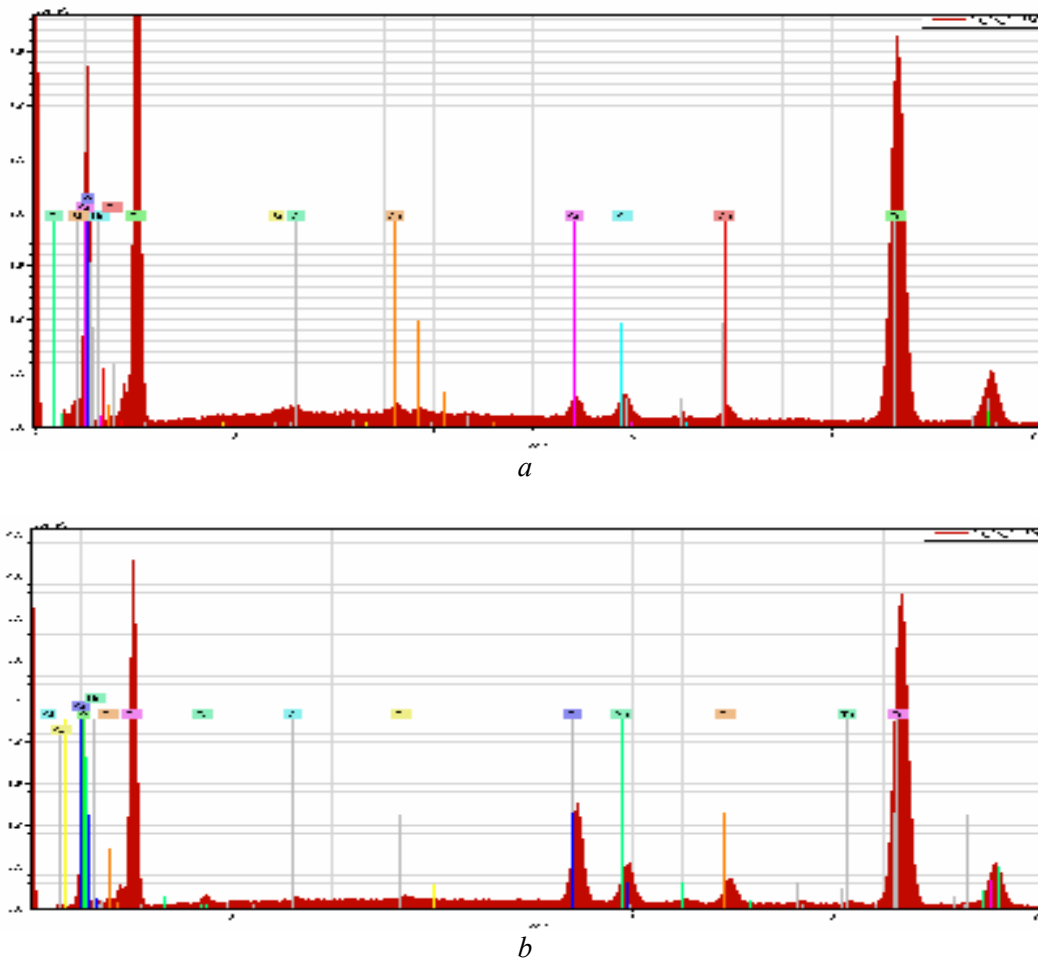
Fig.2. *EDX Spectra of newly sinthesized vitroceram:*
a – before vitrifying-sinterizing; b – after vitrifying-sinterizing.

Table 2. *Composition of the vitroceramics: left table is after precipitation*
and right table is the composition of a bluk of doped ZnO

Element	Weight, %	Atoms, %	Error in %
Zinc	64.58572	37.09885	1.849272
Oxygen	25.02373	58.74673	7.219001
Manganese	1.11221	0.760413	0.079453
Chromium	1.415505	1.022532	0.091944
Cobalt	1.201922	0.76604	0.068493
Antimony	1.396885	0.430925	0.084291
Bismuth	5.004422	0.899464	0.212932
Chlorine	0.259606	0.275043	0.043605

Element	Weight, %	Atoms, %	Error in %
Zinc	66.32515	40.41063	1.777766
Oxygen	19.62508	48.86934	3.40265
Chromium	9.136397	7.000575	0.292687
Cobalt	2.843064	1.922008	0.110038
Manganese	1.155598	0.838036	0.103717
Chlorine	0.386475	0.434311	0.046599
Calcium	0.52823	0.525105	0.048067

The thermogravimetric analysis took 100 mg of product, very finely crushed, dried in oven at 110±5°C for 4 hours and then subjected to dynamic thermal analysis. Figure 3 presents the derivatograma of the product.

Fig.3. *Derivatogram of the vitrified-sinterized product*

Table 3. *Data on the nature of thermal effects on temperature ranges*

Product	Temperature ranges (°C)	Nature of the dominant thermic effect	Charateristic temperature (°C)
G(I)	30-110	exothermic	max. at 70
	110-210	highly exothermic	max. at 170
	210-240	highly endothermic	min. at 220
	240-400	exothermic	max. at 270

From Figure 3 and the corresponding data listed in Table 3 for the newly synthesized product, after vitrifying-sintering stage, the following conclusions:

- On heating under dynamic can be drawn, it has up to 110°C, a thermal process with a dominant weak exothermic effect, corresponding to the elimination of ammonia and of reversible hygroscopic water (the sample was heated at 110±5°C, hydroscopic water coming from the residual and the reversible water, taken after the initial thermic treatment) and of a quantity of oxygen absorption from the atmosphere; so, in this area, specific mass loss (0.18%) corresponds to the three processes: dehydration, ammonia elimination and oxygen uptake;

- Over 110°C, the product has a highly exothermic effect at 170°C, when it is eliminated a portion of the crystallization water and the coordinative;

- Endothermic dominant processes corresponding to the disposal of constitution water (of the OH groups and of those of coordinating left) are found at 220 ºC;

- Last highly exothermic effect corresponding to crystalline reforming processes, takes place at 270°C, attributed to the fact that the product structure shows a higher concentration of congruent structures of spinel type, with high thermal stability;

- Thermal analysis under dynamic which shows that coprecipitation procedure in ammonia system allows redistribution phase at high temperatures, thus creating optimal conditions to achieve eutectoid of oxides of antimony and bismuth, as a dispersion medium for spinel grains.

- In Figure 4 there are comparative spectra IR of the newly synthesized product after precipitation and drying stage, when the product is white-gray-brown (thick curve) and respectively after step by step treatment of calcination and sintering at 1200°C, when the product is pale green (thin curve).
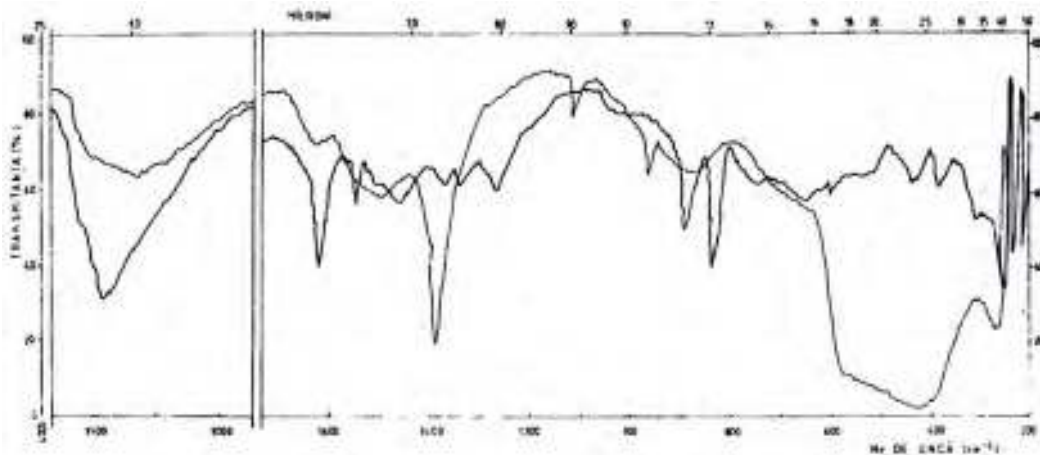
Fig. 4. *IR spectra for the product G(I): thick line – product after precipitation and drying stage; Thin line – product after calcination-sinterizing.*

To characterize these products by IR spectroscopy were used characteristic group vibrations of the main structural components, in particular groups: Zn(II)-O, Zn(II)-OH, Mn(II)-O, Mn(II)-OH, Co(II)-O, Co(II)-OH, Cr(III)-O, Cr(III)-OH, with Bi(III)-O and Sb(III)-A [171, 195, 198, 199, 292 and 293].

If the oxidic systems of the cations of Zn(II), Mn(II), Co(II), Cr(III) have a few crystalline changes, very stable, oxides of Sb(III) and Bi(III), presents a more complex allotropy, whose stability depends on the summative oxidic system in which it takes part. Because they are easily fusible oxides, other oxides are dispersed by physical and chemical processes, when congruent hardly fusible structures are formed,.

From IR spectra, stands some specific features major phase, zinc oxide (Table 4).

It should noted that the product analyzed after precipitation and drying has representative characteristic group frequencies in the 3380-3430 cm-1 range, specific to each type of water, those at 1380cm^{-1} and 250cm^{-1}, corresponding hidroxocomplexes of transition metals, in exchange, the same products after the sintering stage, are subjected to changes of absorption bands in fields 380-440 cm^{-1}, 500-570 cm^{-1}, 1380 cm^{-1} şi 3380-3440 cm^{-1}. It should be noted that there is a clear difference between the spectra produced in the two stages: precipitation and calcination-sintering. At first, there also are shown the corresponding bands to amino complexes, the thick line spectra (1620-1630 cm^{-1}, 830 cm^{-1} şi 860-880 cm^{-1}), which are strongly attenuated in the process of calcination.

Table 4. Characteristic group vibrations –specific to diverse structural units

Chemical Compound	Characteristic frequency showed like wave numbers (cm^{-1})
ZnO	230 420-450-500 1380
MnO	350 405-420 660
CoO	220 390-460 590 670
Cr_2O_3	320 530 650-670
Sb_2O_3	212 390 540
Bi_2O_3	260 505 1480-1520 1550

In conclusion, IR spectra show the presence of two groups of oxide systems, transition hardly fusible metals and fuses easily fusible of Sb and Bi, which after sequential coprecipitation process in ammonium hydroxide medium originally formed some type of coordinative oxiammino or oxihidroxidice species, which after the gradual thermal processes, lead to elimination processes of volatile components (water and ammonia), segregation, diffusion and microstructural reform, resulting multicomponent dispersed phase, thermally and photochemically stable.

5. Conclusions

New vitroceramic material was synthesized to help obtaining tessers for mosaic and stained by single or double glazing [6]. Through chemical analysis, combined with SEM-EDX data, the thermogravimetric and IR spectrocopy, coprecipitation process revealed that the ammonia system allows redistribution phase at much higher temperatures, and the pigment has a uniform particle size, coloration and coverage of high power, high chemical, thermal and photo resistance, with good preservation of color over time. This pigment has a color degradation rate (shift to grey), very low compared with other green mineral pigments as chromophore groups form intragranular and intergranular film which stabilizes the color and protects it photochemically and thermally.

References

[1]. **A.V. Sandu, V. Vasilache,, I. Sandu, M. Saviuc, I.G. Sandu, I.M. Popa** - „*Obtaining and Characterisation of Thermoresistive Pigments*", in International Scientific Conference UGALMAT 2009 (Advenced Materials and Technologies), vol. II, Ed. University Press GUP (ISSN 1843-5807), Galaţi, 2009, p. 470-474;

[2]. **I. Sandu, M. Saviuc, I.G. Sandu, I.M. Popa, A.V. Sandu,** *Thermoresistive New Pigments for stained glass and mosaics*, in Proceeding of the IVth International Simposium Cucuteni 5000 Redivivus – Exact and Less Exact Sciences, Ed. Pim (ISBN 978-606-520-664-9), Iaşi, 2009, p. 163-177;

[3]. **I. Sandu, I.C.A. Sandu şi A. van Saanen** - *Scientific Expertize of the Art Works,* vol I, ."Al.I. Cuza" University Publishing House Iaşi, (ISBN 973-9272-21-5),1998, p.436;

[4]. **I. Sandu, I.C.A. Sandu, I. G. Sandu,** *Colorimetry in Art*, Ed. Corson, Iaşi, (ISBN 973-8225-28-0), 2002;

[5]. **I. Sandu, T. Bounegru, I.G. Sandu, A.Alexandru, I.C.A. Sandu, F. Diaconescu, A.V. Sandu** - „*Process for obtaining a green, opaque, photo- and thermoresistant pigment*", Patent MD3296G2/30.04.2007 (AGEPI File a2006-0178/21.06.2006, Owner the State University of Kisinew);

[6]. **V. Moraru, I. Sandu, C. Moraru, I.C.A. Sandu, I.G. Sandu** - „*Process for Manufacturing Polychrome Tesserae and Use Thereof for Producing Wall Mosaic*", Patent RO118.415/3/155/28.03.2003 (OSIM File nr. A00988/2001, Owner the Authors);

[7]. **C.-C. Lin, W.-S. Lee, C.-C. Sun, W.-H. Whu** - "*The Influences of Bismuth Antimony Additives and Colbalt Manganese Dopants on the Electrical Properties of ZnO-Based Varistors",* Composites Part B: Engineering, 38, 3, MAR 2007, 338-344;

[8]. **M. Peiteado, M.A. de la Rubia, J.F. Fernandez, A.C. Caballero** - "*Thermal Evolution of ZnO-Bi2O3-Sb2O3 System in the Region of Interest for Varistors",*Journal Material Science (J. Mater. Sci.), 41, 8, APR2006, p.2319-2325;

[9]. **M. Matsuoka** - "*Nonohmic properties of zinc oxide ceramics*", Jap. J. Appl. Phys., 10, 6, JUN1971, 736–46;

[10]. **G.S. Snow, S.S. White, R.A. Cooper, J.R. Armijo** - *"Characterization of high field varistors in the system ZnO–CoO–PbO–Bi$_2$O$_3$"*, Ceramic Bull., 59, 6, JUN1980, 617–22;

[11]. **S.N. Bai, J.S. Shieh, T.Y. Tseng** – *"Characteristic analysis of ZnO varistors made with spherical precipitation powders"*, Mater. Chem. Phys., 41, 1995, 104–109;

[12]. **R.G. Dosch, B.A. Tuttle, R.A. Brooks** - *"Chemical preparation and properties of high-field zinc oxide varistors"*, J. Mater. Res., 1, 1986, 90–99;

[13]. **J. Wu, C. Xie, Z. Bai** - *"Preparation of ZnO-glass varistor from tetrapod ZnO nanopowders"*, Mater. Sci. Eng. B., 95, 2002, 157–61;

[14]. **R.J. Lauf, W.D. Bond** - *"Fabrication of high-field zinc oxide varistors by sol-gel processing"*, Ceramic Bull., 63, 2, FEB1984, 278–81;

[15]. **M. Elfwing** - *"Novel powder-coating solutions to improved microstructures of ZnO based varistors, WC-Co cutting tools, and Co/Ni nano phase films and sponges"*, Acta Universitatis Upsaliensis, 2002;

[16]. **E. Olsson, G. Dunlop, R. Osterlund** - *"Development of functional microstructure during sintering of a ZnO varistor material"*, J. Am.Ceram. Soc., 76, 1, IAN1993, 65–73;

[17]. **D. Dey, R.C. Bradt** - *"Grain growth of ZnO during Bi$_2$O$_3$ liquid-phase sintering"*, J. Am. Ceram. Soc., 75, 1992, 2529–2534;

[18]. **J. Kim, T. Kimura, T. Yamaguchi** - *"Effect of bismuth oxide content on the sintering of zinc oxide"*, J. Am. Ceram. Soc., 72, 1989, 1541–1544;

[19]. **T. Asokan, G.N.K. Iyengar, G.R. Nagabhushana** - *"Studies on microstructure and density of sintered ZnO-based non-linear resistors"*, J. Mater. Sci., 22, 1987, 2229–2236;

[20]. **M. Inada** - *"Crystal phases of nonohmic zinc oxide ceramics"*, Jap. J. Appl. Phys. 17, 1978, 1–10;

[21]. **M. Ito, M. Tanahashi, M. Uehara, A. Iga** - *"The Sb$_2$O$_3$ addition effect on sintering ZnO and ZnO + Bi$_2$O$_3$"*, Jpn. J. Appl. Phys., 36, 1997, 1460–1463;

[22]. **J. Ott, A. Lorenz, M. Harrer, E.A. Preissner, C. Hesse, A. Feltz, A.H. Whitehead, M. Schreiber** - *"The influence of Bi$_2$O$_3$ and Sb$_2$O$_3$ on the electrical properties of ZnO based varistors"*. J. Electroceram., 6, 2001, 135–146;

[23]. **P. Duran, F. Capel, J. Tartaj, C. Moure** - *"Low-temperature fully dense and electrical properties of doped-ZnO varistors by a polymerized complex method"*, J. Eur. Ceram. Soc., 22, 2002, 67–77;

[24]. **F. Greuter, G. Blatter** - *"Electrical properties of grain boundaries in polycrystalline compound semiconductors"*,

Semicond. Sci. Technol., 5, 1990, 111–1375;

[25]. **S. Tanaka, C. Akita, N. Ohashi, J. Kawai, H. Haneda, J. Tanaka** - „*Chemical-State Analysis of Grain-Boundaries in ZnO Varistors by Auger-Electron Spectroscopy"*, J. Solid State Chem., 105, 1993, 36-43;

[26]. **K.O. Magnusson, S. Wiklund** - *"Interface formation of Bi on ceramic ZnO: a simple model varistor grain boundary"*, J. Appl. Phys., 76, 1994, 7405-7409;

[27]. **F. Greuter** - *"Electrically active interfaces in ZnO varistors"*, Solid State Ionics, 75, 1995, 67-78;

[28]. **E. Olsson, G.L. Dunlop, R.** - ¨Osterlund, *"Development of interfacial microstructure during cooling of a ZnO varistor material"*, J. Appl.Phys., 66, 1989, 5072-5077;

[29]. **M.A. de la Rubia, M. Peiteado, J.F. Fernandez, A.C. Caballero** -*"Bi$_2$O$_3$ vaporization from ZnO-based varistors"*, J. Eur. Ceram., Soc. 24, 2004, 1209-1214;

[30]. **L. Hozer** - Semiconductor Ceramics: Grain Boundary Effects, Polish Scientific Publishers, Warszawa, Poland, 1994, p. 44;

[31]. **J. Wong** - *"Microstructure and Phase Transformation in a Highly Non-Ohmic Metal Oxide Varistor. Ceramic"*, J. Appl. Phys., 46, 1975, 1653-1659;

[32]. **M. Inada** - *"Formation Mechanism of Nonohmic. Zinc Oxide Ceramics"*, Jpn. J. Appl. Phys., 19, 1980, 409-419;

[33]. **J. Kim, T. Kimura, T. Yamaguchi** -*"Sintering of Zinc Oxide Doped with Antimony Oxide and Bismuth Oxide"*, J. Am. Ceram. Soc.,72, 1989, 1390-1395;

[34]. **A. Mergen, W.E. Lee** - *"Microstructural relations in BZS pyrochlore-ZnO mixtures"*, J. Eur. Ceram. Soc., 17, 1997, 1049-1060;

[35]. **J.P. Guha, S. Kunej, D. Suvorov** - *"Phase equilibrium relations in the binary system Bi2O3–ZnO"*, J. Mater. Sci., 39, 2004, 911-918;

[36]. **J. Kim, T. Kimura, T. Yamaguchi** - *"Sintering of Sb2O3-doped ZnO"*, J. Mater. Sci. 24, 1989, 213-219;

[37]. **E.R. Leite, M.A.L. Nobre, E. Longo, J.A.Varela** - *"Microstrutural development of ZnO varistor during reactive liquid phase sintering"*, J. Mater. Sci., 31, 1996, 5391-5398;

[38]. **V. Krasevec, M. Trontelj, L. Golic** - *"Transmission Electron Micro- scope Study of Antimony- Doped Zinc Oxide Ceramics"*, J. Am. Ceram. Soc, 74, 1991, 760-766;

[39]. **K.G.V. Kumari, P.D. Vasu, V. Kumar, T. Asokan** - *"Formation of Zinc–Antimony-Based Spinel Phases"*, J. Am. Ceram. Soc., 85, 2002, 703-705;

[40]. **N.Orban** - *Pigmenţi anorganici,* Ed. Tehnică, Bucureşti, 1974, p. 113;

[41]. **C.M. Beavis** - *Pigment*, Dyestufss and Laches, Ed. Chapmann and Hall, London, 1966.

VALUE ANALYSIS BETWEEN ART AND TECHNIQUE

Florin CHICHERNEA, Alexandru CHICHERNEA
Transilvania University of Brasov
email: chichernea.f@unitbv.ro, kiki_rider_r6@yahoo.com

ABSTRACT

Value Management is a method that provides an operating technique using a creative and organized approach. The Value Management includes Value Analysis managed by a group, each of them selected by their expertise in specific subjects and coordinated by a Value Analysis expert. The paper presents a complete study of Value Analysis applied specifically to one equipment, with one finality: re-design two selected pieces (the Flywheel and the Bearing). The phases and iterative operation of the Value Analysis method are presented. Value Analysis combines both engineering and economics without, however, placing either engineering or economics first. They both are similarly important, as can be concluded by the end of this paper.

KEYWORDS: value management, value analysis, value, optimum variant

1. Value analysis

Value Analysis is a method that provides an operating technique utilizing a creative and organized approach. It is managed by a group, each of them selected by their expertise in specific subjects and coordinated by a Value Analysis expert.

The Value Analysis group activity is managed in seven stages:

1. formation and functional analysis,
2. creativeness,
3. evaluation and selection of the proposals,
4. the creative phase,
5. development of the selected proposals,
6. presentation of the selected proposals, set in order by priority,
7. implementation phase.

An example of Value Analysis is presented, applied to the re-design of a jaw crusher used for primary crushing of a wide variety of materials in the mining, iron and steel and pit and quarry industries.

Next the establishing mode of the optimum constructive solution is presented from the technical and economic viewpoint for *two parts participating in two functions with a high cost:*

1. the Flywheel which contributes to the function F7 (it ensures the uniformity of the movement) and

2. the Bearing which contribute to the function F4 (it supports the assembly).

2. Establishing the list of functions and dimensions

Table 1 presents the list of functions of the jaw crusher.

Table 1. *List of functions (*FS – Service function,***FE – Estimation function)*

Symbol	Function	Type of function	Technical dimension of function		
			Name	UM	Value
...					
F4	*It supports the assembly*	*FS*	*weight*	*daN*	*20000*
F5	Aesthetics	FE***	colour, form	-	7
F7	*It ensures the uniformity of the movement*	*FS*	*revolution pulsation*	*rpm rad/sec*	
...					

3. Establishing the levels of importance of the functions-step 1

Table 2 presents the value weighting of the functions. The following percentage values of the functions value weighting result: X_{F1}=20%,

X_{F4}=17.8%, X_{F3}=15.6%, X_{F7}=13.1%, X_{F5}=11.1%, X_{F6}=8.89%, X_{F2}=6.67%, X_{F10}=4.44% and X_{F9}=2.22%.

The product value is equal to the sum of the functions levels and is equal to 45.
The studied jaw crusher is shown in [8].

Table 2. *Value weighting of the functions (*X coordinate)*

Functions	F1	F4	F3	F7	F5	F6	F2	F10	F9	Total
No. of points	9	8	7	6	5	4	3	2	1	45
Ratio	0.2	0.17	0.15	0.13	0.11	0.08	0.06	0.04	0.02	1
*Percentage %	20	17.8	15.6	13.3	11.1	8.89	6.67	4.44	2.22	100
Functions	F1	F4	F3	F7	F5	F6	F2	F10	F9	Total

4. Economic dimensioning of the functions

Costs were assigned to the various functions by means of the functions-costs matrix shown in Table 3.

The percentage values of the functions participation in the total cost are: Y_{F1} = 16%, Y_{F4} = 14.3%, Y_{F3} = 15.2%, Y_{F7} = 14.4%, Y_{F5} = 11.7%, Y_{F6} = 7.83%, Y_{F2} = 11.2%, Y_{F10} = 4.79% and Y_{F9} =4.6%

Table 3. *Distribution of costs on functions (*Y coordinate, ** monetary units)*

No.	Parts	Functions									Cost part**
		F1	F4	F3	F7	F5	F6	F2	F10	F9	
7	Flywheel	20			15			30	10	25	100
...											
17	Bearing	250	30					70	20	30	400
...	...	550	700	750	720	500	400	410	215	175	4420
Total cost		820	730	775	735	600	400	570	245	235	5110
Ratio		0.16	0.14	0.15	0.14	0.11	0.07	0.11	0.04	0.04	1
Cost of functions %		16	14.3	15.2	14.4	11.7	7.83	11.2	4.79	4.6	100

5. Diagrams

The construction of the diagrams is presented.
Based on the values for coordinates x_i and y_i presented in Table 4 the diagrams of Figures 1, 2 and 3 are plotted.
The parameters have the following computed values: a = 0.93, α = 42.9°, S = 4.57, S' = 0.

Table 4 provides the necessary values for constructing the following types of diagrams:
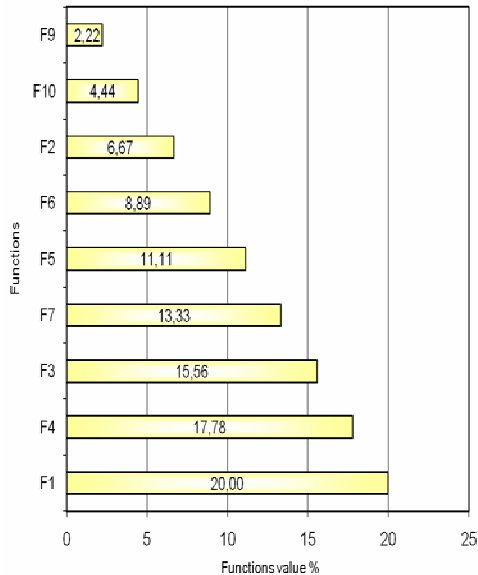1. in Figure 1, the diagram of the functions value weighting,
2. in Figure 2, the diagram of the functions cost weighting,
3. in the Figure 3, the diagram of the functions value and cost weighting.

Table 4. *Computational elements for plotting the diagrams*

| No	Computational elements	Functions									Total value
		F1	F4	F3	F7	F5	F6	F2	F10	F9	
1	X_i	20	17.8	15.6	13.3	11.1	8.89	6.67	4.44	2.22	100
2	Y_i	16	14.3	15.2	14.4	11.7	7.83	11.2	4.79	4.6	100
3	$(X_i)^2$	400	316	242	177	123	79.0	44.4	19.7	4.93	1407
4	$X_i * Y_i$	320.9	254	235	191	130	69.5	74.3	21.3	10.2	1309
5	$(Y_i - a*X_i)^2$	6.493	5.03	0.49	3.94	1.99	0.19	24.5	0.43	6.41	49.57
6	S' *	101.9	79.7	-21	-52	-31	7.76	-66	-5.8	-11	2E-13

$$*S' = 2 * a *(X_i)^2 – 2 * X_i * Y_i$$

Figure 1 shows the ranking of the functions by their value.

Fig.1. *Diagram of the functions value weighting.*

Figure 2 shows the ranking of the functions by their functional cost.
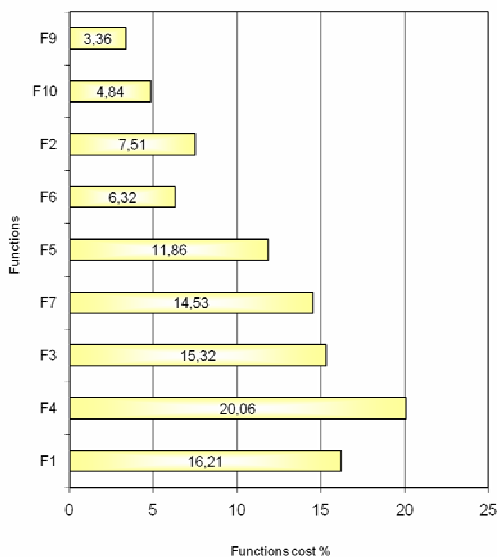
Fig.2. *Diagram of the functions cost weighting*

The diagram reveals a Pareto type distribution, meaning that 20 - 30% of the total number of functions include 70 - 80% of the total costs of the functions. These functions are F1, F4, F3 and F7.

In the case of such a distribution, the first functions in the order of costs, representing 20 - 30%

of the total number of functions (in the above example functions F1, F4, F3 and F7) are considered to be very expensive functions.

The real situation is represented by the shape of the straight line in Figure 3, plotted by means of the smallest squares method, and showing disproportions in the distribution of costs and in the contribution of the various functions to the value of the product.

An analysis of the diagram in Figure 3 shows that functions F9, F5, F7 and F4 are located above the regression line, indicating high costs, not justifiable in relation to the value.

These aspects allow the assumption that these functions are deficient, hence the solutions to be identified are to focus on those assemblies, parts, materials and technological operations that contribute, within the general structure of the product, to the achievement of these functions.
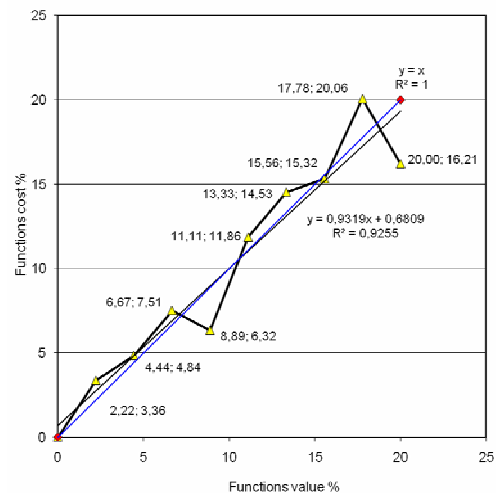
Fig. 3. *Value and cost weightings of the functions.*

A basic criterion of Value Analysis is obtaining a minimum value for S'.

In order to diminish estimator S', the points need to be aligned as perfectly as possible along the straight line y = a * x, with a tilt of 45°.

Firstly, in order to diminish the costs, those functions will be re-designed that are located above the straight line.

For the points below the line the problems is more complicated.

By diminishing the cost of the functions above the straight line, it may change its tilt and the points initially located below the line may appear above it. It is also evident that by diminishing the cost of certain functions the total costs of the product decreases, the weighting of the functions that were not modified increasing implicitly.

This is another cause for some points relocating from below the straight line to above it, without, however, any modification occurring in the absolute value of the costs of these functions.

Secondly, the minimization of S' needs to be understood in the sense of growth of the value/cost ratio as much as possible, and not in the sense of imposing S' = 0.

Thirdly, Value Analysis also admits the increase of the costs of some functions, provided their value increases at a faster rate than the costs.

Practically, the criterion of minimization of S' leads most often to cascading Value analysis studies, the optimization of the constructive solution being thus an iterative process. At first, the functions above the regression straight line are analyzed and their costs

reduced, then the regression line is re-plotted and the functions relocated above it are noted; these functions too are analyzed in view of reducing their costs, followed by the re-plotting of the regression line, etc.

Hence the constructive solution is improved from one iteration to the other.

6. Establishing the functional-technological form of the parts in view of cost reduction for the flywheel

An analysis from the technical and economic viewpoint will be carried out in order to select a technically optimum variant for *two selected pieces of equipment: the flywheel and the bearing.*
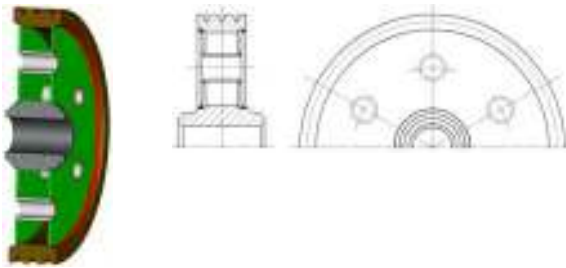
Fig. 4. *Flywheel made of the welded semi-products.*
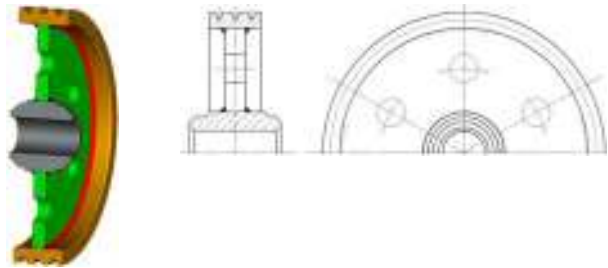
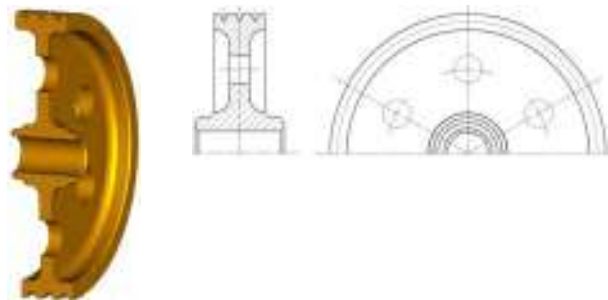**Fig. 5.** *Flywheel made from the welded semi-products.*

Four constructive variants of flywheel will be studied and eventually the most cost effective and the most competitive one from the technical and economic viewpoint will be selected. Figures 4 and 5 present a flywheel made of the welded semi-products.

The functional characteristics for this type of part are the following:
1.   maximum diameter, diameter of engagement, geometrical elements of connecting gear,
2.   internal diameter of wheel hub, concentricity between flywheel axis and diameter of engagement,
3.   wearing resistance, reconditioning method.

Figure 6 presents a flywheel screw assembled and Figure 7 presents a flywheel made of a cast semi-product.

All variants are technological and the selection of one of them depends on the level of endowment of the company.

The constructive variant in Figure 7 obtained from a cast semi-product ensures the best functional characteristics, if the technical conditions for heat treatment are provided. It has, however, the disadvantage that it allows only one solution for reconditioning: build-up welding and re-machining to the initial functional dimensions.

Fig. 6. *Flywheel screw assembled*

Fig. 7. *Flywheel made of a cast semi-product*

7. Comparison of the variants for flywheel

Table 5 presents the denotings by 9 assessment criteria of the analyzed constructive variants of a flywheel. The variant in Figure 7 has obtained the highest score, and will thus be selected as the constructive solution within the assembly of the jaw crusher.

Table 5. Synthetic table with the analyzed constructive variants for flywheel

No.	Analysis criteria	Figure 4	Figure 5	Figure 6	Figure 7
1	Functional characteristics	4	4	4	4
2	Semi-product	1	2	3	4
3	Mechanical machining	1	2	3	1
4	Mounting	4	4	4	4
5	Repair	4	4	4	4
6	Rigidity	3	3	2	4
7	Ergonomics	2	2	2	4
8	Aesthetics	3	3	3	4
9	Cost	1	2	3	4
	TOTAL	23	26	28	33

8. Establishing the functional-technological form of the parts in view of cost reduction for the bearing

An analysis from the technical and economic viewpoint will be carried out in order to select a technically optimum variant for the bearing. Six constructive variants of bearings will be studied and eventually the most cost effective and the most competitive one from the technical and economic viewpoint will be selected.

The analysis of the constructive variants for the support (bearing) in Figures 8, 9, 10, 11, 12 and 13 is presented further on.

The Figures 8, 9 and 11 show three constructive – technological variants of the support (bearing): welded semi-product made of three, six and five modules, the Figures 10 and 12 shows two constructive cast semi-product and Figure 13 presents a complex bearing.

The constructive variant of Figure 12 obtained from a cast semi-product ensures the best functional characteristics, if the technical conditions for heat treatment are provided. It has, however, the disadvantage that it allows only one solution for reconditioning: build-up welding and re-machining to the initial functional dimensions. The difficulty in this case is applying a heat treatment subsequent to reconditioning.
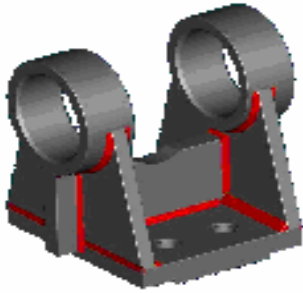

Fig. 8. Support made of welded semi-products.
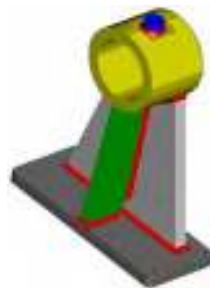
Fig. 9. Support made of welded semi-products.

Fig. 10. Support made of cast semi-product.

Fig. 11. *Support made of two welded semi-products*

Fig. 12. *Support made of cast semi-product*

Fig. 13. *Complex bearing*

9. Comparison of the variants for bearing

Table 6 presents the denoting by 9 assessment criteria of the analyzed constructive variants of a bearing. But in many cases the bearing must be made of two parts, to facilitate quick installation and removal of all assembly (Figure 14 and Figure 15). The bottom can body with the cradle, can be incorporated into the cradle.

Table 6. *Synthetic table with the analyzed constructive variants for bearing.*

No.	Analysis criteria	Figure 8	Figure 9	Figure 10	Figure 11	Figure 12	Figure 13
...	...						
9	Cost	5	4	4	3	6	2
	TOTAL	45	40	42	39	*51*	41

Fig. 14. *Complex bearing*
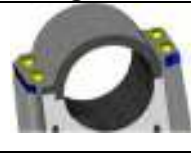
Fig. 15. *Bearing incorporated in to the cradle*
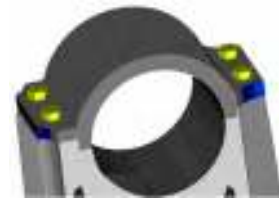
Given the option of Figure 14 and 15, the Value Analysis study may be repeated, for comparing the share value and cost functions and this is the next step of the study and Table 7 presents the new denoting by 9 assessment criteria of the analyzed constructive variants of a bearing.

Tabele 7. *Synthetic table with the analyzed constructive variants for Bearing.*

No.	Analysis criteria	Figure 10	Figure 12	Figure 13	Figure 15
...	...				
9	Cost	4	6	2	3
	TOTAL	42	*51*	41	*49*

The variant in Figure 12 obtained a score better than the version in Figure 15, but in many cases the bearing must be made of two parts, to facilitate quick installation and removal of the assembly.

The score obtained by the variant in Figure 15 is less than the cast version in Figure 12, but choise of the variant in Figure 15 is made because the weight of the advantages is greater than the weight of disadvantages for variant in Figure 12.

The version in Figure 15 has the following advantages over the version in Figure 12:
1. installation and removal are all much easier,
2. maintenance runs also easier.
The disadvantages of the variant in Figure 15 and of the variant in Figure 12 are:
1. the process of obtaining semi – product: this can be seen in the choise of the piece compared of 2 modules,
2. the machining by cutting: machining process is longer, more complicated and costly,
3. the functional cost of this variant is greater, but the difference is non significant.

10. Establishing the levels of importance of the functions – step 2

Table 8 presents the value weighting of the functions, in the second step of the Value Analysis study, the final situation.

Table 8. *Cost distribution on functions (*Y coordinate, ** monetary units)*

No	Parts	Functions									Cost part**
		F1	*F4*	F3	*F7*	F5	F6	F2	F10	F9	
1	Fix crushing jaw		60	24		90		50		4	228
...											0
7	Flywheel	10			15			25	5	22	77
...											0
17	Bearing	250	20					68	15	28	381
...	...	550	800	750	670	500	400	300	215	175	4360
Total cost		810	880	774	685	590	400	443	235	229	5046
Ratio		0.16	0.17	0.15	0.13	0.11	0.07	0.08	0.04	0.04	1
Cost of functions %		16.1	17.4	15.3	13.6	11.7	7.93	8.78	4.66	4.54	100

By introducing the new data into Table 9 the three diagrams in Figures 16, 17 and 18 are plotted. These diagrams will be compared to those in Figures 1, 2 and 3. The parameters have the following computed values: a = 0.95, α = 43.6°, S = 23.83, S' = 0. It can be noticed that S and S' have smaller values than in the initial variant.

Table 9 provides the necessary values for the plotting of the following types of diagrams:
1. the diagram of the value weighting of the functions (Figure 16).

2. this diagram has not changed, as the value of the system and of the functions has remained the same and is similar to Figure 1,
3. the diagram of the functions cost weighting (Figure 17). The diagram in Figure 18 presents the functional costs of the new variant, step 2.
4. the diagram of the cost weightings of the functions, step 1 and step 2 (Figure 18).

Figure 18 presents the diagram of the cost weightings of the functions in step 2 of the Value Analysis.

Table 9. *Computational elements for plotting the diagrams.* $S' = 2 * a * (X_i)^2 – 2 * X_i * Y_i$

No	Computational elements	Functions									Total value
		F1	F4	F3	F7	F5	F6	F7	F10	F9	
1	X_i	20	17.8	15.6	13.3	11.1	8.89	6.67	4.44	2.22	100
2	Y_i	16.1	17.4	15.3	13.6	11.7	7.93	8.78	4.66	4.54	100
3	$(X_i)^2$	400	316	242	177	123	79.0	44.4	19.7	4.93	1407
4	$X_i * Y_i$	321	310	238	181	129	70.4	58.5	20.6	10.0	1340
5	$(Y_i - a*X_i)^2$	8.97	0.25	0.27	0.76	1.23	0.29	5.90	0.18	5.86	23.74
6	S' *	119	-18	-16	-23	-24	9.57	-32	-3.7	-10	0

Only the costs are represented in order not to overload the diagram and to observe the decrease of the value of cost:

1. of function F4, from 20.06 %, in the first step of the Value Analysis study to 17.44 % in the second step of the Value Analysis study, with a decrease of 15 %.

2. of function F7, from 14.53 %, in the first step of Value Analysis study to 13.58 % in the second step of Value Analysis study, with a decrease of 7 %.
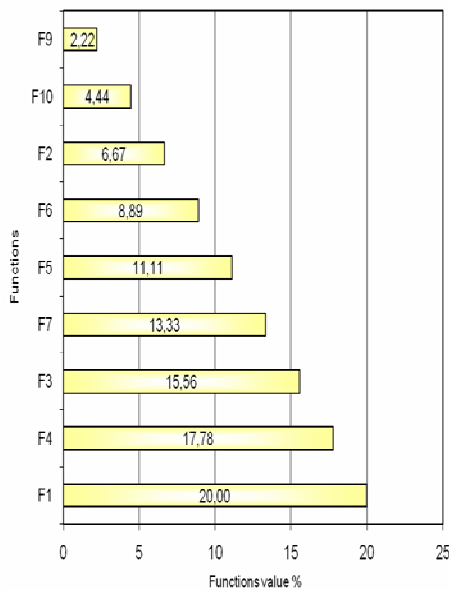

Fig. 16. *Diagram of the value weighting of the functions.*
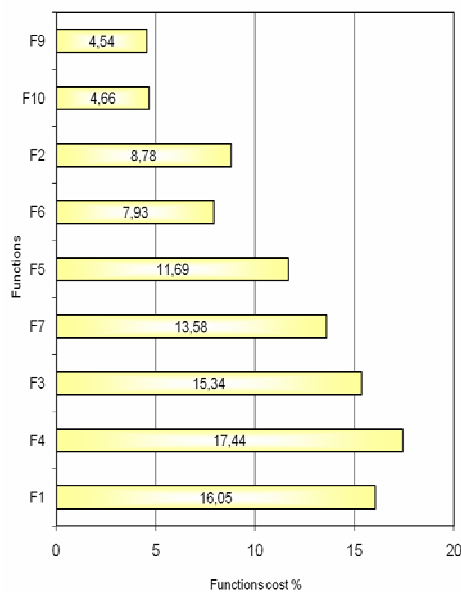
Fig. 17. *Diagram of the functions cost weighting.*
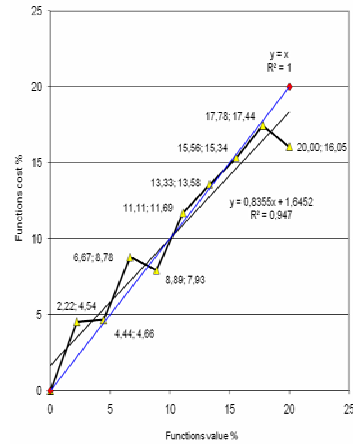
Fig. 18. *The diagram of the cost weightings of the functions in step 2.*

The economic dimension or the cost of the function represents the main criterion for the critical evaluation of functions.

These evaluations aim at identifying those functions, the too costly technical solutions of achievement which affect the total manufacturing cost of the analyzed product.

A correctly completed critical evaluation will directly lead to the identification of what can be called the deficient functions of the analyzed product that is of those functions that include useless costs.

The deficient functions from the economic viewpoint appear as: very expensive functions in relation to the others.

11. Conclusion

In two steps of the Value Analysis study two components of the jaw crusher, the flywheel which contributes to the function F7 (*it ensures uniformity to the movement*) and the bearing which contributes at the function F4 (*it supports the assembly*) were redesignted and optimized:

1. From the engineering viewpoint (Figure 19 and Figure 20),

a. from variant of flywheel in Figure 4 consisting of five welded modules, one complicated part (many components, machining mechanical, turning of metal parts complicated, long and very expensive, etc.) to the variant in Figure 7 consisting of cast semi-product (one component, mechanical machining, simple turning of metal parts, short and less expensive than the flywheel in Figure 4, etc.).

b. from the variant of bearing in Figure 8 consisting of three welded modules, one complicated part (many components, machining mechanical, complicated turning of metal parts, long and very

expensive, etc.) to the variant in Figure 15 consisting of cast semi-product (two components, mechanical machining, simple turning of metal parts, short and less expensive than the bearing of Figure 8, etc.).

Fig. 19.

2. From the economic viewpoint (Figure 21):

a. the cost of function F7 (Figure 18) decrease sfrom 14.53 %, in the first step of the Value Analysis study to 13.58 % in the second step of the Value Analysis study (decrease by 7 %).
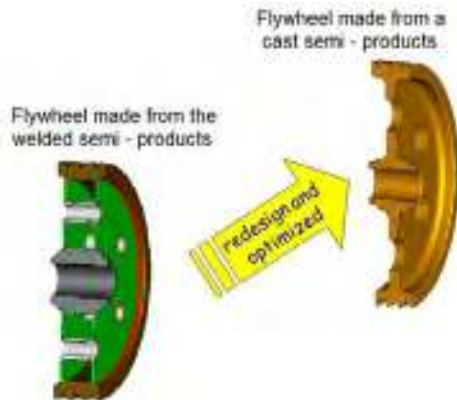
b. the cost of function F4 (Figure 21) decreases from 20.06 %, in the first step of the Value Analysis study to 17.44 % in the second step of the Value Analysis study (decrease by 15 %).

Fig. 20.

Fig. 21.

3. ***In the third step of the Value Analysis study are analyzed other functions above the regression straight line*** (for example F1) and their costs reduced, then the regression line is re-plotted and the functions relocated above it are noted; these functions too are analyzed in view of reducing their costs, followed by the re-plotting of the regression line, etc.

At the end of the Value Analysis study, the points are aligned as perfectly as possible along the straight line y = a * x, with a tilt of 45°, this is the optimal situation, the values weighting of functions and the functions cost weighting are equal.

References

[1]. www.bikudo.com/product_search/detai
[2]. Chichernea Fl. - *Analiza Valorii*, Editura Universităţii Transilvania din Braşov, 2002
[3]. Bejan V. - *Tehnologia fabricării şi a reparării utilajelor tehnologice*, vol.I şi vol.II, Oficiul de Informare Documentară pentru Industria Construcţiilor de Maşini, Bucureşti, 1991
[4]. Chichernea Fl. - *Analiza valorii*, Editura Universităţii Transilvania Braşov, 2007
[5]. Chichernea Fl. - *Analiza valorii*, Universitatea Transilvania Braşov, 2007, CD
[6]. Chichernea Fl. - *Analiza Valorii.* Partea I, Bramat 2007, Proceedings - International Conference on Materials Science and Engineering, Braşov, România, 22-24.feb.2007, vol.I
[7]. Chichernea Fl., Chichernea Al. - *Value Analysis*, part III, Rev.Metalurgia International nr.2, 2010, pg. 22.
[8]. Chichernea Fl., Chichernea Al. - *Redesigning a jaw crusher using value analysis*-*Part I, II,* The Annals of "Dunarea de Jos" University of Galati. Fascicle IX. Metallurgy and Materials Science, N^0. 1,2 – 2009, ISSN 1453 – 083X.

INFLUENCE OF RIB THICKNESS ON THE SOLIDIFICATION OF CAST PARTS

Ioan CIOBANU, Diana ŢUŢUIANU, Tibor BEDŐ, Aurel CRIŞAN

Faculty of Materials Science and Engineering
"Transilvania" University of Braşov,
email: ciobanu_i_bv@yahoo.com

ABSTRACT

The ribs applied to the walls of cast parts are designed for enhancing both stiffness and aesthetics. The presence of ribs modifies the conditions of heat transmission and implicitly the solidification of the alloy in the joining area of the rib to the part wall. This is highlighted by the modified radius of the circles inscribed in the rib – wall joining area. The diameter of the circles inscribed in this area is greater than of those in the rest of the part wall. This leads to the assumption that the solidification of the alloy in this area is slowed. The paper presents the results of a study concerning the influence of rib thickness on the duration of cast part solidification and on the position of the hot spots. The study was conducted by computer simulation of solidification. The results have revealed that in certain situations (thin ribs compared to wall thickness) the ribs cause an acceleration of the solidification of cast parts. The thickness of ribs ensuring the maximum cooling effect is determined.

KEYWORDS: rib thickness, cast parts solidification, computer simulation

1. Introduction

While representing the technological elements required by the designer or manufacturing engineer, ribs, casting slopes and corner radii of the cast parts also have an aesthetic function. Generally ribs have the role of stiffening the walls of the cast parts. These technological elements (ribs, slopes, corner radii) influence the solidification of cast parts. Ribs determine a local thickening of parts in the rib – part wall joining area, as highlighted by the local increase of the circle radii inscribed in the part perimeter, as shown in Figure 1.

Consequently it is to be expected that these technological elements determine a local increase of solidification time and hence the generation of hot spots, causing on their turn solidification-specific defects (porosity, shrinkholes, cracks, etc.).

The paper presents the results of a study on the influence of rib thickness on the solidification of cast parts, and thus on the tendency of defect generation caused by solidification. The aim is to establish the magnitude of this influence and the opportunity of prevention measures.

Research was conducted by computer aided simulation of the solidification process, by means of the dedicated "Sim-3D" software, developed at the Faculty of Materials Science and Engineering of the Transilvania University of Braşov.

2. Influence of rib thickness on the solidification of cast parts

The rib thickness influence on the solidification of cast parts has been studied.

The test piece thickness was of a = 20 mm. Figure 2 shows the geometry and dimensions of the cast parts and casting mould included in the study. The ribs length was of L_n = 50 mm. The rib thickness was between b_n = 0 mm and b_n = 23 mm.

The study was conducted on eutectic cast iron parts cast in silica sand moulds. Table 1 features the thermo-physical characteristics of the alloy and the mould used for simulation.
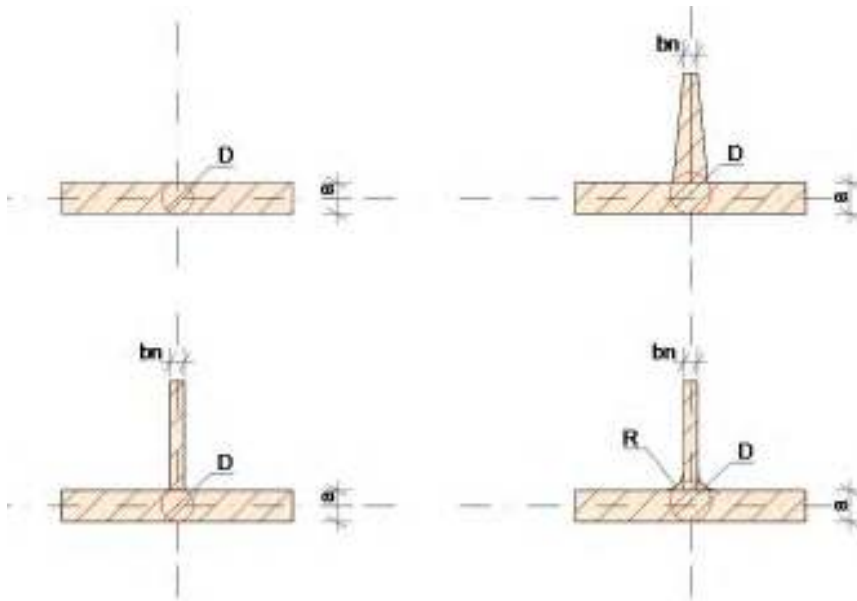
Fig. 1. *Influence of rib thickness, casting slopes and corner radii on the diameter of the circle inscribed in the contour of the cast parts.*
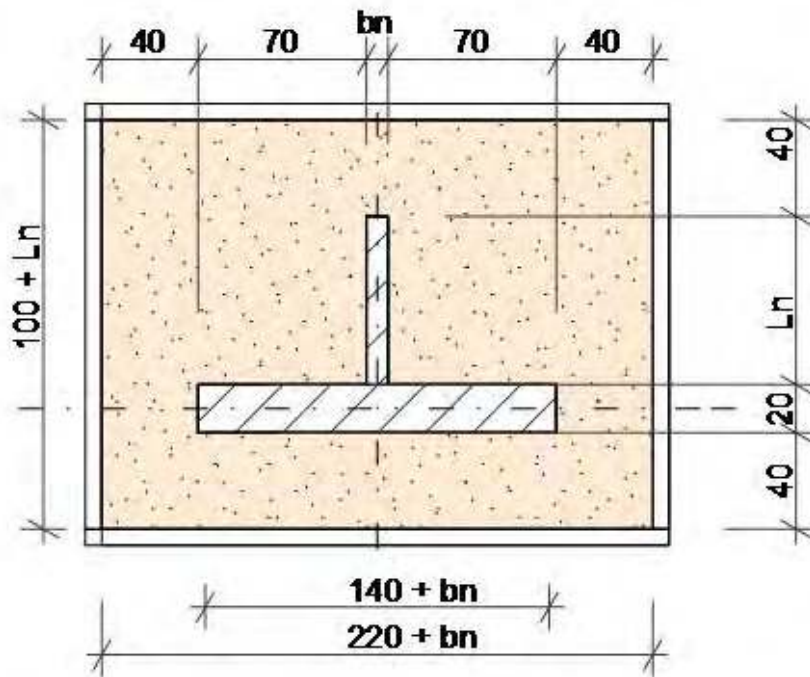
Fig. 2. *Geometry and dimensions of the part and mould.*

The study concerned the influence of rib length on the position of hot spots, on the solidification time, on temperature variation and on the solidified fraction in the hot spots. Figures 3 ÷ 9 show for a number of the studied cases the distribution of the isotherms in the cast part and the mould at the moment of solidification of the hotspots.

Table 2 shows the coordinates of the hot spots and their respective solidification times

Table 1. *Values of the quantities used for simulation of solidification*

| No.	Parameter	Physical symbol	Measure unit	Value
1	Mesh width of mould dividing	Δ	m	0,001
2	Time interval	τ	s	0,02
3	Environment temperature for the exterior of the mould	T_{ex}	^{0}C	20
4	Thermal exchange coefficient of the mould-exterior environment	α_{ex}	$W \cdot m^{-2} \cdot K^{-1}$	10,0
5	Solidus temperature of the cast alloy	T_{sme}	^{0}C	1150
6	Thermal conductibility coefficient of the mould	λ_{sfo}	$W \cdot m^{-1} \cdot K^{-1}$	0,85
7	Thermal conductibility coefficient of the solidified alloy	λ_{sme}	$W \cdot m^{-1} \cdot K^{-1}$	40
8	Thermal conductibility coefficient of the liquid alloy	λ_{lme}	$W \cdot m^{-1} \cdot K^{-1}$	30
9	Specific heat of the mould	C_{sfo}	$J \cdot kg^{-1} \cdot K^{-1}$	1170
10	Specific heat of the liquid cast iron	C_{lme}	$J \cdot kg^{-1} \cdot K^{-1}$	850
11	Specific heat of the solid cast iron	C_{sme}	$J \cdot kg^{-1} \cdot K^{-1}$	750
12	Mould density	ρ_{fo}	$kg \cdot m^{-3}$	1550
13	Alloy density	ρ_{me}	$kg \cdot m^{-3}$	6700
14	Specific latent heat of the cast alloy	L_{me}	$J \cdot kg^{-1}$	250000
15	Initial temperature of the mould	T_{0fo}	^{0}C	20
16	Initial temperature of the cast alloy	T_{0me}	^{0}C	1350

Table 2. *Coordinates of the hot spots and solidification time versus rib thickness*
(Rib length of L_n=50mm).

No.	Rib thickness	No. of hot spots	Coordinates of hot spots	Solidification time
Symbol	b_n	N_n	(x,y)	t_{sol}
u.m.	mm	-	(mm,mm)	s
1	0	1	(0;0)	300,38
2	3	2	(-21,0; -0,5) and (+21,0; -0,5)	262,58
3	5	2	(-20,0; +0,5) and (+20,0; +0,5)	270,50
4	9	2	(-15,0; +0,5) and (+15,0; +0,5)	299,94
5	13	2	(-9; +0,5) and (+9; +0,5)	333,32
6	15	1	(0; +0,5)	355,44
7	19	1	(0; +3,5)	401,42
8	23	1	(0; +6,5)	446,16
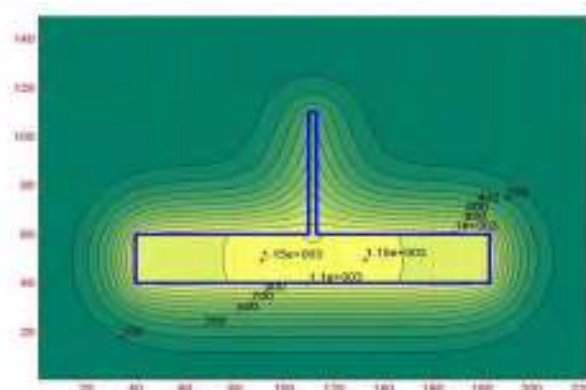
Fig. 3. *Outline of isotherms in the case of the part with a rib of thickness b_n = 3 mm.*
(at the moment of solidification t_{sol} = 262.58 s).
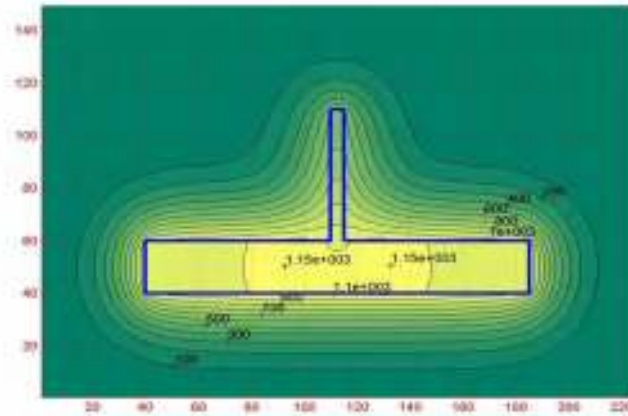
Fig. 4. *Outline of isotherms in the case of the part with a rib of thickness b_n = 5 mm (at the moment of solidification t_{sol} = 270.50 s).*
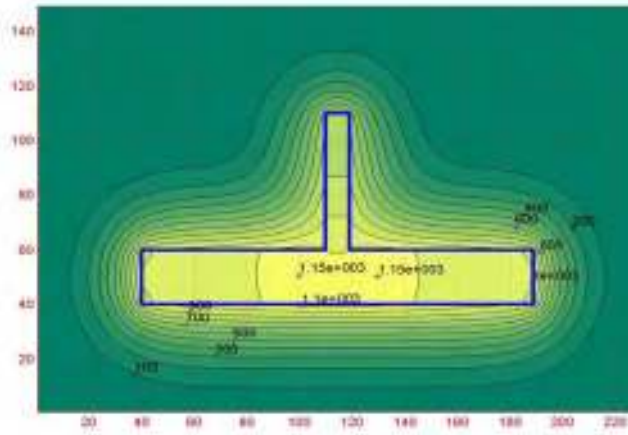
Fig. 5. *Outline of isotherms in the case of the part with a rib of thickness b_n = 9 mm (at the moment of solidification t_{sol} = 299.94 s).*
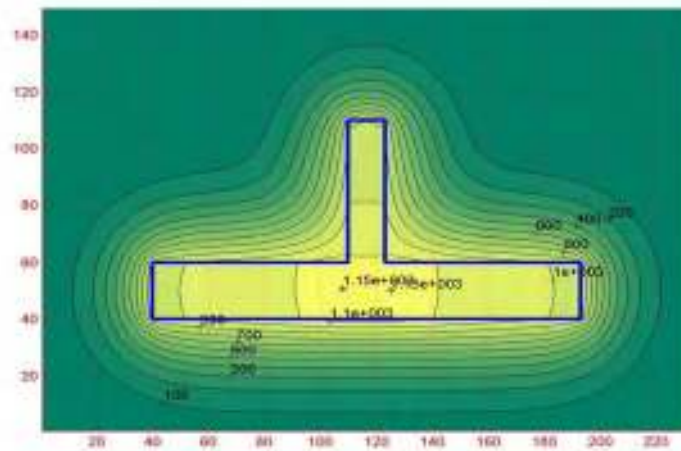
Fig. 6. *Outline of isotherms in the case of the part with a rib of thickness b_n = 13 mm (at the moment of solidification t_{sol} = 333.32 s).*
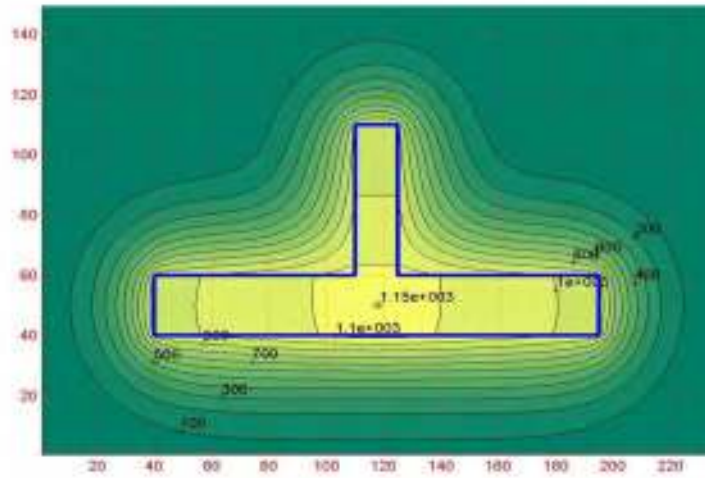
Fig. 7. *Outline of isotherms in the case of the part with a rib of thickness $b_n = 15$ mm (at the moment of solidification $t_{sol} = 355.44$ s).*
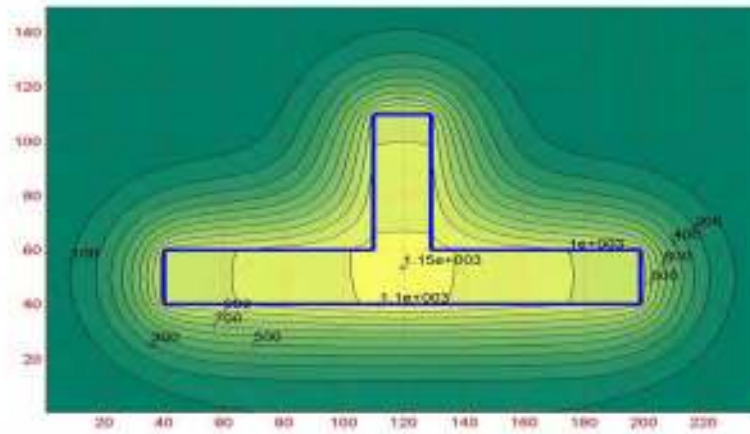
Fig. 8. *Outline of isotherms in the case of the part with a rib of thickness $b_n = 19$ mm (at the moment of solidification $t_{sol} = 401.42$ s).*
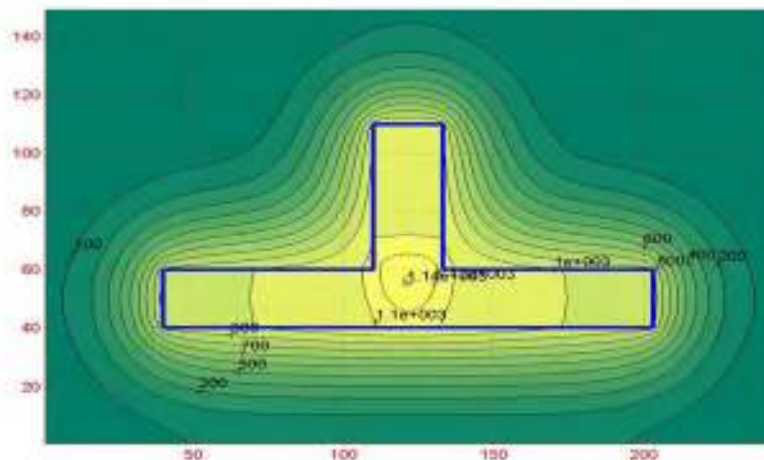
Fig. 9. *Outline of isotherms in the case of the part with a rib of thickness $b_n = 23$ mm (at the moment of solidification $t_{sol} = 446.16$ s).*

The hot spot coordinates relate to a frame of reference corresponding to the symmetry axes of the cast part walls, as shown in Figure 10. Figure 11 shows the influence of rib thickness on hot spot solidification time. Figures 12 ÷ 14 feature the distribution of temperatures in the mould, at a moment close to the end of the solidification time, along the AB line corresponding to the axis of 20 mm thickness wall in the case of a rib. Figures 15 ÷ 18 feature the variation curves of temperature and of the solid fraction in the hot spots for two of the studied cases.
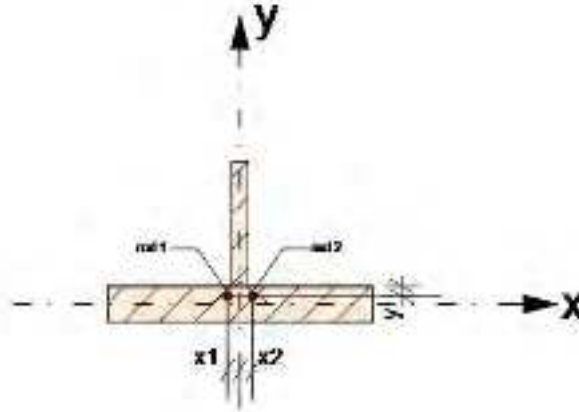
Fig. 10. Coordinates of the hot spots.
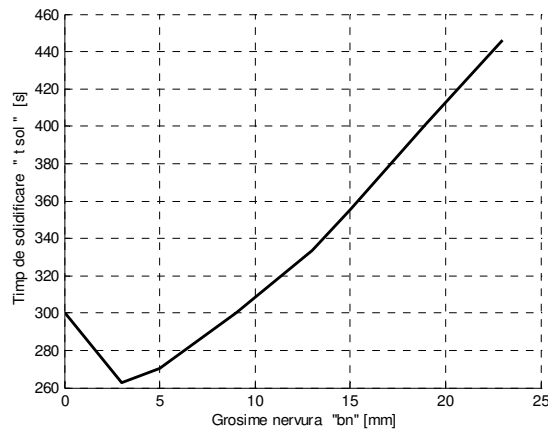
Fig. 11. Influence of rib thickness on the solidification of a part (plate of thickness a = 20 mm and rib of L_n = 50 mm length) (T_{sol} = Solidification time, b_n = Rib thickness).
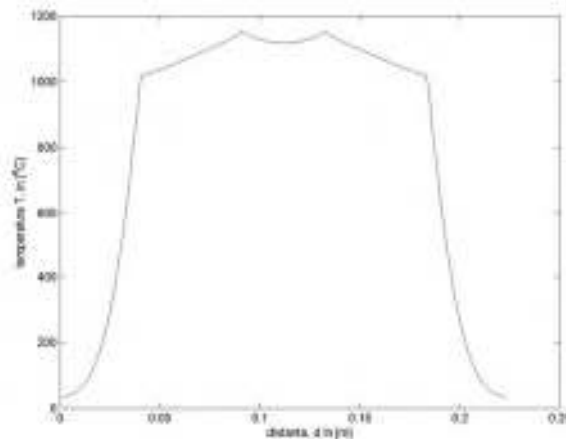
Fig. 12. Distribution of temperatures line AB (axis of wall of thickness 20 mm) in the case of a rib of thickness b_n = 3 mm, at moment t = 260s. (T = temperature d = distance).
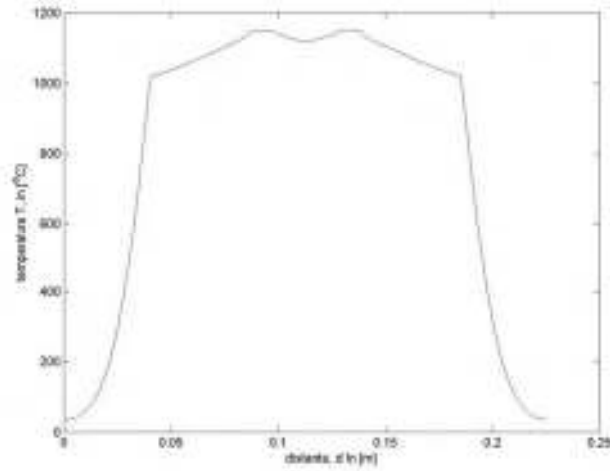
Fig. 13. *Distribution of temperatures line AB (axis of wall of thickness 20 mm) in the case of a rib of thickness b_n = 5 mm, at moment t = 260s. (T = temperature d = distance).*
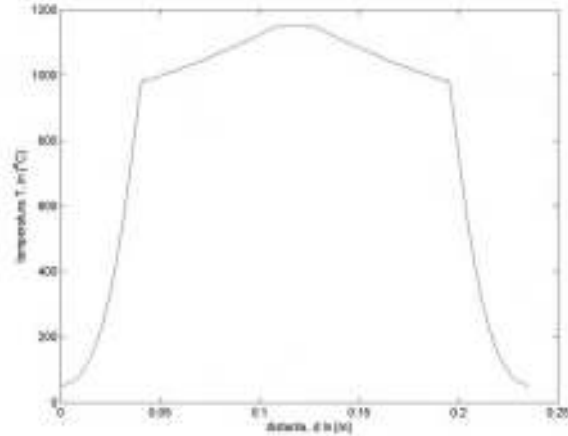
Fig. 14. *Distribution of temperatures line AB (axis of wall of thickness 20 mm) in the case of a rib of thickness b_n = 15 mm, at moment t = 340s. (T = temperature d = distance).*
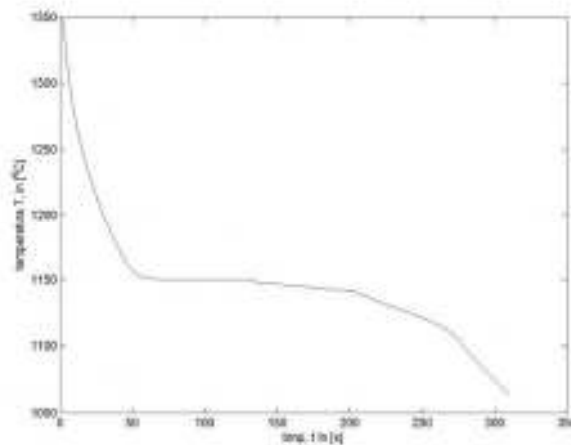
Fig. 15. *Variation of temperature in the point of coordinates (x,y) = (0; 0.5), rib of b_n = 3 mm thickness and L_n = 50 mm in length (T = temperature; t – time).*
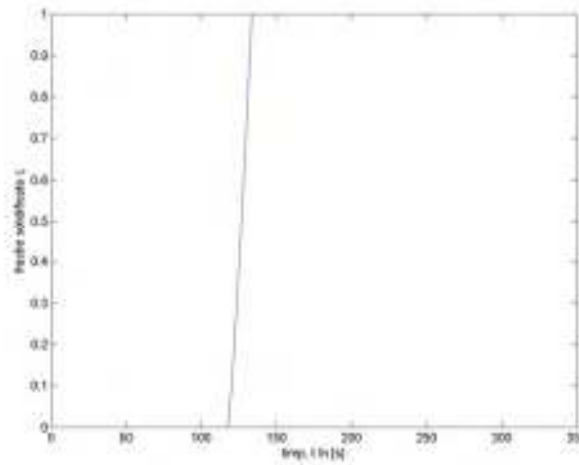
Fig. 16. *Variation of the solid fraction in the point of coordinates (x, y) = (0; 0.5), rib of b_n = 3 mm thickness and L_n = 50 mm in length (Solidified fraction; t = time).*
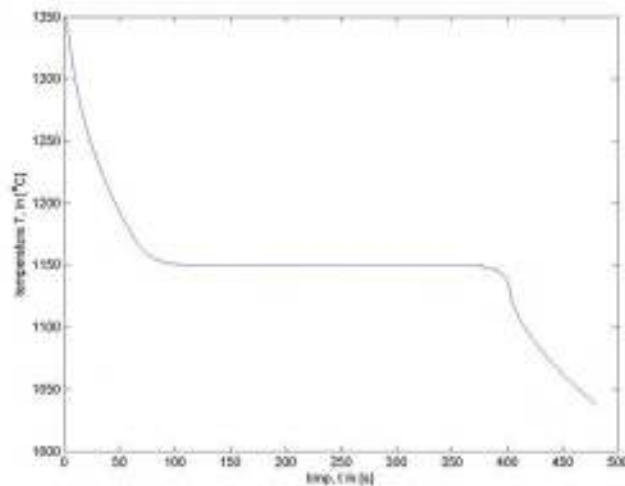
Fig. 17. *Variation of temperature in the point of coordinates (x, y) = (0; 0.5), rib of b_n = 19 mm thickness and L_n = 50 mm in length (T = temperature; t – time)*
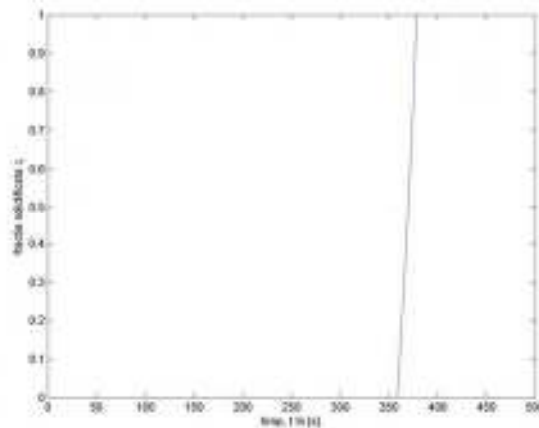
Fig. 18. *Variation of the solid fraction in the point of coordinates (x, y) = (0; 0.5), rib of b_n = 19 mm thickness and L_n = 50 mm in length (Solidified fraction; t = time).*

3. Conclusion concerning the influence of rib thickness on solidification

The following conclusions are yielded by the results of this study:

- ribs significantly thinner than the wall of the cast parts have a cooling effect, causing the decrease of solidification time compared to that of a ribless part;

- the cooling effect (or wing effect) is observed in the case of ribs thinner than 0.5a (half the wall thickness) and is clearly visible in Figures 12 and 13;

- the maximum effect of the cooling caused by the ribs is observed (in the case of the studied parts, part of thickness a = 20mm) for the rib of thickness b_n = 3mm);

- for rib thickness exceeding b_n = 9mm the cooling effect of the ribs disappears (Figure 14); thickness exceeding this value causes an increase of the cast part solidification time;

- in the part of thickness a = 20mm and thin ribs, $b_n \leq$ 13mm, two hot spots are generated, positioned symmetrically in relation to the rib axis;

- in the case of ribs with thickness $b_n \geq$ 15 mm a single hot spot is generated in the part, placed on the rib axis;

- the greatest decrease of solidification time (compared to the ribless part) is observed for the 3 mm thick rib, namely from 300.38s to 262.58s, representing 12.5%;

- Figures 15 ÷ 18 reveal the significant influence of rib thickness on temperature variation and solidification kinetics in the points of the rib – part wall joining area.

References

[1]. **Ciobanu I., Monescu V., Munteanu S. I., Crişan A.** – *Simularea 3D a solidificării pieselor turnate*, Editura Universităţii "Transilvania" din Braşov, Braşov, Ro, 2010, ISBN 978-973-598-678-0.

[2]. **Ciobanu I., Ţuţuianu Diana** – *Estetica, element valoric al pieselor turnate*, Metalurgia, nr. 1, pag. 3-8, ISSN 0461/9579.

[3]. **Ciobanu, I., Maşniţă, M., Monescu, V.** *Cercetări privind solidificarea pieselor cu secţiune "T"*, Metalurgia, nr.13, 2006.

[4]. **Maşniţă M.** – *Cercetări privind influenţa unor factori tehnologici şi constructivi asupra solidificării pieselor turnate*, Teză de doctorat, Universitatea Transilvania din Braşov, 2007.

[5]. **Ţuţuianu Diana, Ciobanu I.** – *Consideraţii privind implicaţiile tehnologice şi estetice ale înclinaţiilor de turnare şi ale razelor de racordare în cazul pieselor turnate*, Sesiunea de comunicări stiinţifice cu participare internaţională Terra Dacică - România mileniului trei. Acad. Forţelor aeriene Henri Coandă Brasov, 5-6 mai 2006, An VII, nr.1, CD - ISSN 1453 – 0139.

[6]. **Zirbo G., Ciobanu I.** – *Tehnologia turnării*, vol 1 & 2, Institutul Politehnic Cluj – Napoca, 1989.

MODELING OF THE MATERIAL FLOW AT THE ECAE PROCESS USING THE CURRENT LINES METHOD

Nicolae CĂNĂNĂU

"Dunărea de Jos" University of Galati
email: ncananau@yahoo.com

ABSTRACT

The Equal Channel Angular Extrusion is an important method of Sever Plastic Deformation, applied in aim the obtaining of nanostructured metallic materials. The cinematic field of the material may be described with various calculus methods. In this paper is developed a study of the flow field using the current lines theory.

KEYWORDS: advanced material, modeling, CAE, extrusion

1. Introduction

The metallic nanostructured materials have special properties, which justify the many researches applied for obtaining this advanced material. A very good method in the aim of working the nanostructured metallic materials is the ECAE.

This method consists in the extrusion of the material in the extrusion die [1, 2] with a constant cross section channel in an angle of 90^0, usually broken (Figure 1).
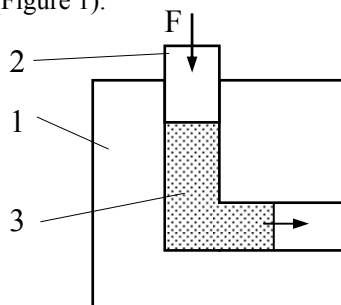
Fig. 1. *Scheme of the ECAE.*

The plunger 2 developed the force F and the material 3 flows in the channel of the extrusion die 1.

The plastic deformation process is localized in angular zone of the channel (Fig.2).
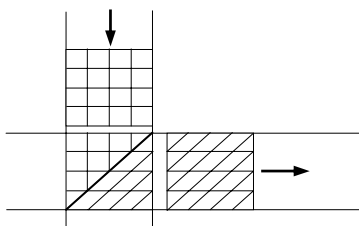
Fig. 2. *Deformation of lines net.*

In this location is developed a very intense plastic deformation by relative slide of the material layers, in condition of the compression stress state and great material plasticity. The plastic deformation degree is important.

For greater deformation intensity, the ECAE process may be repeated in a number of cycles [3, 4].

The equivalent strain, for a single extrusion, may be evaluated with the expression [5]:

$$\varepsilon_{eq} = \frac{1}{\sqrt{3}}\left[2\cot\left(\frac{\varphi}{2}+\frac{\psi}{2}\right) + \psi\cos ec\left(\frac{\varphi}{2}+\frac{\psi}{2}\right)\right] \quad (1)$$

The geometrical factors are defined in Figure 3.
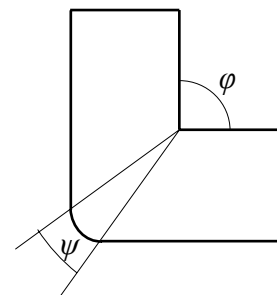
Fig. 3. *Geometrical factors of ECAE.*

For ensuring the continuity of the material flow the channel of die is worked with a cylindrical surface.

For this reason the passing zone, practically, is centered at the interior peak of the channel under the anter angle ψ (Fig.4).

The evolution of the material flow at the ECAE deformation process may be defined using the flow line method.

2. Definition of the flow line

The deformation volume is composed by three zones: first is the uniform zone at the entry of the channel, the second is the deformation zone, the material deformed by shear, the third is the uniform zone at the exit of the channel (Fig.4).

In these conditions the equation of the flow line is defined in the three zones as following.

In the first zone $\mathbf{D_1}$ the material particle flows in the direction of the Oy axis.

The equation of the flow line is:

$$x = x_0 \qquad (2)$$

In this relation x_0 is the Lagrange factor of the flow line and its value belongs to the real numbers domain, between 0 and a.
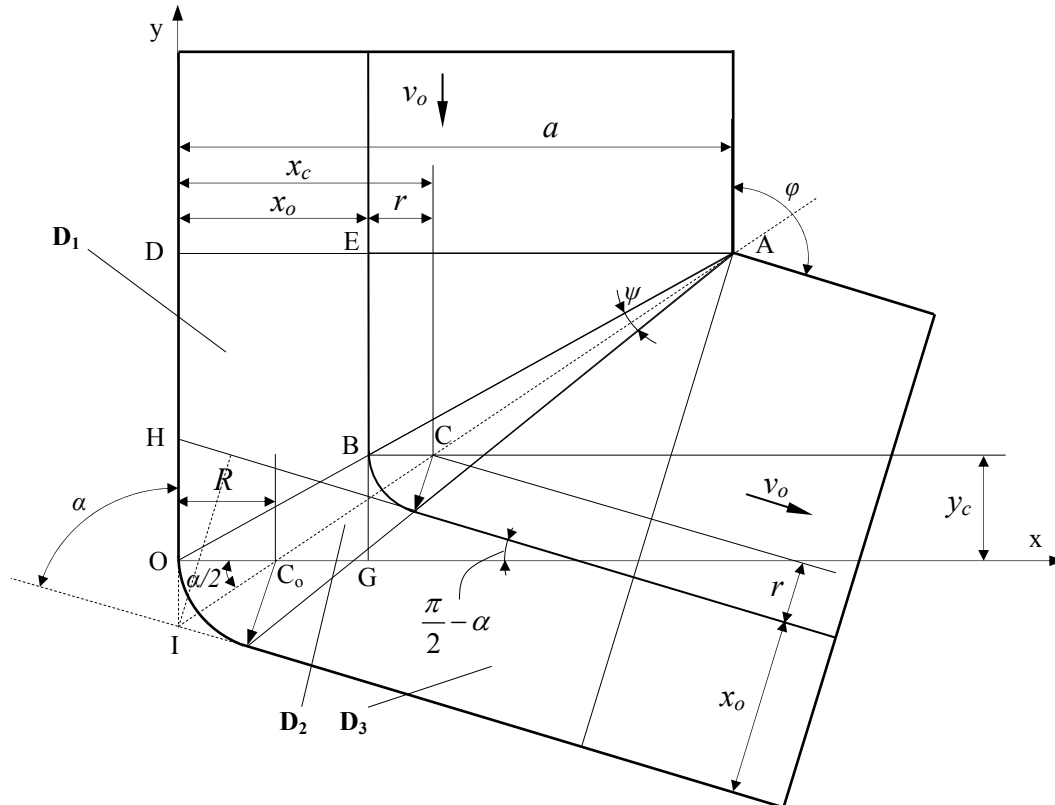
Fig. 4. Domains and flow line.

In the second zone $\mathbf{D_2}$ the elementary material particle goes from the first zone to the third zone through the circle arch BF.

The circle arch is determined by the construction of extrusion channel. In the practical conditions, at the passing from the vertical direction at the inclined direction, the channel has a cylindrical crossing zone.

We denote r_0 the radius of this cylindrical zone. The characteristics of the circle arch of the flow line are the radius r and the centre point C. It is evident the relation:

$$x_c = x_0 + r \qquad (3)$$

The coordinate y_c is defined by condition:

$$y_c = BG = EG - EB$$

but we have:

$$EG = OD = a \cdot \operatorname{tg}\left(\frac{\alpha}{2} - \frac{\psi}{2}\right)$$

and:

$$EB = AE \cdot \operatorname{tg}\left(\frac{\alpha}{2} - \frac{\psi}{2}\right) = (a - x_o) \cdot \operatorname{tg}\left(\frac{\alpha}{2} - \frac{\psi}{2}\right)$$

Results:

$$y_c = x_o \cdot \operatorname{tg}\left(\frac{\alpha}{2} - \frac{\psi}{2}\right) \qquad (4)$$

The angle ψ in the relation (4) is defined in function of the geometrical factors a, r_0, and α through the relation:

$$\operatorname{ctg}\frac{\psi}{2} = \frac{\dfrac{a}{R} - \sin^2\dfrac{\alpha}{2}}{\sin\dfrac{\alpha}{2}\cos\dfrac{\alpha}{2}} \qquad (5)$$

The radius of the circle arch is defined from the condition:

$$\frac{BC}{OC_o} = \frac{AB}{AO} = \frac{AE}{AD}$$

Results: $\quad r = R\dfrac{a - x_o}{a}$ (6)

The equation of the circle arch is:

$$(x - x_c)^2 + (y - y_c)^2 = r^2 \qquad (7)$$
$$\text{for} \qquad x \in [x_o, x_o + r(1 - \cos\alpha)]$$

In the third zone the elementary particle goes a trajectory inclined at the angle α according to the Oy direction. The equation of flow line in the third domain is defined through:

$$y = -x \cdot \text{ctg}\,\alpha + \frac{x_o}{\sin\alpha} - R \cdot \text{tg}\,\frac{\alpha}{2} \qquad (8)$$

3. Establishing the speed field

We consider v_0 the speed in the domain $\mathbf{D_1}$.
Thus in the first domain we have:

$$v_x = 0, \quad v_y = v_0 \qquad (9)$$

In the third domain the speed field is defined by the expressions:

$$\begin{aligned} v_x &= v_o \cdot \sin\alpha \\ v_y &= v_o \cdot \cos\alpha \end{aligned} \qquad (10)$$

In the second domain we use the equation of the definition of flow line:

$$\frac{dx}{v_x} = \frac{dy}{v_y} \qquad (11)$$

We differentiate the equation (7) and obtain:

$$\frac{dx}{dy} = -\frac{y - y_c}{x - x_c},$$

and we have:

$$\frac{v_x}{v_y} = -\frac{y - y_c}{x - x_c} \qquad (12)$$

From the continuity condition we have:

$$v_x^2 + v_y^2 = v_o^2 \qquad (13)$$

And, consequently it results:

$$\begin{aligned} v_x &= v_o \frac{y - y_c}{r} \\ v_y &= v_o \frac{x - x_c}{r} \end{aligned} \qquad (14)$$
$$\text{for} \qquad x \in [x_o, x_o + r(1 - \cos\alpha)]$$

4. Establishing the strain rate field

The components of the strain rate tensor are defined by the equations:

$$\dot{\varepsilon}_{ij} = \frac{1}{2}\left(\frac{\partial v_i}{\partial x_j} + \frac{\partial v_j}{\partial x_i}\right), \quad i, j = x, y \qquad (15)$$

The detailed forms of these equations, in the conditions of the ECAE process are:

$$\dot{\varepsilon}_{xx} = \frac{\partial v_x}{\partial x}, \; \dot{\varepsilon}_{yy} = \frac{\partial v_y}{\partial y}, \; \dot{\varepsilon}_{xy} = \frac{1}{2}\left(\frac{\partial v_x}{\partial y} + \frac{\partial v_y}{\partial x}\right) \qquad (16)$$

From the continuity condition we have the relation:

$$\dot{\varepsilon}_{xx} = -\dot{\varepsilon}_{yy}$$

In the domains $\mathbf{D_1}$ and $\mathbf{D_3}$ the field of the strain rate field is defined by the components:

$$\dot{\varepsilon}_{xx} = -\dot{\varepsilon}_{yy} = \dot{\varepsilon}_{xy} = 0 \qquad (17)$$

In the domain $\mathbf{D_2}$ we apply the conditions (16) of the equations (14) and obtain:

$$\dot{\varepsilon}_{xx} = -v_o \frac{(x - x_c)(y - y_c)}{\left[(x - x_c)^2 + (y - y_c)^2\right]^{\frac{3}{2}}} \qquad (18)$$

$$\dot{\varepsilon}_{yy} = v_o \frac{(x - x_c)(y - y_c)}{\left[(x - x_c)^2 + (y - y_c)^2\right]^{\frac{3}{2}}} \qquad (19)$$

$$\dot{\varepsilon}_{xy} = \frac{1}{2}v_o \frac{1}{\left[(x - x_c)^2 + (y - y_c)^2\right]^{\frac{1}{2}}} \qquad (20)$$

The strain rate intensity is defined by the expression:

$$\bar{\varepsilon} = \sqrt{\frac{2}{3}\left(\dot{\varepsilon}_{xx}^2 + \dot{\varepsilon}_{yy}^2 + 2\dot{\varepsilon}_{xy}^2\right)} \qquad (21)$$

We consider relations (18), (19) and (20) in the equation (21) and, after some transformations, we obtain:

$$\bar{\varepsilon} = \frac{2v_0}{\sqrt{3}r^3}\sqrt{4(y - y_c)^2\left[r^2 - (y - y_c)^2\right] + r^4} \qquad (22)$$

This equation is an invariant of the strain rate tensor and represents the global effect of the deformation process.

5. Establishing the strain field

As a result of using the strain-rate, we can define the strain field. For the calculus of the strain rate components, we can use the general expression:

$$\varepsilon_{ij} = \int_0^t \dot{\varepsilon}_{ij} \cdot dt \qquad (23)$$

And for establishing of the strain intensity field we can use the expression:

$$\bar{\varepsilon} = \int_0^t \bar{\dot{\varepsilon}} \cdot dt \qquad (24)$$

The differential of the time must be defined in function of the extrusion speed and the differential of the coordinate y, respectively, thus we have:

$$dt = \frac{dy}{v_0} \qquad (25)$$

And coupling the expression (22) with the expression (25) we obtain:

$$\bar{\varepsilon} = \frac{2v_0}{\sqrt{3}r^3} \int_{y_\alpha}^{y_c} \sqrt{4(y - y_c)^2 \left[r^2 - (y - y_c)^2\right] + r^4}\, dy$$

$$(26)$$

In the relation (26) we have:

$$y_\alpha = y_c \sin \alpha$$

Thus we can establish the strain field in the deformation zone.

Analyzing the expressions (18), (19) and (20) we observe that in zone of the entry of the extrusion die the deformations are null, also in the exit zone. The deformation is localized in the passing zone and consists in the crossing of material elements from the entry direction to the exit direction by a shear process (Fig.5).

Table 1. *Numerical results*

Xo	Xmax	R	(α-Ψ)/2	Xc	Yc	X	Y	éxx	éxy	é	Δd	Δt	Δε
0	2	2	38.66	2	0	0	0	0	1.25	1.4434	1.2649	0.1638	0.2820
						0.4	-1.2	-1.2	1.25	2.0008	0.5657	0.0722	0.1444
						0.8	-1.6	-1.2	1.25	2.0008	0.4629	0.0590	0.1118
						1.2	-1.833	-0.9165	1.25	1.7898	0.4196	0.0536	0.0896
						1.6	-1.9596	0.4899	1.25	1.5503	0.402	0.0512	0.0766
						2	-2	0	1.25	1.4434			0.7044
2	3.6	1.6	38.66	3.6	1.6	2	1.6	0	1.5625	1.8042	1.024	0.1328	0.2858
						2.32	0.64	-1.5	1.5625	2.501	0.4525	0.0578	0.1446
						2.64	0.32	-1.5	1.5625	2.501	0.3703	0.0472	0.1118
						2.96	0.1336	-1.1456	1.5625	2.2372	0.3357	0.0428	0.0896
						3.28	0.0323	-0.6124	1.5625	1.9378	0.3216	0.0410	0.0766
						3.6	0	0	1.5625	1.8042			0.7084
4	5.2	1.2	38.66	5.2	3.2	4	3.2	0	2.0833	2.4056	0.7589	0.0984	0.2824
						4.24	2.48	-2	2.0833	3.3347	0.3394	0.0434	0.1448
						4.48	2.24	-2	2.0833	3.3347	0.3463	0.0442	0.1420
						4.72	1.9904	-1.68	2.0833	3.0903	0.2424	0.0310	0.0880
						4.96	2.0242	-0.8165	2.0833	2.5837	0.2412	0.0308	0.0768
						5.2	2	0	2.0833	2.4056			0.7340
6	6.8	0.8	38.66	6.8	4.8	6	4.8	0	3.125	3.6084	0.506	0.0656	0.2594
						6.16	4.32	-2.9063	3.125	4.9278	0.2263	0.0290	0.1440
						6.32	4.16	-1.3179	3.125	5.0021	0.1852	0.0236	0.1118
						6.48	4.0668	-2.2913	3.125	4.4745	0.1678	0.0214	0.0894
						6.64	4.0162	-1.2247	3.125	3.8756	0.1608	0.0206	0.0770
						6.8	4	0	3.125	3.6084			0.6816
8	8.4	0.4	38.66	8.4	6.4	8	6.4	0	6.25	7.2169	0.253	0.0328	0.2824
						8.08	6.16	-6	6.25	10.0042	0.1131	0.0144	0.1446
						8.16	6.08	-6	6.25	10.0042	0.0926	0.0118	0.1118
						8.24	6.0334	-4.5825	6.25	8.9489	0.0832	0.0106	0.0884
						8.32	6.0106	-2.4338	6.25	7.7448	0.0816	0.0104	0.0778
						8.4	6	0	6.25	7.2169			0.7150

Consequently, in the domain **D$_2$** is developed great intensity of strain.

We consider *R=2*mm, *a=10*mm, *α=π/2*, *v$_0$=5*mm/s and five flow lines and five points at the length of each flow line.

Using the methodology described above we obtain the numerical results showed in Table 1.

Under the graphical form, the results are represented in Figures 5, 6, 7, 8 and 9.
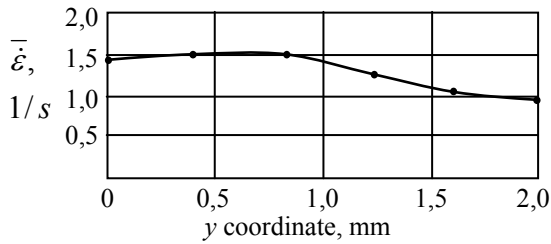
Fig. 5. *Variation of strain rate along the flow line for x$_0$=0.*
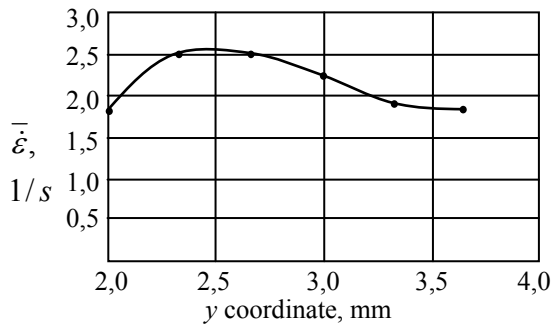
Fig. 6. *Variation of strain rate along the flow line for x$_0$=2.*
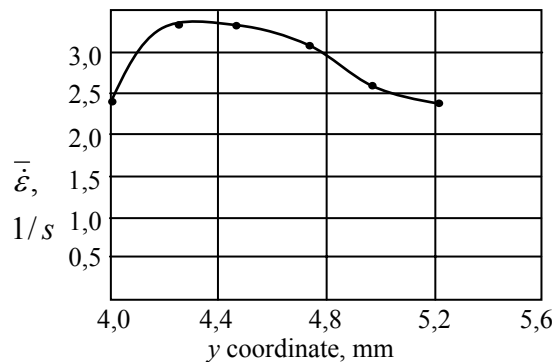
Fig. 7. *Variation of strain rate along the flow line for x$_0$=4.*

The strain intensity is calculated by numerical integration of the equation (24).

In this aim, we considered the continuity condition and we used the equation:

$$\overline{\varepsilon}_i = \frac{\overline{\dot{\varepsilon}}_{i-1} + \overline{\dot{\varepsilon}}_i}{2} \cdot \Delta t_i \qquad (27)$$

Δt$_i$ is the time necessary for the passing of material particle of the *Δl$_i$* sequence along the flow line.
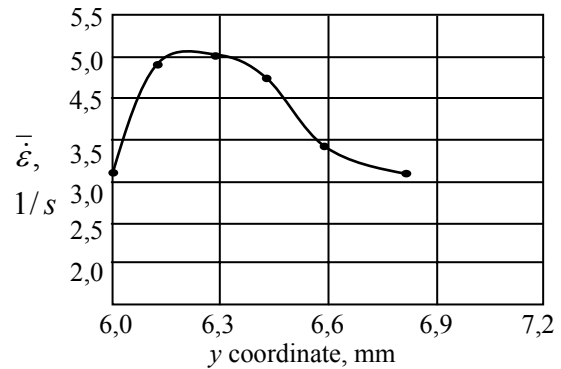
Fig. 8. *Variation of strain rate along the flow line for x$_0$=6.*
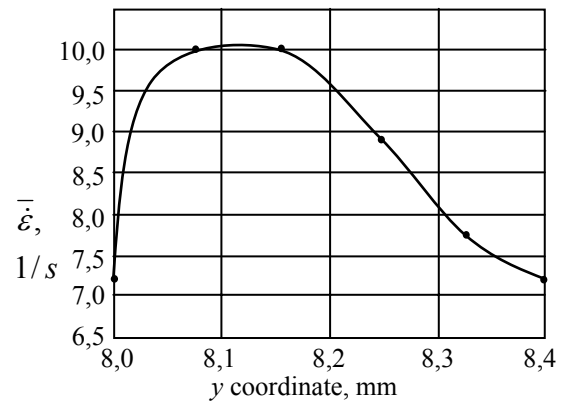
Fig. 9. *Variation of strain rate along the flow line for x$_0$=8.*

This factor is calculated with the equation:

$$\Delta t_i = \frac{4R}{v_0} \cdot \frac{\arcsin\left(\dfrac{\Delta d_i}{2R}\right)}{180} \qquad (28)$$

where

$$\Delta d_i = \sqrt{\Delta x_i^2 + \Delta y_i^2} \qquad (29)$$

The numerical values are written in Table 1. The distribution of the values of partial strain intensity is similar for each flow line.

The graphic of the variation of the partial strain intensity, along the flow line, is showed in Figure 10.

The partial strain rate is great at the entrance of the material in the second deformation domain. Then the value of the partial strain rate decreases.

The cumulate strain rate intensity is showed in Figure 11.

The cumulate strain rate increases and reaches the value of 0.352 – 0.367, a relatively great value.
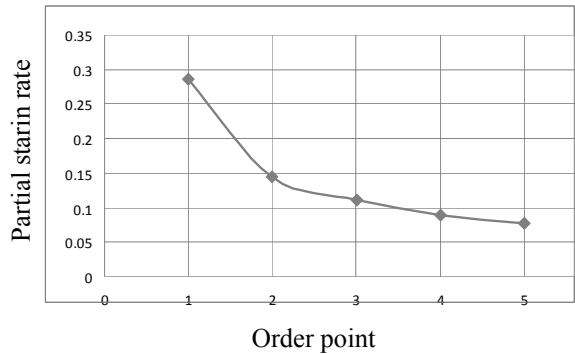
Fig. 10. *Variation of the partial strain rate intensity.*
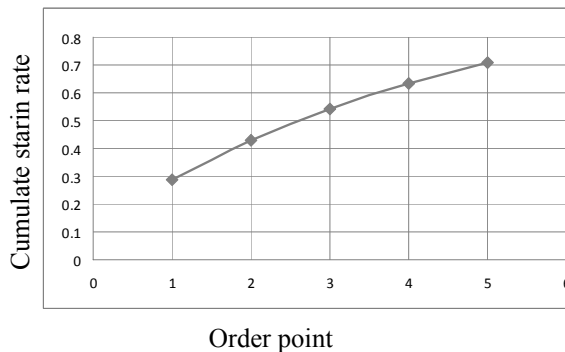
Fig. 11. *Variation of the cumulate strain rate intensity.*

6. Conclusions

The flow lines method allows the solving of the plastic deformation processes, such as the ECAE method.

The ECAE method permits intensive deformation process what leads to severe plastic deformation with a very fine structure.

The paper systematizes the basis aspects for application of the flow line method in case of the equal channel angular extrusion.

References

[1]. R.Z. Valiev, R.K. Islamgaliev and I.V. Alexandrov, Progr. Mat. Sci., 45 (2000) 103-189

[2]. H.S. Kim, M.H. Seo and S.I. Hong, Mater. Sci. Eng., A291 (2000), 86-90

[3]. H.S. Kim, M.H. Seo, S.I. Hong, H.R. Lee, B.S. Chun and K.H. Lee, Mater. Sci. Forum, 386-388 (2002), 421-426

[4]. A. Gholinia, P. Bate and P.B. Prangnell, Acta Materialia, 50 (2002), 2121-2136

[5]. Y. Iwahashi, J. Wang, Z. Horita, M. Nemoto and T.G. Langdon, Scripta Metall. 35, (1996), 143-146

[6]. R.E. Barber, T. Dudo, P.B. Yasskin and T. Hartwig, in "Ultrafine Grained, Materials III", ed. Y.T. Zhu et. al., TMS, 2004, 667-672

[7]. Y. Saito, H. Utsunomiya, H. Suzuki and T. Sakai, Scripta Mater. 42 (2000), 1139-1144

CORROSION RESISTANCE IN NEUTRAL SALINE FOG OF THE COMPOSITES Cu-Mo OBTAINED BY PVD METHOD

V.G. GRECHANYUC[1], N.I. GRECHANYUC[1], Lucica ORAC[2]

[1]Kiev National University of Building and Architecture, Ukraine
[2]University "Dunarea de Jos " of Galati
email: lucia_orac@yahoo.com

ABSTRACT

The basic materials used for electrical contacts, which may be available economically, are the Cu-Mo based composites obtained by the method of electron flow at high temperatures under vacuum.

Cu-Mo (12% max. Mo) composite materials are produced by simultaneous evaporation from separate Cu and Mo crucibles with subsequent condensation of the vapor flow on an OL-37 steel layer of 15 to 20 mm thickness and 800 mm diameter. The surface of the disk-support on which condensation of the vapor flow takes place was machined until a roughness of Ra =0.63 was obtained.

Analysis of chemical composition and structure of composites based on copper and molybdenum content allowed determination of the variation of these elements from layer to layer (of up to 20-25% to 4-5 mas.) and the distribution gradient of these elements in the layers.

The Cu-Mo composites produced by PVD method were introduced in the room and tested in neutral saline fog exposure time of 100h. Cu-Mo composites, obtained by PVD method, have a fairly good corrosion resistance, at Mo concentrations ranging from 8% to 12 % of the surface do not present oxides and the concentrations of Mo between 1,2 to 6% area are covered with oxide.

KEYWORD: PVD method, layer, corrosion, saline fog

1. Introduction

The paper describes reviews referring to determination of working parameters of the development processes of some composites in copper matrix, obtained by vapour-phase deposition method. The molybdenum was used as complementary phase.

Development of the multi-component coatings necessary to enhance the electro corrosive resistance of the electric contact of commutation devices represents one of the future applications of this technology.

An important scientific and practical interest represents the use of the vaporization method involving high rates of electron flows and metal & non-metal condensation, not only having in view the building of coatings on working surfaces of the contacts, but also for development of the massive condensates (MC) necessary for the electric contacts.

In order to obtain composite materials made from Cu-Mo, condensed in the vapor phase, the electron flow industrial system, type UE-189, designed by the Welding Institute of the Academy of Science of Ukraine and updated by the Centre of Scientific Production "Gekont" (CSP "Gekont") was used.

The composite materials of Cu-Mo have been obtained by simultaneous vaporising, from separate crucibles, of copper and molybdenum followed by the vapor flow condensing on a steel OL-37 sub layer, preheated up to 700 ±20 °C. Copper and molybdenum ingots have been used as initial materials obtained by vacuum electron flow remelting. The condensate obtained as plates of 0,7 … 1,2 mm thickness have been used for the study of corrosion resistance [1].

The structure of Cu-Mo composites is under the form of blocks. For each block it is characteristic an arbitrary striped structure. The period of stripes repetition is 150 ± 3 mm.

2. Results and experimental researches

To obtain composite materials based on copper and molybdenum, copper, molybdenum and calcium fluoride powder have been used; their characteristics are presented in Table 1.

Table 1. Material marks that were used to obtain composite materials based on copper and molybdenum.

Materials	Mark	Standard
Cu	M0b, M00, M0, M1, M2	GOST 859-78
Mo	MCVP	TU 48-19--247-87
CaF$_2$	c	GOST 7167-77

For evaporation, use is made of copper ingots of 100mm diameter and 70 mm diameter molybdenum. The ingots were blanked to 98.5, respectively 68.5 mm size to avoid their jam in the evaporation process [2]. Calcium fluoride powder was pressed with a press-type P-457 at a pressure of 240 to 300 MPa, in a number of pills of 30 mm diameter and 15 to 20 mm thickness.

The surface of the disk-support, where vapor flow condensation takes place, was processed up to the roughness of R$_a$ = 0.63.

The ingots of blanked copper and molybdenum are subjected to degreasing with acetone and then they are installed in the crucibles 8 and 9 (Figure 1).
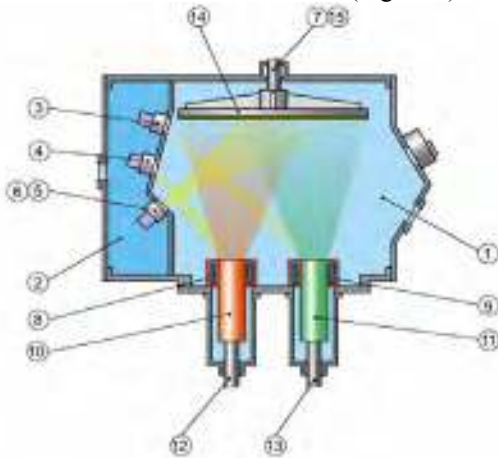
Fig 1. Electron flow installation
1-Technological working room; 2 - gun room, 3,4 (100kW),5,6(20 kW) - electron gun; 7- rod; 8(d=100mm), 9(d=70mm) – cooper crucible; 10,11- material; 12,13,14- assurance mechanisms to advance material, T$_{support}$= 673 … 1073 K

On the surface of the molybdenum ingot the CaF$_2$ pill with a weight of 4 ... 6 g is placed to form the separation layer on the surface of the support of OL-37. After installing and degreasing with acetone of the disc-support, the entire installation is vacuumed. Vacuum is done in 45 to 60 minutes and is 1.3 … 4 · 10^{-2} Pa in the technological room and, 3 · 10^{-2} ... 6.6 · 10^{-3} Pa – in the gun room.

When the needed vacuum pressure is achieved, it starts the disk-rotation mechanism and by means of the guns 5 and 6 heating is achieved up to temperatures of 923 ± 20 K.

The rotation speed of the disc-holder is 36 rpm.

On reaching the required temperature of the disc-support, the electron gun 4 starts and when a current flow of 0,2A and acceleration voltage of 20 kV are achieved, the pill CaF$_2$ is evaporated on the surface of the molybdenum ingot. In these process parameters the molybdenum ingot does not evaporate.

This technological process enables during one cycle to achieve deposition of the separation layer and to further obtain the composite material Cu-Mo without depressurization of the plant. After the separation layer deposition process is complete, between disc 14 and ingots a shutter is installed.

This prevents the vapor flow to reach the support surface with the process of reaching the technological regimes of evaporation of copper and molybdenum alloys.

The shutter being pulled down, the ingot of copper is heated (1.3 ... 1.5 A current flow). At the same time the ingot of molybdenum is heated as well. After completing the process of formatting the intermediate bath and heating the molybdenum ingot, the currents which flow on the ingot surface are brought to 3.2 ... 3.4 A for copper and up to 1.4 ... 1.8 A for molybdenum; the shutter opens and the technological process is performed to obtain the material concerned.

The composite material with a thickness of 0.8 ... 1.2 mm is achieved within 80 to 100 min. The duration of cooling the composite is 3.5 ... 4 h. After this, chamber 1 is depressurized and the composite detaches from the substrate.

The chemical composition of the condensates was determined by chemical-analytical methods [3].

The chemical composition was determined at the Electrotechnical Research Institute in Bucharest, according to STAS STAS 1706/1-85 and 1706/17-71 using spectrometric methods.

The result, which is the arithmetic average of tens of tests on samples with different thicknesses, is presented in table 2.

Table 2. Chemical composition of the composites

Sample code	Chemical composition, %	
	Cu	Mo
1	98.80	1.20
2	96.09	3.91
3	94.90	5.10
4	93.20	6.80
5	91.60	8.40
6	87.70	12.30

By electronic microscopy in cross –section and from the spot analyses EDX it could be noticed the stratified distribution of both molybdenum and copper (Figure 2).
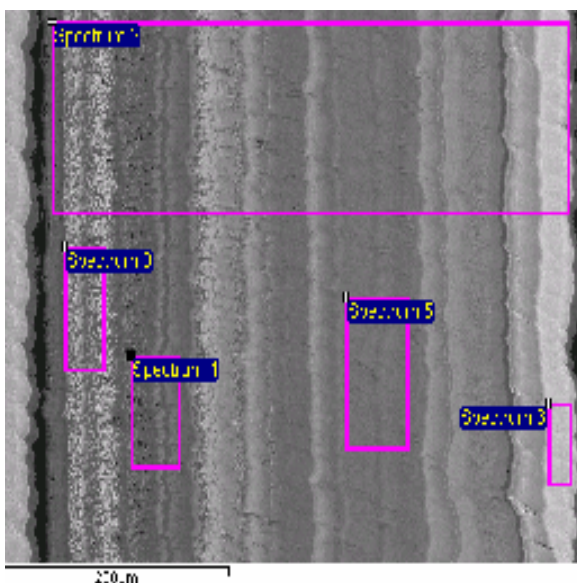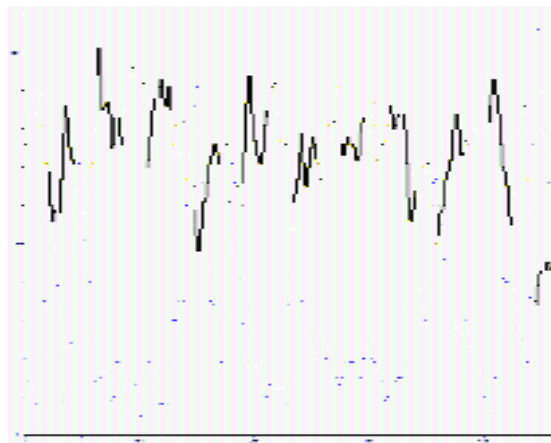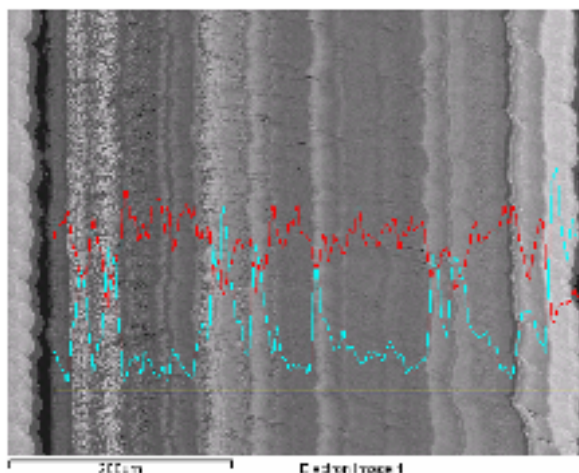
Processing option: All elements analysed (Normalised)
All results in weight%

Spectrum	Cu	Mo	Total
Spectrum 2	91.85	8.15	100
Spectrum 3	91.80	8.20	100
Spectrum 4	92.02	7.98	100
Spectrum 5	92.14	7.86	100
Spectrum 6	91.60	8.40	100

Fig. 2. *Analyses EDX in cross section and spots for the stratified composite, Cu- Mo (8,4% Mo).*

Analysis of the chemical composition and structure of composites based on copper and molybdenum allowed determination of these elements variation from layer to layer (of up to 20-25% to 4-5 mas.) and the gradient distribution nature of these elements in layers [4].

Composites obtained by physical vapor deposition increase, forming chains and conglomerates actually very important because thus increases the resistance to high temperatures [5].

Distribution of molybdenum concentration, upon evaporation from three crucibles, depends on the geometric arrangement of the crucibles. By changing the distance between the central axes of the crucibles an increased concentration of molybdenum in a particular sector of support can be obtained. Thin structure of the composites was investigated by electronic microscopy method using electronic microscope. Metallographic attack was made with 20% HNO_3. For study purpose, samples of material based on copper and molybdenum, a molybdenum content of 12.3% (mas.), copper – remainder were considered. Specificity of the technology for obtaining composites Cu-Mo is a condition of the formation of a special laminated structure (Figure 3).

Composites were obtained in Cu-Mo micro layers with a structure sufficiently balanced by condensation at temperatures above the melting temperature to 0.3 than the melting temperature of the lowest fusible component (°C). Structure of Cu-Mo composites is under the form of blocks. For each block, it is characteristic an arbitrary periodic striped structure. The period of stripes repetition is 150 ±3 μm.
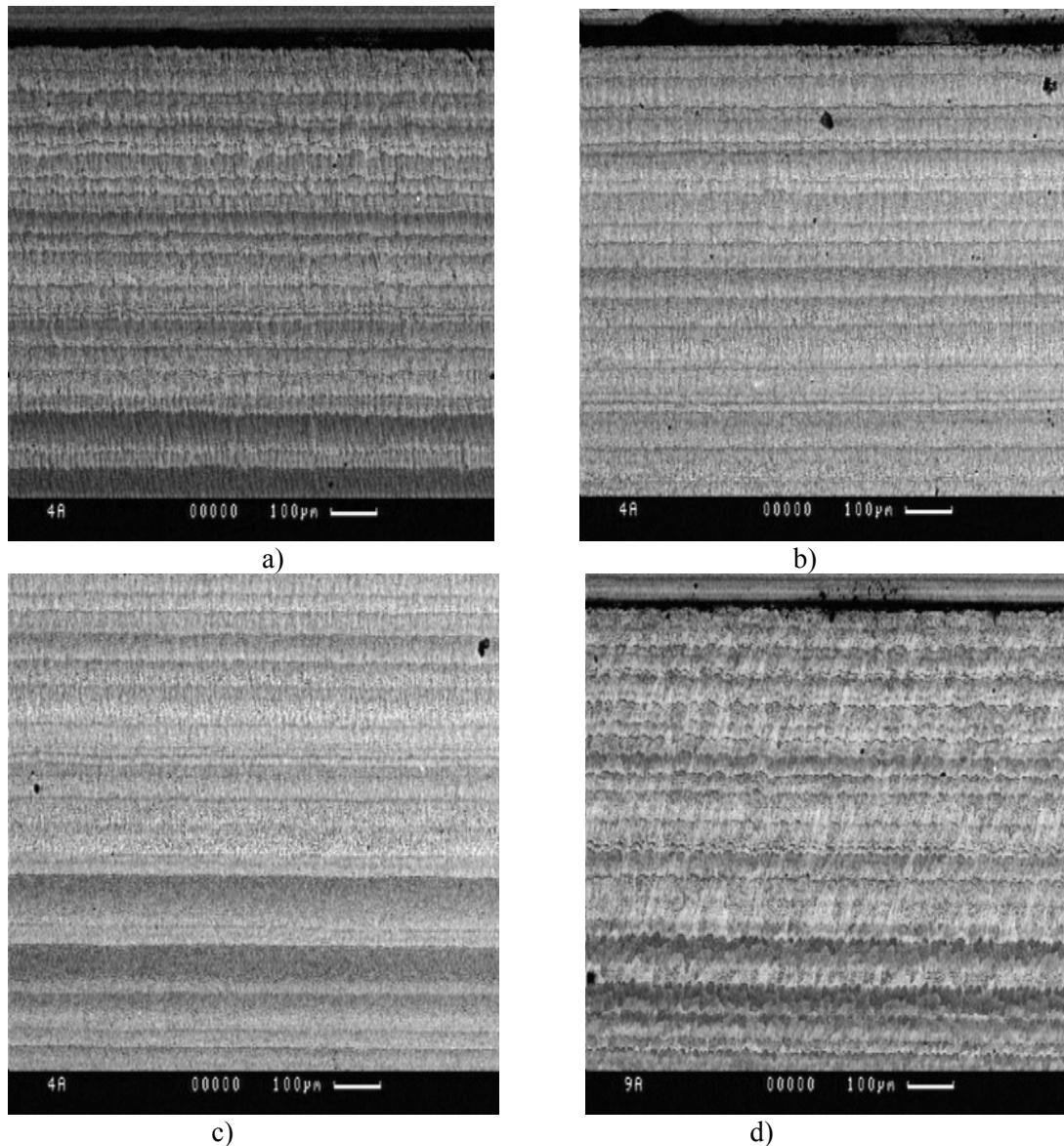
Fig. 3. *Microstructures a) Cu – 3.91% Mo, b) Cu-5.1% Mo, c)-8.4% Mo,*
d) Cu-12.3% Mo magnification x 1000

Such a phenomenon is accounted for by the structure of this composite material which determines the corrosion process progress according to an electrochemical mechanism. In accordance with the Cu-Mo equilibrium state diagram, within the concentration interval, these are not miscible in liquid nor in solid state, and their reciprocal solubility at 900 °C is very low [6].

The corrosion test according to SR ISO 9227/1995, for a period of 100 hours at a temperature of 35°C. The purpose of the test was to detect discontinuities such as pores or other defects.

Initial samples were degreased with acetone, weighed on analytical balance with an accuracy of 0.01 mg and marked with a code. At the end of the test, samples were removed from the room and were left to dry for 30 minutes.

To determine the mass loss, the corrosion products were removed by etching in 50% hydrochloric acid solution (volumetric concentration), and the inhibitor was added 3.5g/L hexamethylene.
Velocity values of corrosion and penetration indices when testing for corrosion in saline fog are given in Table 3.

Table 3. *Behavior of Cu-Mo Composite obtained by PVD method, when tested in saline fog*

Sample	Weight difference	Corrosion rate	Penetration index	Resistance group	Observations
	[g]	[g/cm^2·h]	[mm/an]		
Cu – 1.2% Mo	0.0008	0.20	0.18	Rezistance	Non-adherent Oxide spots emergence on~80% of the area
Cu - 3.91% Mo	0.0006	0.15	0.12	Rezistance	Non-adherent Oxide spots emergence on~60% of the area
Cu – 5.1% Mo	0.0004	0.10	0.07	Rezistance	Non-adherent Oxide spots emergence on~10% of the area
Cu – 6.9% Mo	0.0004	0.10	0.07	Rezistance	

As shown in Figure 4, Cu-Mo composites, obtained by PVD method, have a fairly good corrosion resistance, at Mo concentrations ranging from 1.2 to 5.1% area is covered with non adhering oxide and the concentrations of Mo between 6.8 to 12.3% of the surface do not present oxides.

Cu – 3.91% Mo   a)   b)

Cu – 5.1% Mo   a)   b)

Cu – 6.9% Mo   a)   b)
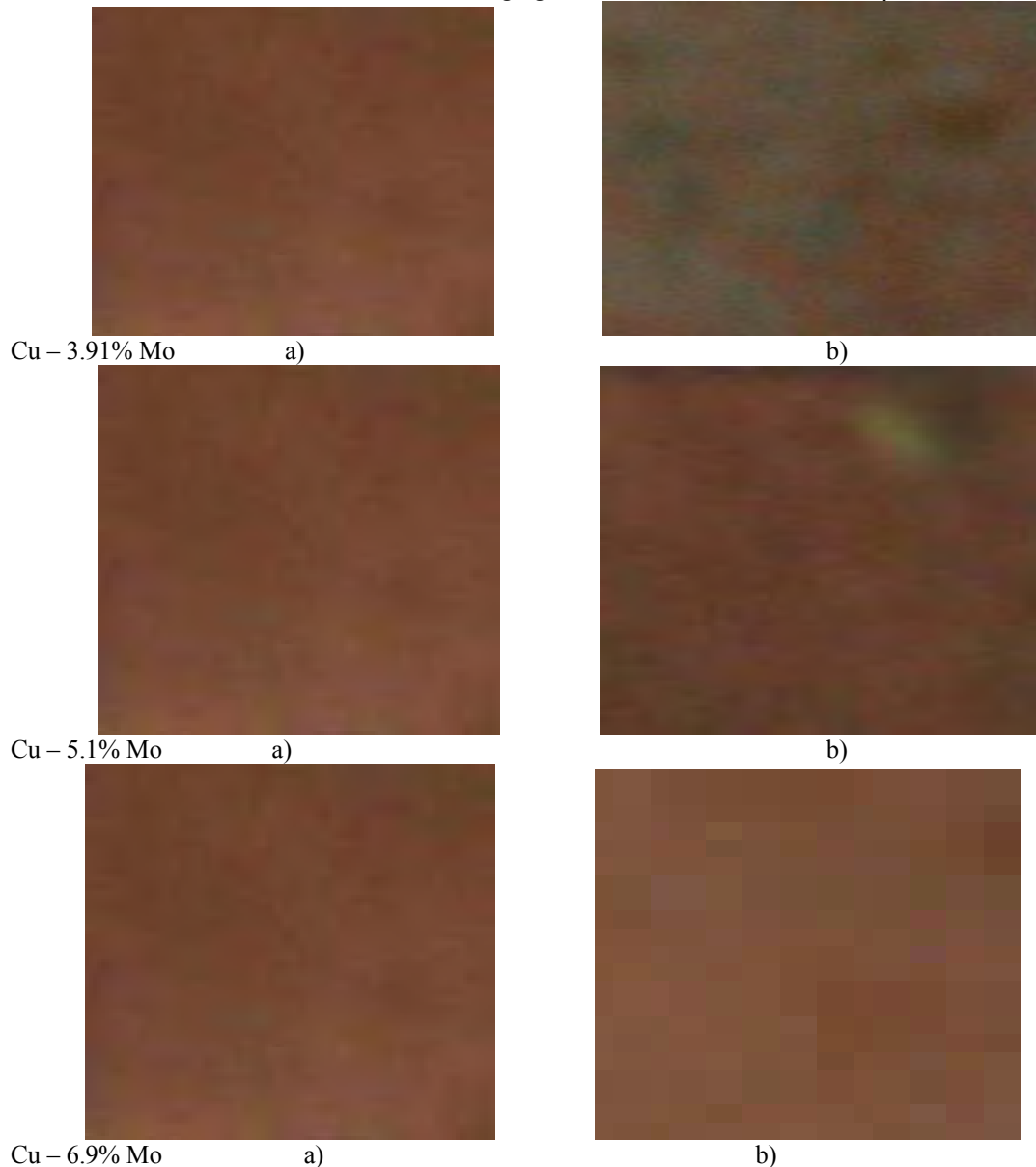
Fig. 4. *Macrostructures of coatings: a) before corrosion, b) after corrosion, magnification x 50.*

This is actually an adherent oxide coating, the penetration index remains unchanged. In saline fog, tests have shown that the corrosion resistance of the composites obtained by PVD method is higher than pure copper.

3. Conclusions

Analyses of chemical composition and structure of composites based on copper and molybdenum content allowed determination of the variation of these elements from layer to layer (of up to 20-25% to 4-5 mas.) and the distribution gradient of these elements in the layers. The composites obtained by physical vapor deposition increase, forming chains and conglomerates actually very important because they increase the resistance to high temperatures. Cu – Mo composites were obtained in micro-layers with a structure sufficiently balanced by condensation at temperatures above the melting temperature to 0.3 than the melting temperature of the component with the lowest fusibility (°C). In saline fog, tests have shown that the corrosion resistance of the composites obtained by PVD method is higher than pure copper.

References

[1]. **N.I. Grechanyuk, V.A. Osokin and I.B. Afanasiev,** *Electron flow technology for electric contact materials*, Electrical contacts and electrode, Sb. Tr. - Kiev: IMP NANU, 1998, pp. 51-66.

[2]. **M.I. Grechanyuk, V.O. Osokin and I.B. Afanasiev**, *Composite materials for electric materials and obtaining method*, Pat. 34875 Ukraina. MPK C23C/20, Bul. Nr.12, 2002.

[3]. **B.A. Movcian, V.A. Osokin, L.V. Pusecinicova, N.I. Grechanyuk,** *Electron flow evaporation and copper condensation using intermediary creuset*, Issues of power metallurgy, Nr. 3, 1991, pp. 58-61

[4]. **V.G. Grechanyuk, L. Orac, V.A. Denisenko**, *Studies and research on mechanical properties and the influence of structural defects for the Cu-Mo composite material*s obtained using the PVD metod, Proceedings GEOENV 2008, Geoenvironment and Geotechnics, Publisher by Heliotopus Conferences, ISBN 978-960-6746-01-7, Millos, Greece, 2008

[5]. **V.G. Grechanyuk, V.A. Denisenco, L. Orac** *Structurre and corrosive firmness of composition materials on basis of copper and molybdenum electron beam technology metod*, The Annals of 'Dunărea de Jos' University of Galaţi, Fascicle IX Metallurgy and Material Science,Vol. Nr. 1, 2007.

[6]. **V.G. Grechanyuk, V.A. Denisenko, I.F. Rudenko, L. Orac**, *Anticorrosive stability of cooper- molybdenum composites for electrical contacts*, Electrical contacts and electrode, Kiev I.N. Frantevicia NAN Ukraina, 2008, pp. 129-133.

ELECTROCHEMICAL CORROSION PROPERTIES OF SiC/Ni NANO-COMPOSITE COATINGS IN 0.5M NaCl

Lidia BENEA[1], Viorel DRAGAN[1], Bernard TRIBOLLET[2]

[1]Competences Center: Interfaces–Tribocorrosion and Electrochemical Systems (CC-ITES),
Dunarea de Jos University of Galati,
[2]Laboratoire Interfaces et Systemes Electrochimiques, Université Pierre et Marie Curie Paris, France.
email: Lidia.Benea@ugal.ro

ABSTRACT

Nano particles have an influence on nickel electrocrystallisation steps: decreasing charge transfer resistance and activating the nickel reduction. The SEM – EDX surface morphology and TEM structure of the electrodeposited nano-composite were investigated. The dispersed particles perturb the nickel crystal growth resulting in a random rather than in a preferred orientation. The corrosion behaviour of the nano-composite coatings was evaluated in the solution of 0.5M NaCl at room temperature. It was found that the polarization resistances of nano-SiC–nickel composite coatings are higher compared pure nickel coatings. The SiC distribution in the nano-composite coatings at low concentrations of SiC in bath was uniform across the coatings. The incorporation of the SiC nano-particles leads to the changes in the morphology and corrosion resistance of the nano-composite coatings as compared to the pure nickel coatings. The Ni–SiC nano-composite coatings have higher corrosion resistance than the pure nickel coating, which is attributed to the grain-fining and dispersive strengthening effects of the co-deposited SiC nano-particles with nickel.

The silicon carbide nano particles embedded during nickel electroplating have a good effect to corrosion properties of composite coating compared to pure nickel coating.

The polarization resistance increases about two times and the corrosion current density decreases about two times in the case of nano-composite coating.

KEYWORDS: nanocomposite, coatings, electrodeposition, dispersed phase, corrosion

1. Introduction

The goal of composite development is to achieve a combination of properties not achievable by any of the materials acting alone.

The electrochemical deposition of nano size particles in a metallic matrix has led to a new generation of composites, due to the advantages of this technique. Studies by several investigators have proved that the uniform dispersion of the codeposited particles leads to the improvement of the mechanical, tribological, anti-corrosion and anti-oxidation properties of the coatings [1–3]. A large volume fraction of particles is also needed, since they act as load bearing elements.

The ability to produce reinforcing powders with decreasing particle sizes has led to technological interest in the production of new composite materials with improved and well controlled properties. The major challenges in the codeposition of nanoparticles seem to be the codeposition of a sufficient number of particles, and avoiding the agglomeration of particles suspended in the plating solution. SiC/Ni composites in particular have been investigated, due to their improved wear resistance.

This property has led to their commercial use in the protection of friction parts, combustion engines and casting mould [4, 5]. Considerable research has been focused on the impact of the electrodeposition parameters: bath composition, presence of additive, pH, current conditions and type of SiC particles [6 - 12]. Reports on the tribological properties of SiC/Ni deposits containing micron and submicron SiC particles are available [1, 13 - 17].

Composite coatings are produced by codeposition of inert particles into a metal matrix from an electrolytic or electroless bath being considered as metal matrix composite (MMC) coatings. This technique is receiving increased interest because of its ability to produce films with excellent mechanical properties such as wear resistance, corrosion resistance and lubrication [2-6]. These properties depend on the morphology of the inert particles in the composite coatings. Furthermore, metal matrix nanocomposite coatings exhibit unique magnetic, mechanical and optical properties and are promising materials for micro-devices. Nano-composite deposition may be useful in fundamental studies of their nanometric nature. As mentioned above not many reports are available on the corrosion performances of SiC/Ni composite coatings particularly the electrochemical corrosion. It is therefore interesting to study the influence of incorporated nano SiC particles into the coating, which thereby can affect the properties of the coating. To understand the effect of nano SiC (20 nm mean diameter) particles samples with nanostructued SiC/Ni composite coatings were prepared by electrodeposition in a common nickel plating bath by adding 20 g/L SiC (20 nm size) in the electrolyte. A comparison has been made with reference to pure Ni coating obtained from the same electrolyte.

2. Experimental research

2.1. SiC/Ni nano-coatings preparation

The SiC/Ni composite nano-coatings were prepared in a solution containing 260 g/L $NiSO_4$ x $6H_2O$, 30 g/L $NiCl_2$ x 6H2O, 30 g/L H_3BO_3, 20 g/L nano-sized SiC (20 nm mean diameter) and surfactant. The nano sized SiC particles from a TEM image are shown in Figure 1. Electrodeposition was carried out on vertical electrodes, and the bath was agitated during electrodeposition with a magnetic stirrer.
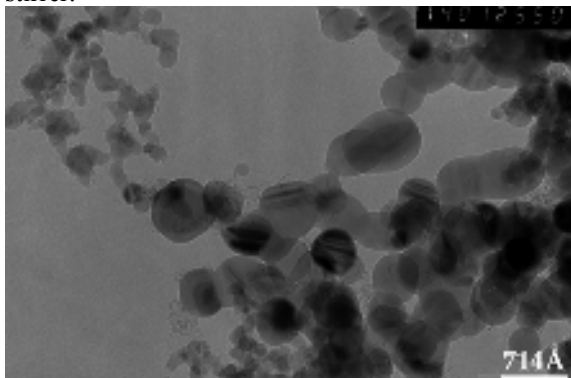
Fig. 1. TEM image of SiC nano particles (mean diameter of 20nm).

The temperature of the electrodepositing bath was maintained at 40 ^{0}C and its pH was adjusted to 4.0. A steel plate with dimensions of 50 mm x 80 mm x 1 mm was used as the base plate for the electrodeposition, and the anode was a pure nickel plate. For comparison, pure Ni coatings were also prepared in almost the same solution mentioned above except for SiC particles. In order to standardize the comparison, the thickness of all coatings was controlled at 100 μm.

2.2. Electrochemical corrosion

The solution used for thecomparative study of pure and nanocomposite coatings deposited on steel support was 0.5M NaCl. Corrosion investigations were taken out by electrochemical impedance spectroscopy method in the frequency range from 10^4 Hz to 0.003 Hz with amplitude of 5 mV and potentiodynamic diagrams. After impedance measurements potentiodynamic curves were plotted with a scan rate of 0.5 mVs^{-1} between the potentials: – 600 mV and +600 mV (referred to Ag/AgCl electrode). Corrosion current densities, polarization resistance, Tafel slops and corrosion potential were determined in 0.5 M NaCl naturally aerated solution.

3. Results

3.1. SEM – EDX and TEM studies

Surface morphologies of SiC/Ni and pure nickel films deposited are examined using a SEM with EDX system and the presence of SiC dispersed particles inside the composite coatings by TEM. The images are given in Figures 2-3. The surfaces of the films appear to be smooth and densely covered. The crystallites, however, get finer when deposited nano SiC dispersed particles with nickel.
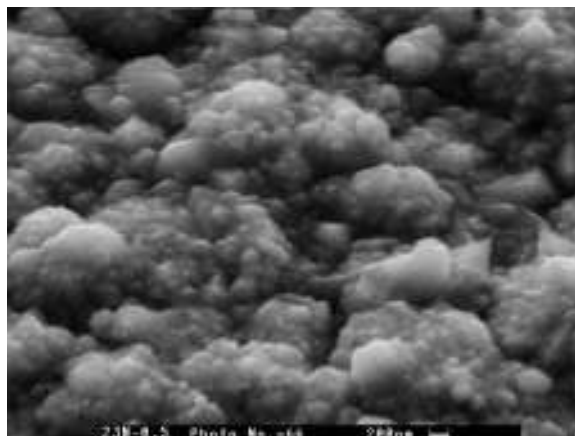
Fig. 2. SEM image of SiC/Ni nanocomposite coating surface.

Fig. 2 shows the SEM image of SiC/Ni nanocomposite coatings. The grain size of the composite coated sample was smaller when compared to the pure nickel coating. The presence of SiC provides more nucleation sites and retards the crystal growth and hence the composite coatings samples possess smaller grain size [10]. The nano SiC particles inside o composite coating were visualised by TEM, see Fig. 3.
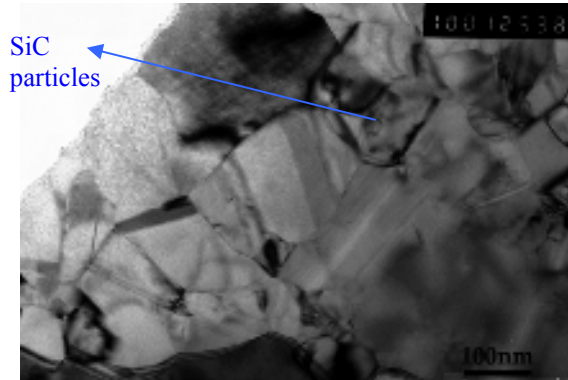
Fig. 3. *TEM image inside of SiC/Ni nanocomposite coating*

From EDX analysis of SEM surfaces silicon content was calculated and transformed after wards in SiC content.

Fig. 4 shows the EDX spectrum of SiC/Ni composite coating surface having 6.29 % of Si layer (A), which represents general analysis on SEM surface. On the layer (B) from Fig 4 a punctual analysis on a SiC particle is shown.

The nano SiC content in the tested nanocomposite coatings was 8.99 as weight % or ~25 as volume %.
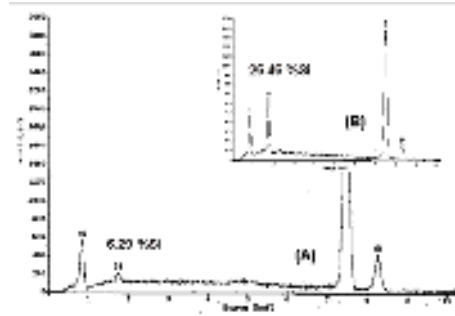
Fig. 4. *SEM-EDX analysis of SiC/Ni nanocomposite surface: Layer (A) – general analysis on entire surface; Layer (B) punctual analysis on SiC particle*

3.2. Electrochemical corrosion studies in 0.5M NaCl

The results of corrosion testing of nano-SiC/Ni composite and pure nickel coatings in aerated 0.5M NaCl solution, pH=7, are presented in Figs. 5 and 6. The test was performed during 24 hours. The polarization resistance of composite coatings, see Fig. 7 is increasing from R_p=600 kΩcm^2 to 1600 kΩcm^2 during the experiment.

Oppositely, the polarization resistance for pure nickel coating (See Fig. 8) is decreasing from about 140 kΩcm^2 after 10 hours and increases slowly at about 160 kΩcm^2 after 24 hours.

It can be observed also that the polarisation resistance of nanocomposite coatings is higher than the one of pure nickel coatings (Figures 5 and 6).
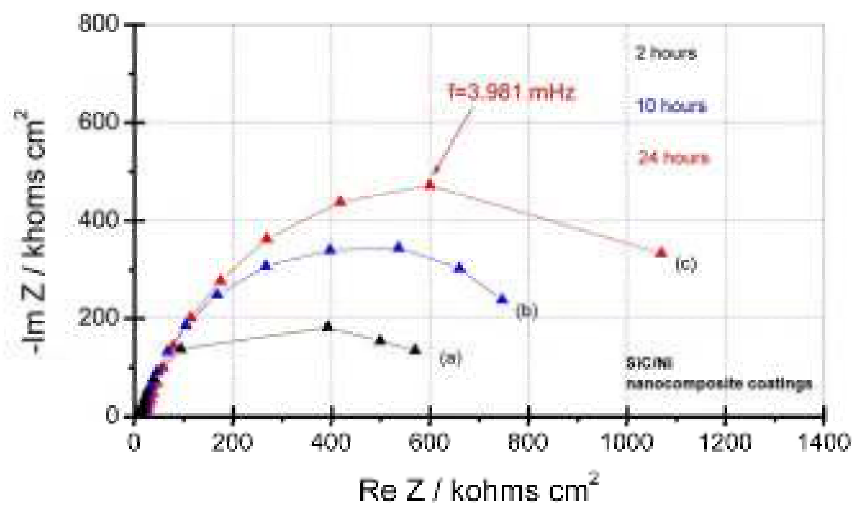
Fig. 5. *Nyquist plot of impedance data of SiC/Ni nanocomposite coatings in aerated 0.5 M NaCl: (a) after 2 hours of immersion; (b) after 10 hours; (c) after 24 hours. The line connecting the points represents the simulation diagram.*
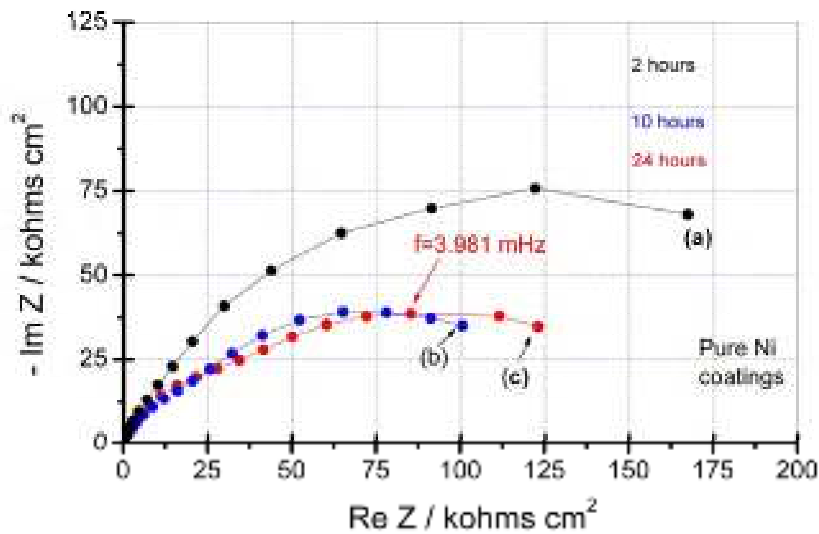
Fig. 6. *Nyquist plots of impedance data of pure nickel coatings in aerated 0.5 M NaCl*
(a) after 2 hours of immersion; (b) after 10 hours; (c) after 24 hours
The line connecting the points represent the simulation diagram.

One equivalent circuit was proposed to fit the experimental impedance data [18]. In the composite coatings corrosion experiments this circuit, represented in the Fig. 7, allow obtaining an excellent agreement between experimental data and simulated impedance plots.
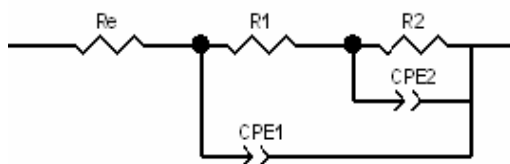
Fig. 7. *Equivalent circuit proposed to fit the experimental impedance data of SiC/Ni nanocomposite and pure Ni coatings immersed in 0.5 M NaCl solution*

The experimental data was simulated with this equivalent circuit, where:
R_e – electrolyte resistance between the reference electrode and the working electrode;
CPE_1 – the double layer capacitance depending on frequency of nickel coating or nanocomposite coating;
CPE_2 - double layer capacitance depending on frequency of pores (in the case of nickel coating, or double layer capacitance depending on frequency of insulating SiC nano-particles).
R_1 – the polarization resistance of nickel or nanocomposite coatings.

R_2 - resistance of pores (in the case of pure nickel coating) or resistance of insulating nanoparticles in the case of nanocomposite coatings.

The impedance could be described by the following equation:

$$Z = R_e + \frac{R_p}{1 + (j\omega\tau)^\beta} \quad (\text{with } 0 < \beta \le 1) \quad (1)$$

The value of β determines the amplitude of the depressed impedance semi-circle and the importance of the discrepancy between the Randles' circuit model with a pure capacitor C_{dl} and the equivalent circuit with the CPE insteade of C_{dl}. The borderline case of the Randles' circuit is found if $\beta = 1$. CPEs are constant phase elements, accounting for the fact that the centres of the capacitive arcs of the impedance circle are under the axis of real part. This feature of capacitive arcs is encountered in all electrochemical impedance studies performed on inhomogeneous surfaces and has given rise to extensive studies. CPE are not pure capacitors but components depending on frequency.

The proposed equivalent circuit fitted better the experimental data as it is shown in Figs 5 and 6 as lines connecting the experimental points of the impedance measurements.

Evolution of the polarisation resistance (R_1) of pure nickel coatings and nanocomposite coatings during the experiment is presented in Figure 8 and evolution of the CPE_1 in Figure 9.

The continuous increases of capacitance (CPE) for pure nickel coatings can be explained by the increases in the permittivity of the coating and/or increases in porosity due to the pitting corrosion installed in chloride solution.

The decreases of capacitance for nanocomposite coating can be explained by improving the passivity film protection on the composite surface due to the presence of insulating SiC nanoparticles.
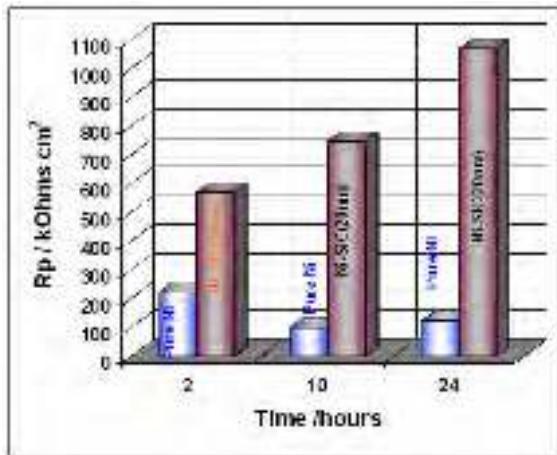
Fig. 8. *Evolution of polarisation resistance during immersion time in 0.5M NaCl solution.*

From the evolution of polarisation resistance diagrams during immersion time it is shown the same differences between nanocomposite and pure nickel

coatings, increase in the polarization resistance for nanocomposite coating and decreasing the polarization resistance for pure nickel coatings.

The corrosion current densities of both type of coatings were calculated from potentiodynamic diagrams plotted in 0.5 M NaCl solution with a scan rate 0.5 mVs^{-1}.
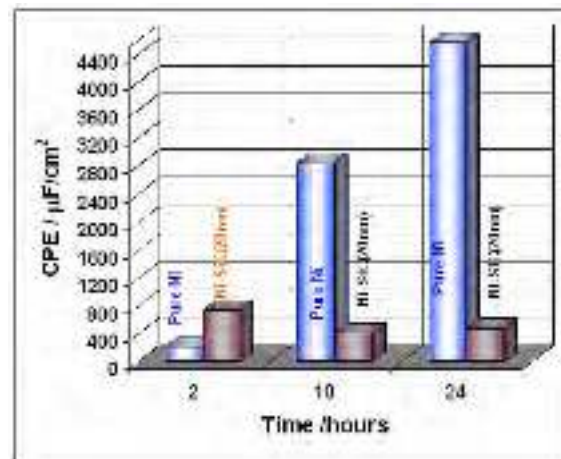
Fig 9. *Evolution of CPE_1 during the immersion time in 0.5M NaCl solution.*

From the potentiodynamic diagram of nanocomposite coating, curve [b] in Fig. 10, the calculated corrosion current density has a value of i_{corr}=65.06nAcm^{-2} and a corrosion potential situated at E_{corr}= −169mV (Ag/AgCl).
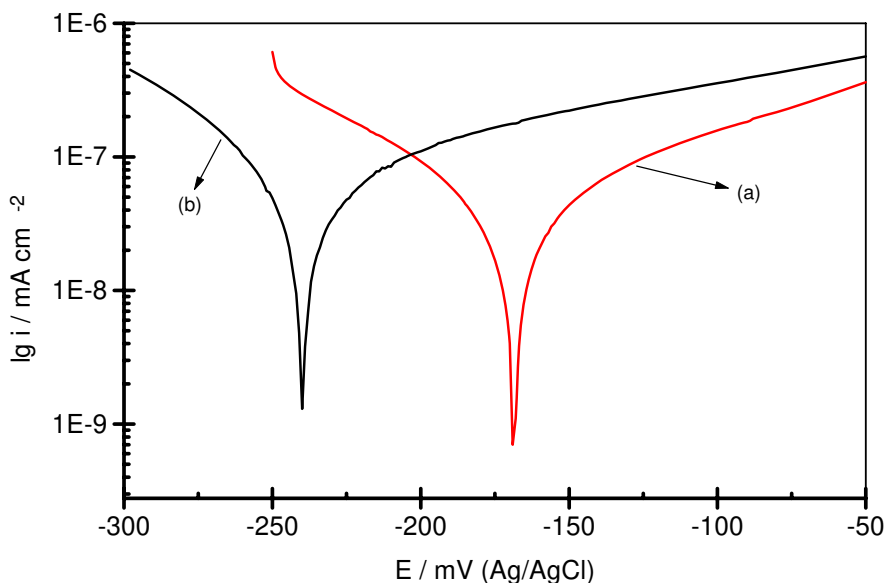
Fig. 10. *Potentiodynamic diagrams of: (a) nickel SiC composite coating and (b) pure nickel plating in aerated 0.5M NaCl; scan rate 0.5 mV/s.*

The corresponding Tafel slopes were the following: B_a=161.5 mV/decade and B_c=101.9 mV/decade for anodic and cathodic reactions, respectively.

From the potentiodynamic diagram performed on pure nickel coating, curve [b] in Fig. 10, the calculated corrosion current value is i_{corr}=178nAcm^{-2} with a corrosion potential situated at E_{corr}= –236mV (Ag/AgCl). The corrosion potential is shifted with about 66 mV to more negative values that in the case of nanocomposite coating.

The corresponding Tafel slopes were the following: B_a=380mV/decade and B_c=133 mV/decade for anodic and cathodic reactions respectively.

We can conclude that the silicon carbide nano particles embedded during nickel electroplating process have a good effect to corrosion properties of nanocomposite coatings compared with pure nickel coatings. The polarization resistance increases about two times and the corrosion current density decreases about two times in the case of nanocomposite coating.

4. Conclusions

SiC nano-particulates can be successfully co-deposited with nickel by electrodeposition process from a nickel plating bath.

The benefit of presenting codeposition results was demonstrated for the codeposition of SiC/Ni with particle sizes having a mean diameter of 20 nm. For this system, it was found a better corrosion resistance.

The incorporation of the SiC nano-particulates leads to the changes in the surface morphology, grain sizes and corrosion resistance of the nano-composite coatings as compared to the pure nickel coatings.

The SiC/Ni nano-composite coatings have higher polarization resistance and better corrosion resistance than the one pure nickel coating in chloride containing solution, which is attributed to the grain-fining and dispersive strengthening effects of the deposited hard SiC nano-particulates.

The values of polarization resistances of pure nickel and SiC/Ni nanocomposite coatings determined by two electrochemical methods, electrochemical impedance spectroscopy and potentiodynamic polarization respectively are in good agreement.

The improved properties of SiC/Ni nano-composite coatings must be tested also to other applications, on the better resistance to bacterial adhesion and biofilm formation compare to pure nickel coatings.

Acknowledgments

References

[1]. **Nabeen K. Shrestha, Masabumi Masuko, Tetsuo Saji,** Wear 254 (2003) 555.

[2]. **F. Hu, K.C. Chan,** Applied Surface Science 233 (2004) 163.

[3]. **F. Hu, K.C. Chan**, Applied Surface Science 243 (2005) 251.

[4]. **Lidia Benea, Pier Luigi Bonora, Alberto Borello, Stefano Martelli**, Wear 249 (2002).

[5]. **S.H. Yeh, C.C. Wan**, Journal of Applied Electrochemistry 24 (1994) 993.

[6]. **P. Gyftou, M. Stroumbouli, E.A. Pavlatou, P. Asimidis, N. Spyrellis**, Electrochimica Acta 50 (2005) 4544.

[7]. **Ming-Der Ger**, Materials Chemistry and Physics 87 (2004) 67.

[8]. **C.T.J. Low, R.G.A. Wills, F.C. Walsh**, Surface and Coatings Technology 371–383 (2006) 201.

[9]. **Sheng-Chang Wang, Wen-Cheng J. Wei**, Materials Chemistry and Physics 78 (2003) 574.

[10]. **Lidia Benea, Pier Luigi Bonora, Alberto Borello, Stefano Martelli, Francois Wenger, Pierre Ponthiaux , Jacques Galland**, Solid State Ionics 151 (2002) 89.

[11]. **Maria Lekka, Niki Kouloumbi, Mauro Gajo, Pier Luigi Bonora**, Electrochimica Acta 50 (2005) 4551.

[12]. **Nabeen K. Shrestha, Ichiro Miwa, Tettsuo Saji**, Journal of Electrochemical Society 48 (2) (2001) C106.

[13]. **I. Garcia, J. Fransaer, J.P. Celis**, Surface and Coatings Technology 148 (2001) 171.

[14]. **K.H. Hou, M.D. Ger, L.M. Wang, S.T. Ke**, Wear 253 (2002) 994.

[15]. Maria **Lekka, Niki Kouloumbi, Mauro Gajo, Pier Luigi Bonora**, Electrochimica Acta 50 (2005) 4551.

[16]. **Lei Shi, Chufeng Sun, Ping Gao, Feng Zhou,Weimin Liu,** Applied Surface Science 252 (10) (2006) 3591.

[17]. **Lidia Benea, Pier Luigi Bonora, Alberto Borello, Stefano Martelli**, Wear 249 (2002) 995.

[18]. **Lidia Benea, Bernard Tribollet, Marilena Mardare**; *Electrochemical corrosion behaviour of nano SiC-Nickel composite coatings*. Conference presented at International Conference of Physical Chemistry Romphyschem-13; September 3 - 5, 2008, Bucharest – Romania.

PHYSICO-MECHANICAL AND PHYSICO-CHEMICAL PROPERTIES OF BIO-INERT COMPOSITE CERAMICS

Anna PETROVA[1], Silvia SIMEONOVA[1], Radoslav VALOV[2] and Vladimir PETKOV[2]

[1]Space Research Institute, Bulgarian Academy of Sciences, Sofia, Bulgaria
[2]Institute of Metal Science, Bulgarian Academy of Sciences, Sofia, Bulgaria
email: ani@phys.bas.bg

ABSTRACT

Bio-inert ceramics are non-toxic, non-allergenic and non-carcinogenic materials which explain why these are frequently used as orthopedic and dental implants. Unfortunately, these are chemically inert and do not naturally form a direct link with the bone. The research carried studies micro/nanostructure properties and the porosity of the TiO_2-Nb_2O_5 ceramics, used as biocompatible polymer matrix, prepared by different technological regimes. The morphology of the composite samples of TiO_2-Nb_2O_5 was studied using scanning microscopy. The phase identification of the composites was carried by metallographic microscopy. Results obtained show the chemical composition, the technological parameters and the porosity determined, favors formation of sufficiently strong bond between the studied materials and vitreous carbon layers.

KEYWORDS: bio-inert ceramics, physico-mechanical, physico-chemical properties

1. Introduction

The class of ceramics used for repair and replacement of diseased and damaged parts of musculoskeletal systems are termed bioceramics.

Bioceramics have become a diverse class of biomaterials presently including three basic types: bioinert high strength ceramics, bioactive ceramics which form direct chemical bonds with bone or even with soft tissue of a living organism; various bioresorbable ceramics that actively participate in the metabolic processes of an organism with the predictable results (1). Alumina (Al_2O_3), Zirconia (ZrO_2) and carbon are termed bioinert. Bioglass and glass ceramics are bioactive [1-4].

The aim of the present paper is to examine the change of structure and phase composition of the inert bioceramic material based on TiO_2 with small additions of Nb_2O_5 with nanosized vitreous carbon layers for orthopedic implants.

2. Samples preparation

The studied ceramic substrate specimens, were prepared by mixing TiO_2 and Nb_2O_5 powders in proportions ensuring concentration of 8 wt.%. Nb_2O_5 in the final product. The choice of Rutile as base powder of the mixture is due to its structure. The preparation of the samples is described in details in [Teodosiev and all Artcast Galati] [5].

3. Apparatuses used for measurements of surface morphology – micro/nanostructure

For the investigation of ceramic microstructures and the identification of flaws and defects, the use of light optical microscopy Neophot 32 and digital camera ProgRes C14 JENOPTIK was used.

The nanostructure has been studied by a NanoScan Microscope NanoScan (Figure 3) is presents a scanning microscope that works in a regime of rigid contact and does not require vacuum.

The NanoScan unit has been delivered and made by TISNCM [6, 7]. The main characteristic feature of NanoScan is the use of piezoresonance probe having high bending stiffness of the cantilever. The tests have been performed at the regime of resonance oscillations measuring the contact between the probe tip and the surface, analyzing two parameters: change of amplitude A and frequency F of the probe tip oscillations.

NanoScan Measurement System allows measuring both the topography and mechanical properties. Moreover, NanoScan allows loading and scratching the surface by the probe tip and measuring the hardness. For this purpose, scanning and scratching followed by new scanning have been made to evaluate the sample hardness in comparison with a standard.

For elasticity determination dynamic measurements during loading-unloading process with oscillated probe tip have been performed.

Fig. 1. Scanning Probe Microscope NanoScan.

4. Results and discussion

Fig.2 shows the ceramic's microstructure with different morphology of grains, and large pores. Fig.3 shows the hardness measurements carried on conventional microhardness machines with Knoop or Vickers diamond indenters.

These machines make impressions whose diagonal size is measured with an attached optical microscope. The procedure for testing is very similar to that of the standard Vickers hardness tests, except that it is done on a microscopic scale with high precision instruments.

The surface tested generally requires a metallographic finish; depending on the load used; the smaller the load, the higher the surface finish required. Knoop tests are good for very hard brittle materials and very thin sections.

For the ceramic material tested here, it was determined that the Knoop hardness is between 1000kg/mm^2 and 1050 kg/mm^2.
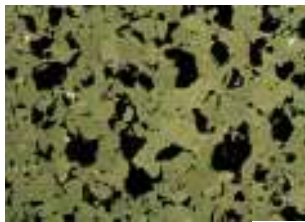
Fig. 2. Microstructure of the TiO_2 - Nb_2O_5 ceramics.
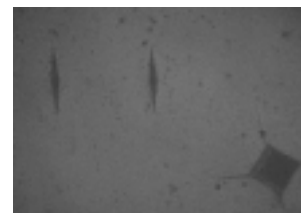
Fig. 3. Knoop and Vickers marks.

The sample surface roughness, the elastic module and hardness before and after coating were scaned and measured (see Fig. 4). The coating improves the surface roughness, and improves the mechanical properties of the samples. Statistics TiO_2 - Nb_2O_5 ceramics shows that the average particle size is **Rms** = 5,67nm.

Roughness (for surface 6.64 X6, 64 um) is **Ra** = 4,12 nm. Measured values are: Elastic module: 185-230 GPa, Hardness **H**=4,1- 6,7 GPa.
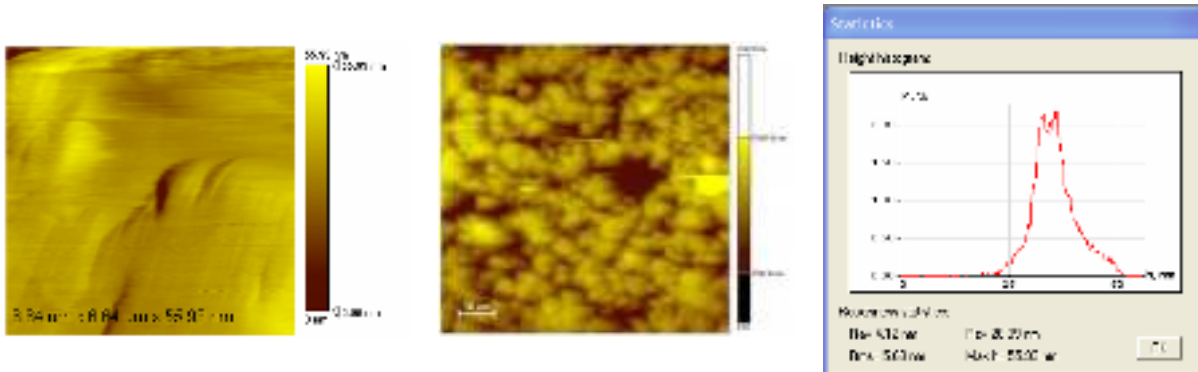
Fig. 4. *Nanostructure of sample TiO_2 - Nb_2O_5 ceramics*

At the same time we studied the system Al_2O_3 - ZrO_2, where the obtained ceramic material possesses better mechanical properties. The coating with VC of this ceramic composite and the evaluation of its coefficient of friction will be a subject of another study.

The Al_2O_3 - ZrO_2 system to long time has been attracting the investigators attention as far as the two oxides do not interact with each other up to 1700^0C and they are in a state of mechanical mixture. Because of that they mutually hinder their grain growth during sintering. As a result a ceramic composite with very fine structure corresponding to very high strengths is obtained [8-10]. This based on alumina and zirconia composite is characterized with high compressive and bending strength, high hardness and wear resistance.

We investigated the mechanical properties of the composite material in the Al_2O_3 - ZrO_2 system with different content of the two oxides and the influence of the temperature treatment. Preliminary synthesis is made aiming at partial stabilization of the ZrO_2 with Y_2O_3.

The sintering of the composite material is carried out at temperature up to 1680^0C. The obtained composite ceramic possesses high hardness – 90 HRA, compressive strength - 1650 MPa and bending strength - 260 MPa.

The zirconia is preliminary partially stabilized with 3.0 wt. % Y_2O_3 at temperature 1350^0C for one hour. The raw materials are mixed and homogenized in planetary mill during six hours in isopropyl alcohol environment.

The received finely dispersed powders are dried and granulated with plasticizers as carboxymethyl cellulose, polyvinyl alcohol, etc. Cylindrical samples with dimensions 15x15 mm and prisms 5x5x45 mm are pressed with pressure 250 MPa from the obtained semidry mass.

The samples are sintered in two stages: to 1400^0C with holding time of 1 ½ hours and then to 1630^0C or 1680^0C in high temperature furnace.

We studied four compositions with different content of the two basic oxides. The mechanical properties – compressive and bending strength of the above cited compositions are determined (*Table 1*).

Table 1. *Composition and properties of the samples vs. the sintering temperature*

Composition No	Al_2O_3 wt. %	ZrO_2 wt. %	Compressive strength MPa		Bending strength MPa	
			1630^0C	1680^0C	1630^0C	1680^0C
1.	86	14	700	935	90	115
2.	83	17	890	1340	115	195
3.	80	20	1045	1580	118	260
4.	77	23	805	1430	97	185

The change of the compressive and bending strength depending on the content of the two oxides and the modifying additives at different sintering temperatures is displayed graphically in *Figure 5* for the compressive strength and in *Figure 6* for the bending strength.

The investigated composite material on the base of Al_2O_3 - ZrO_2, sintered at 1680^0C has better compressive strength indices compared to the ceramic material sintered at 1630^0C (*Fig.5*). Similar trend is observed while determining the bending strength (*Fig.6*) but the corresponding values are lower.
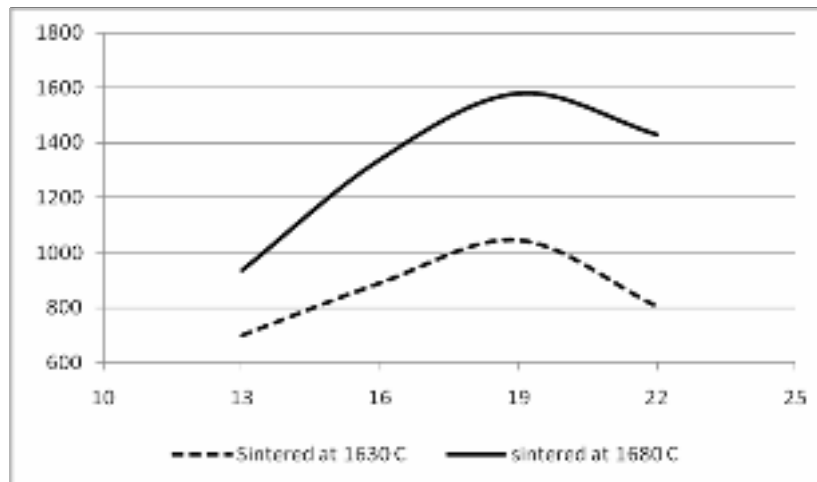
Fig.5. *Compressive strength (MPa) of the composite material sintered at 1630^0C and 1680^0C depending on the ZrO_2 (wt. %).*
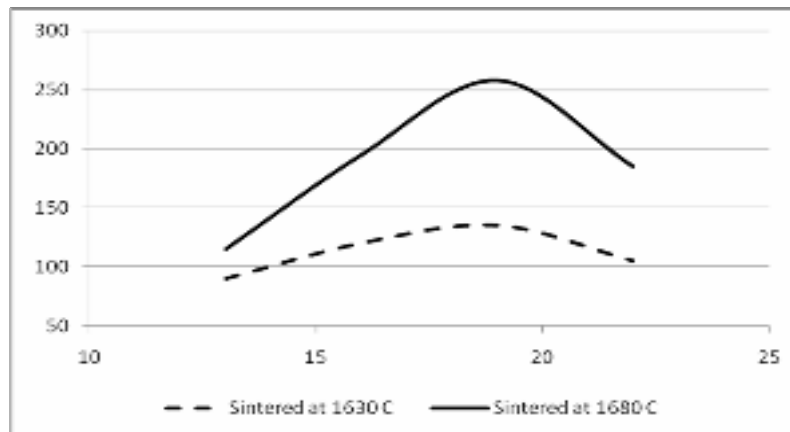
Fig.6. *Bending strength (MPa) of the composite material sintered at 1630^0C depending on the ZrO_2 (wt. %).*

Along with the sintering temperature and the additives, the physical and the mechanical properties are influenced strongly also by the content of the ZrO_2 added. The ZrO_2 is found in three polymorph forms: m-monoclinic, t-tetragonal and c-cubic. Depending on the type and quantity of the additives and the sintering temperature, ZrO_2 can be partially or totally stabilized in one or several modification forms.

The most interesting is the transition from monoclinic to tetragonal structure and vice versa in the temperature range $1000^0C – 1200^0C$. These phase transitions exhibit volume changes.

To avoid this shrinkage and expansion, leading to destruction of the product, partial stabilization of the ZrO_2 is made. We use additives such as Y_2O_3 CaO for this purpose and TiO_2 - to lower the sintering temperature and to compact the structure.

The high mechanical strength of the samples is a result of the tetragonal ZrO_2 located on the boundaries of the Al_2O_3 grains. It can be transformed from tetragonal into monoclinic form when external load is applied which contributes to the strength increase [11]. Based on the carried out experiments and analysis of the results obtained it is found, that the composite material of the Al_2O_3 - ZrO_2 system, containing partially stabilized ZrO_2 in the range 17 – 20 wt. % and modifying additives CaO and TiO_2, possesses the highest mechanical properties – compressive strength 1600 MPa and bending strength 260 MPa.

The Rockwell micro hardness measurements were performed on the same ceramic material sintered at temperature 1680^0C showing values in the range of 85 – 90 HRA, This ceramic composite is suitable for production of different construction components

enduring high mechanical loads and possessing high wear resistance.

4. Conclusions

Bio-inert ceramics are different materials used in the manufacture of orthopedic and dental implants for humans. These are: stainless steel, biocompatible, pure titanium and titanium alloys, cobalt alloys, polymer materials, inert bioceramic (Al_2O_3, ZrO_2), glassy carbon.

All of them have different advantages and disadvantages, but they have one common quality - they meet the standards for the materials used for making implants in human body (ISO 5832-1).

Developed by us TiO_2 - Nb_2O_5 composite materials have good layers of vitreous carbon and an extremely strong connection to the basic ceramic material.

Acknowledgements

References

[1]. **Tamaraiselvi T. V. and S. Rajeswari,** *Biological Evaluation of Bioceramic Materials – A Rewiev*, Trends Biomater. Artif. Organs, vol. 18 (10, PP. 9-17 (2004)

[2]. **George A. Graves, Jr.Dale E. McCullum, Steven M. Goodrich,** *Controlled pore size ceramics particularly for orthopaedic and dental applications*, US Patent 473741, Issued on April 12, 1988.

[3]. **Marti A**., *Inert bioceramics (Al$_2$O$_3$, ZrO$_2$) for medical application*, Injury, Int. J. Care Injured, vol. 31 (2000), S-D33-36.

[4]. **Eschbach L.**, *Nonresorbable polymers in bone surgery*, Injury, Int. J. Care Injured, vol. 31 (2000), S-D22-27.

[5] **Teodosiev D., L. Anestiev, J. Georgiev, N. Petrov, P. Tzvetkov and H. Nikolova,** *GLASS- CARBON BIOACTIVE COATINGS ON A TiO$_2$- Nb$_2$O$_5$ SUBSTRATE,* in print Proceedings of ARTCAST ' 2010, Galati , Romania

[6].*www.nanoscan.info.*

[7]. **Taffner Ul., C. Veronika**, **U. Schafer, M. J. Hoffmann**, *Preparation and Microstructural Analysis of High-Performance Ceramics,* ASM Handbook Volume 9: Metallography and Microstructures, 2004.

[8]. **Akimov G.Y., I.J.Prohorov,** Ogneuporiy, 1995, №2, 12-19 (in Russian)

[9]. **Kladnig W. and G.Gritzner**, J.Mater.Sci.Letters, v.6, 1987, 1235

[10]. **Buchvarov S., Ceramic** Technology, Sofia, 2003, 295 (in Bulgarian)

[11]. **Gogotci J.G., O.N.Grigoriev, N.A.Orlovskaya**, Ogneuporiy, 1991, №6, 2-5 (in Russian).

MATERIALS FOR TOTAL HIP JOINT PROSTHESES: BIAXIAL FLEXURAL STRENGTH OF TWO CERAMIC SYSTEMS

**Bojana TABAKOVA, Ivanka KALIMANOVA, Ina YANKOVA,
Hristiana NIKOLOVA**

Technical University of Sofia, Bulgaria
email: tabakova@tu-sofia.bg

ABSTRACT

Total hip joint replacement is one of the most successful orthopaedic surgeries in the last decade. Essential part of total hip joint prostheses is the mobile joint "hemispherical head - hemispherical cup". Functional properties and durability of the implanted prosthesis in the human body depend crucially on the mechanical and tribological properties and characteristics of materials of articulated parts.

Development and improvement of implant technology are inextricably linked with the development of new materials and, in particular, new ceramic materials with improved mechanical characteristics. This in turn requires improving methods of preliminary testing and evaluation of these characteristics.

In the paper materials for hip prostheses and methods for evaluation of their mechanical characteristics are briefly reviewed. The results of preliminary studies on some characteristics of reinforced titanium ceramics are presented.

KEYWORDS: bioceramics, flexural strength

1. Introduction

Along with high biocompatibility and durability of materials used for hip replacement are their mechanical properties.

There are a number of standardized procedures for determination of suitability of different materials.

For making different types of prostheses are used as metal (steel and titanium) alloys and various types of ceramics.

Two types of ceramic materials are used in practice - type A and type B. Type A ceramic materials for implants are subjected to high loads (bearing surfaces of joint implants), and type B materials are intended for use in implants with small loads (implants for middle ear).

Fundamental mechanical tests for ceramic materials for arthroplasty under ISO 6474:1994 (E) relating to the definition of average biaxial flexure load and wear resistance of the material, such as durability of the material are examined in cases where there is articulation of ceramics on ceramics.

2. Biaxial flexure testing

When examining the biaxial flexure load [1], a disk made of research material is placed between two coaxial rings of different diameters.

Gradually increasing compressive load is applied and its value at fracture of the specimen is registered. The Flexural Strength is calculated based on the results of the recorded fracture load (F).

The specimen, loading and supporting are shown schematically in Fig. 1 and Fig. 2a, Fig. 2b.
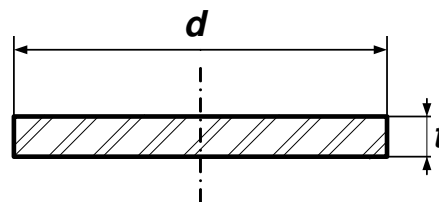
Fig.1. *Shape and dimensions of the specimen*

Principle scheme of measuring the strength of biaxial flexure is presented in Fig.3.

Between the supporting ring (2) and the specimen (3), a rubber pad (8) is placed to exclude the influence of shape deviations of the contact surfaces of the specimen and the rings. The loading ring (4) transmits the load to the specimen through a thin paper pad (7). For A uniform distribution of the load on the specimen, the load given by the loading device of the machine for testing tension/compression load (6) is transmitted through the metal sphere (5) to the loading ring (4)

a)

b)
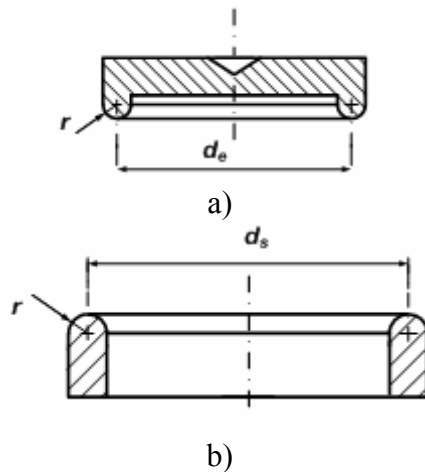
Fig.2. *Loading (a) and supporting (b) rings.*

The fracture load F of the specimen is registered. The flexural strength is given by:

$$\sigma = \frac{3F}{2\pi t^2}\left[(1+\nu)\ln\left(\frac{d_s}{d_e}\right)+(1-\nu)\left(\frac{d_s^2-d_e^2}{2d^2}\right)\right] \quad (1)$$

Where:
t – mean thickness, determined by 3 measurements of the specimen, mm;
d_s – average contact diameter of the supporting ring, mm;
d_e - average contact diameter of the loading ring, mm;
d - average diameter of the specimen, mm;
ν – Poisson's ratio was taken as 0.25 for all ceramics according to the recommendation in the standard.

The specimens are loaded in a universal testing machine INZTRON 1195. The loads applied to the surface of the specimen via loading ring at a rate of 540N/s.
The diameters of the contact circles of the supporting and loading rings are d_e = 12.01, mm and ds=30,14, mm, radius of the curvature of the contact surface with the specimen is r = 2.01 mm. Rubber pad placed between the specimen and the supporting ring has a 0.6mm thickness and

scleroscope hardness 62. The contact surfaces of the rings are hardened to 42 HRC.
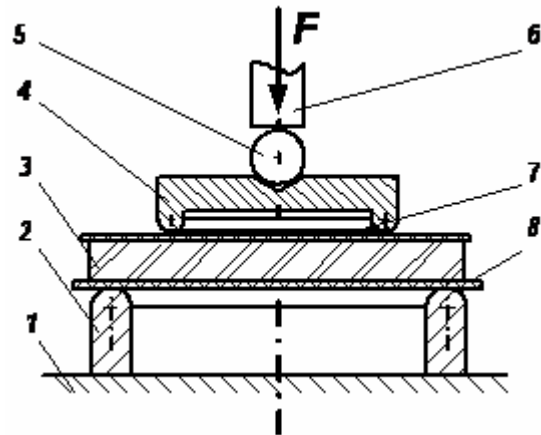
Fig.3. *Loading Scheme*
1–base; 2–supporting ring; 3–specimen;
4–loading ring; 5–contact sphere;
6-loading element; 7–paper pad;
8–rubber plate.

The diameters of the contact circles of the supporting and loading rings are d_e = 12.01 mm and d_s = 30.14 mm, radius of the curvature of the contact surface with the specimen is r = 2.01 mm. Rubber pad placed between the specimen and the supporting ring has a 0.6 mm thickness and scleroscope hardness 62. The contact surfaces of the rings are hardened to 42 HRC.

3. Materials and results

Materials used in the paper are aluminium and reinforced titanium ceramics. The test specimens [3] are obtained by the same technology used for making hip-joints femoral heads.

Aluminium ceramic
Ten pieces of "MARTOXID" ceramic (99.5% Al_2O_3 and 0.3% MgO) [2] MartinSWERK, used for manufacturing hip-joint prosthesis, were subjected to flexural strength test.
The dimensions of the specimens – diameter (d_m) and thickness (t_m), are given in Table 1. In the same table are given values of the fracture load F and defined according to formula flexural strength.

Reinforced titanium ceramic
The ceramic specimens tested were prepared by mixing TiO_2 and Nb_2O_5 powders in proportions ensuring concentration of 8wt.%. Nb_2O_5 in the final product. The preparation of the samples is described in details in [Teodosiev and all Artcast Galati] [4].
The prepared specimens were sintered at temperature of 1450°C (8 specimens) and 1520° (8

specimens) according to a predetermined temperature regime. The dimensions of the specimens - diameter (d_m) and thickness (t_m), are given in Tables 2 and 3 for type 1 and 2. In the same tables are given values of the fracture load (F) and flexural strength.

The tested specimens after fracture are shown in Fig. 4, 5 and 6.

Table.1. *Specimens dimensions and test results for "MARTOXID" ceramic*

Specimen №	Diameter	Thickness	Load at rapture		Biaxial flexure strength at rapture
	d_m, mm	t_m, mm	Load F, kg	Load F, N	σ, MPa
1	36.00	2.28	215	2109.2	265.6431
2	35.83	2.126	185	1814.9	263.2938
3	36.13	2.168	200	1962.0	272.9844
4	36.23	2.144	195	1913.0	271.9115
5	36.30	2.086	180	1765.8	264.9839
6	36.27	2.17	195	1913.0	265.3413
7	35.77	2.128	185	1814.9	262.9425
8	35.97	2.152	195	1913.0	270.5183
9	36.27	2.168	190	1863.9	259.0150
10	36.03	2.13	180	1765.8	254.7572
			$\overline{\sigma}$, MPa		**265.1391**
			s, MPa		**5.678312**
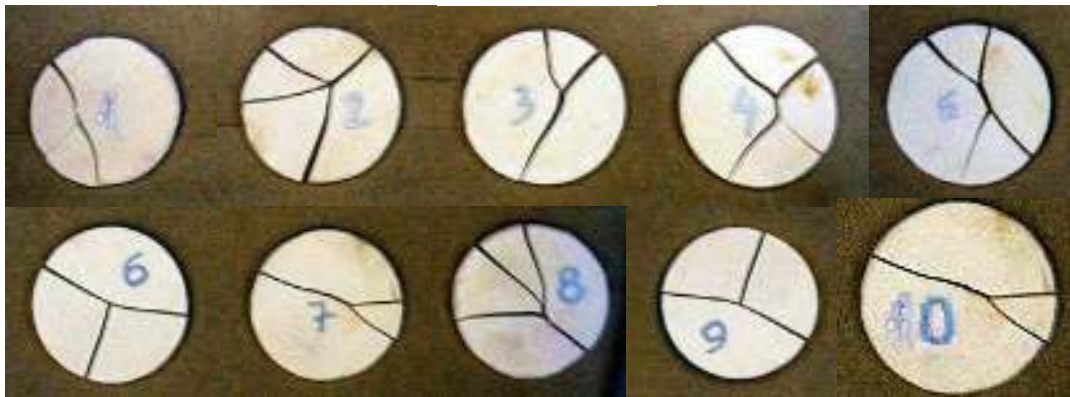
Fig.4. *Specimens from "MARTOXID" ceramic after fracture*

Table.2 *Specimens dimensions and test results for reinforce titanium ceramic – type 1*

Specimen №	Diameter	Thickness	Load at rapture	Biaxial flexure strength at rapture
	d_m, mm	t_m, mm	Load F, N	σ, MPa
1 -1	34.25	1.976	533	90.90
1 -2	34.08	2.042	494	79.00
1 -3	34.24	1.950	486	85.10
1 -4	34.15	2.160	750	107.2
1 -5	34.30	2.080	673	103.5
1 -6	34.13	2.120	984	145.9
1 -7	34.30	2.120	751	111.2
1 -8	34.20	2.124	733	108.2
			$\overline{\sigma}$, MPa	103.87
			s, MPa	19.33

Fig.5. *Specimens from reinforced titanium ceramic – type 1 after fracture.*

Table.3 *Specimens dimensions and test results for reinforce titanium ceramic – type 2*

Specimen №	Diameter	Thickness	Load at rapture	Biaxial flexure strength at rapture
	d_m, mm	t_m, mm	Load F, N	σ, MPa
2-1	34.32	2.244	538	71.1
2-2	34.8	2.215	919	124.0
2-3	34.25	1.980	458	77.8
2-4	34.3	2.080	720	110.7
2-5	34.23	2.183	901	126.0
2-6	34.16	2.081	640	98.5
2-7	34.16	2.124	556	82.1
2-8	34.45	2.213	720	97.7
			$\overline{\sigma}$, MPa	98.48
			s, MPa	19.37

Fig.6. *Specimens from reinforced titanium ceramic – type 2 after fracture.*

Conclusions

Studied samples of ceramics "MARTOXID", MartinSWERK, showed that the average flexural strength at biaxial flexure testing is $\bar{\sigma}$ =265.1 MPa. According to the requirements of the standard the minimum flexural strength is $\bar{\sigma}$ min= 50MPa.

Therefore the tested samples meet the requirements of the regulations for type A and ceramics can be used in a production to implants subjected to large loads.

The average flexural strength of titanium ceramic samples does not meet the requirements. For further investigation of these ceramics, their manufacturing technology must be improved so they can meet the requirements for hip-joint prosthesis.

Acknowledgements

References

[1]. ISO 6474:1994 (E) Implants for surgery - Ceramic materials based on high purity alumina

[2]. BDS EN ISO 21535:2007 Non-active surgical implants – Joint replacement implants

[3]. BDS EN ISO 21534:2007 Non-active surgical implants – Joint replacement implants – Particular requirements

[4]. Teodosiev D., L. Anestiev, J. Georgiev, N. Petrov, P. Tzvetkov and H. Nikolova - *GLASS- CARBON BIOACTIVE COATINGS ON A TiO_2- Nb_2O_5 SUBSTRATE,* in print Proceedings of ARTCAST' 2010, Galati, Romania

RESEARCH ON ABRASIVE WEAR BEHAVIOR OF LASER CLADDING LAYERS OF HIGH - SPEED STEEL POWDER TYPE HS6-5-2 - M2

Simona BOICIUC, Elena DRUGESCU

"Dunărea de Jos" University, Galaţi
email: simonaboiciuc@yahoo.com

ABSTRACT

The paper presents the wear behaviour on a rotating disk which carried abrasive paper of laser cladding layers with high-speed steel powder type HS6-5-2 - M2 compared to steel samples of the same quality but heat treated in volume. To see how temperature affects the wear behaviour by abrasion of the laser cladding alloy and the classically hardened steel, samples have been heated to 450 ℃, 550 ℃, 650 ℃ and 700 ℃ during a four hour exposure, after which they were subjected to testing. It was monitored the hardness and wear mass variation with temperature and the variation of micro-hardness in the laser cladding layer. In order to point out the microstructural aspects of the samples metallographic analyses were performed.

KEYWORDS: laser cladding, high-speed steel, tool, powder, injection

1. Introduction

Laser cladding is one of the laser surface treatments. It was defined like a process used to melt, on a sub-layer, with a laser beam, a material with different metallurgical properties. With this technique particles of a second material are deposited and melted onto the substrate in order to form a dense layer on top of the substrate. The resulting laser treated surfaces have the advantage of being dense, homogeneous, and have a superior bonding across the surface. In order to keep the genuine properties of the cladded material, a very thin layer of the sub-layer has to be melting, in order to get a minimum dilution (0.5 – 3%) of metallurgical bond of addition material and sub-layer material [1, 2]. Several methods can be applied.

The clad material can be pre – placed and then melted together with the underlying substrate by the laser. Another method is to blow the clad material on the surface while blowing a shield gas protecting the laser optics from sputtering material.

Laser cladding can be used to good effect in processes which require a high productivity combined with flexibility without compromising on quality.

The paper presents the wear behaviour on rotating disk with abrasive paper of laser cladding layers with high-speed steel powder type HS6-5-2 - M2 compared with steel samples of the same quality but heat treated in volume.

2. Experimental conditions

For deposition use was made of powder of high-speed steel type HS6-5-2 - M2, SR EN ISO 4957/2002 (Rp 5, STAS 7382/1988) having the following chemical composition 0.82% C, 4.7% Mo, 6, 4% W, 0.3% Mn, 4.1% Cr, 0.32% Si and 2.02% V, and Fe [3, 4]. By sieving the grain fractions were separated in the range 80-90 μm to be used as added material. The powder had a spherical shape, which provided a smooth flow of the material additive through the injection system. Before placing the added material in the injection tank, the powder was dried at a temperature of 110°C for 15 minutes [3, 4].

The basic material used in the experimental research is steel 1C45, SR EN 10083-1:1994. Laboratory experiments were conducted on a CO_2 continuous wave system, type 1400W Laser GT (Romania), with working mass in x-y-z coordinates and computer programming of the working regime, provided with a powder injection system on the melted surface by means of laser, existing in SC UZINSIDER ENGINEERING Galaţi.

For the laser cladding it was used a laser beam of 1.8 mm diameter on the treated surface, at 1100 W power, scanning speed 5mm/s, by means of which partly overlapping parallel strips were deposited with a transverse step advance of 2 mm. The flow rate of the material added was 134mg/s. Final thickness of

the deposited layer was 1.5 mm resulting in 5 overlapping layers.

The samples of steel Rp5 were quenching at 1220°C, with a subsequent triple annealing for one hour at 560°C.

To see how temperature affects the wear behaviour by abrasion of the laser deposited alloy and the classically hardened steel, samples have been heated to 450°C, 550°C, 650°C and 750°C during four hour exposure, after which were subjected to testing. The abrasive wear behavior of laser deposited layers with the nickel base alloy has been studied according to STAS 9639-81.

The method uses a connection of peg/disk friction of class IV-1. The method consists in pressing sequentially, under identical conditions, two samples of dimensions 6.2x6.2 mm, one of the material examined deposited by laser and the other from a material chosen for comparison purpose – improved high - speed steel Rp5 classical quenching on a rotating disk covered with grinding paper of 120 grains. A mechanism for radial displacement of the tube with 0.5mm/r provides a spiral movement on the surface of the rotating disk.

A device for implementing a load of 8.387 N ensured perpendicular pressing of the sample on the grinding paper at a pressure of 0.215N/mm^2. At disk speed of 25rpm, a number of 131 rotations have provided a length path of 82m.

It was monitored the hardness and wear mass variation with temperature and the variation of micro-hardness profile plotting $HV_{0,1}$ (load 0,98N) in the cross-section of the laser cladding layer.

3. Experimental results and discussions

The samples where laser deposit was performed with high – speed steel powder type M2, the classically hardened samples and the support were subjected to wear testing on a rotating disc with abrasive paper. The results are presented in Table 1, which is the average of three determinations.

It may be noted that the laser cladding alloy is more resistant to abrasive wear than steel samples classically hardened, and especially to support. To see how temperature affects the wear behaviour by abrasion of the laser cladding alloy (code A, B, C, D) and the classically hardened steel (code 1, 2, 3, 4), samples were heated to 450°C, 550°C, 650°C, 700°C and exposed for four hours, after which they were tested.

Table 1. Abrasive wear behaviour of the support, the deposit of high – speed powder, and the classically hardened high – speed steel unaffected by temperature

Material	Initial mass	Final mass	Mass wear	n
	[g]			[rotations]
1C45	2.9150	2.7270	0.1870	131
Laser cladding M2	3.1638	3.0818	0.082	131
High – speed steel classically quenching	2.6625	2.5608	0.1017	131

The results after heating are given in Table 2 and those obtained after wear tests are given in Table 3. Table 2 shows the samples code, the heat conditions and the hardness obtained on the surface of the samples. The variation of hardness vs. heating temperature is shown in Fig. 1.

Table 2. The heat conditions and hardness of the samples

Sample code	Heating temperature	Exposure time	Initial hardness HV_5	Final hardness HV_5
	[°C]	[h]	[MPa]	
A	450	4		9860
B	550	4		9560
C	650	4	10490	7810
D	700	4		5280
1	450	4		8910
2	550	4		8570
3	650	4	8910	7010
4	700	4		4940
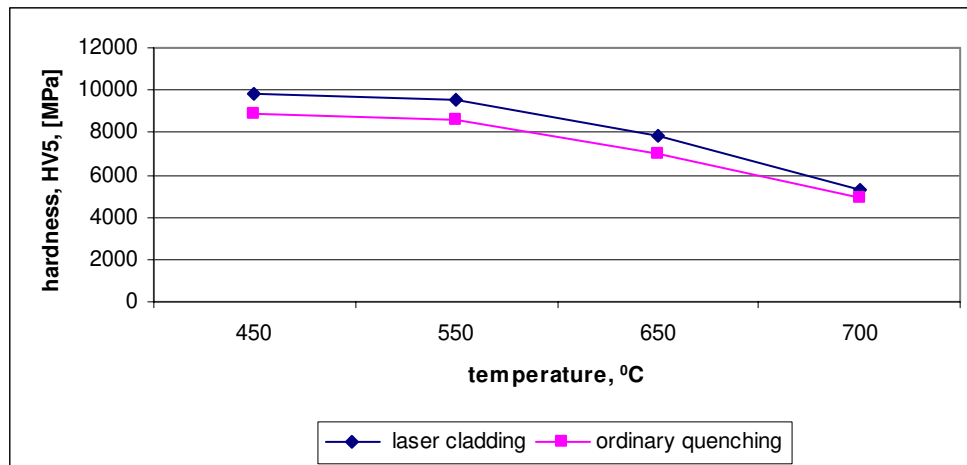
Fig. 1. *Variation of hardness with heating temperature for
laser cladding samples and quenching samples.*

Analyzing Table 2 and Figure1, it can be noticed that, as the heating temperature increases there is a decrease in hardness for both in laser cladding layers and classically treatment samples. However the hardness of the laser layer is maintained at higher values as compared with the classical treatment of steel Rp5. Thus the minimum hardness of 58HRC is reached by the laser cladding at 690°C, while the classically quenching steel at 650°C. This may be correlated with the fact that with laser cladding, the ultra rapid cooling speed causes hardening since the liquid phase with the formation of more alloyed austenite by dissolution of the secondary and part of the primary carbides, chemically non homogenous, finer grains and increased amount of structural defects. High cooling speed guaranteed martensite transformation that inherits the austenitic characteristics, together with an increased amount of residual austenite. Recrystallization at overlaps

favored dispersed precipitation of the carbides and diminished the amount of residual austenite.

Upon heating within the range of 450-700 °C, the high-alloyed martensite featured higher thermal stability than the martensite obtained by the classical volume treatment and implicitly higher hardness at the same heating temperature.

To highlight the microstructural aspects of the heated samples, metallographic analyses were performed at 500x magnifying, both for those with laser cladding and those obtained classically, the metallographic attack being made with nital 2%. They are given in Fig. 2 and 3.

From Fig.2 it can be seen a dendritic structure specific to the laser cladding with numerous carbides.

From Fig.3 it can be seen that as the heating temperature increases coalescence of carbides takes place along with lower degree of dispersion, which leads to lower hardness.
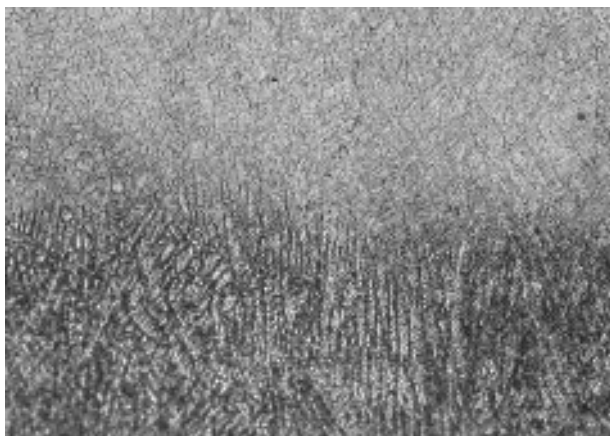
A.a
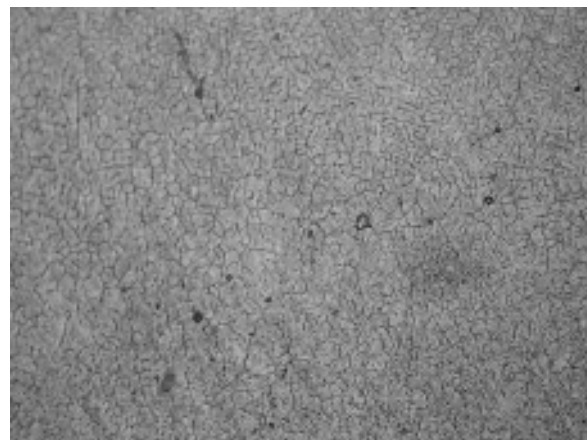
A.b
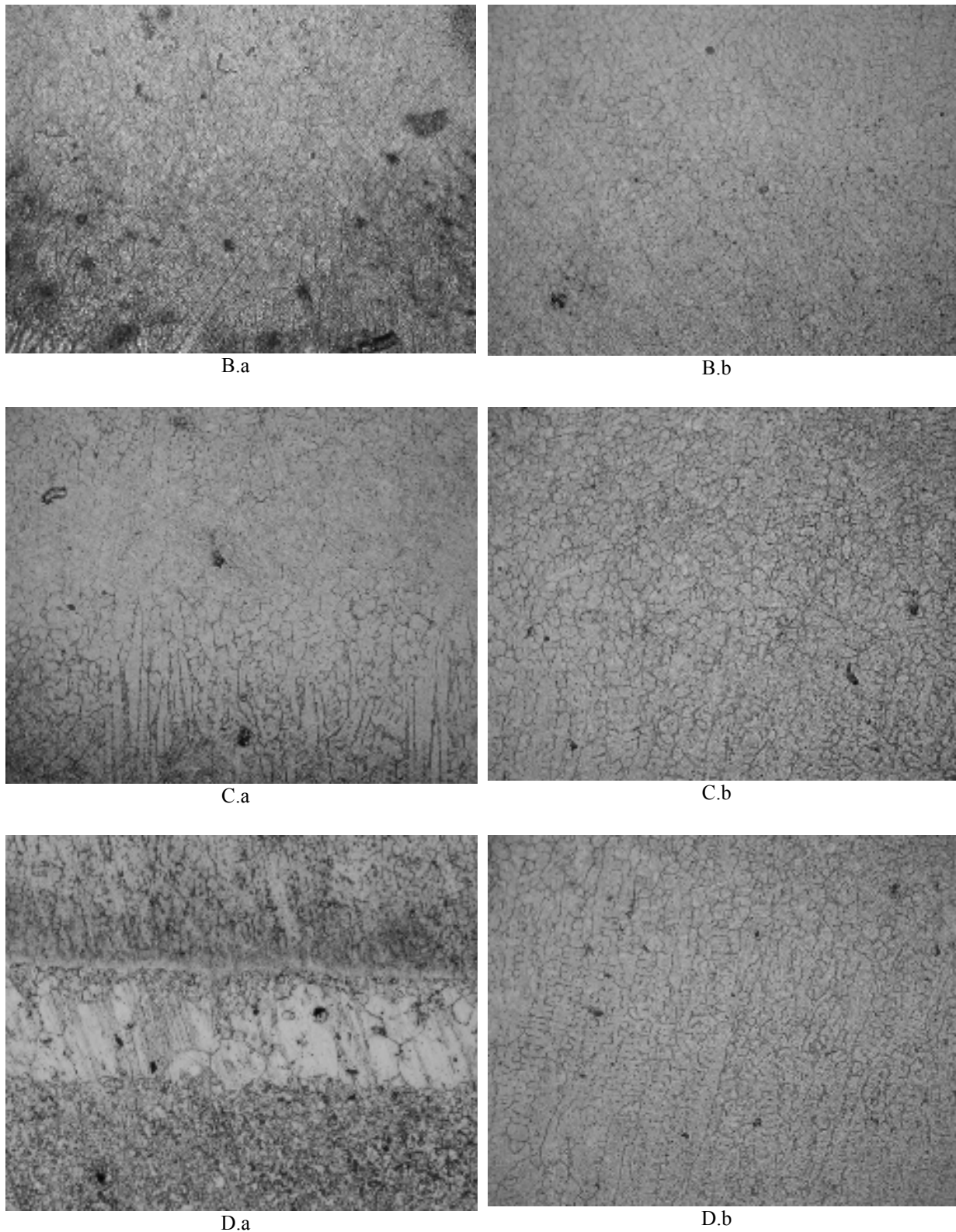
Fig.2. *Microstructures of the laser cladding layers with powder of high-speed steel heated at different temperatures for samples code A - 450 ℃, B - 550 ℃, C - 650 ℃, D - 700 ℃: a)- layer base, b- layer surface (x500). Nital attack 2%.*
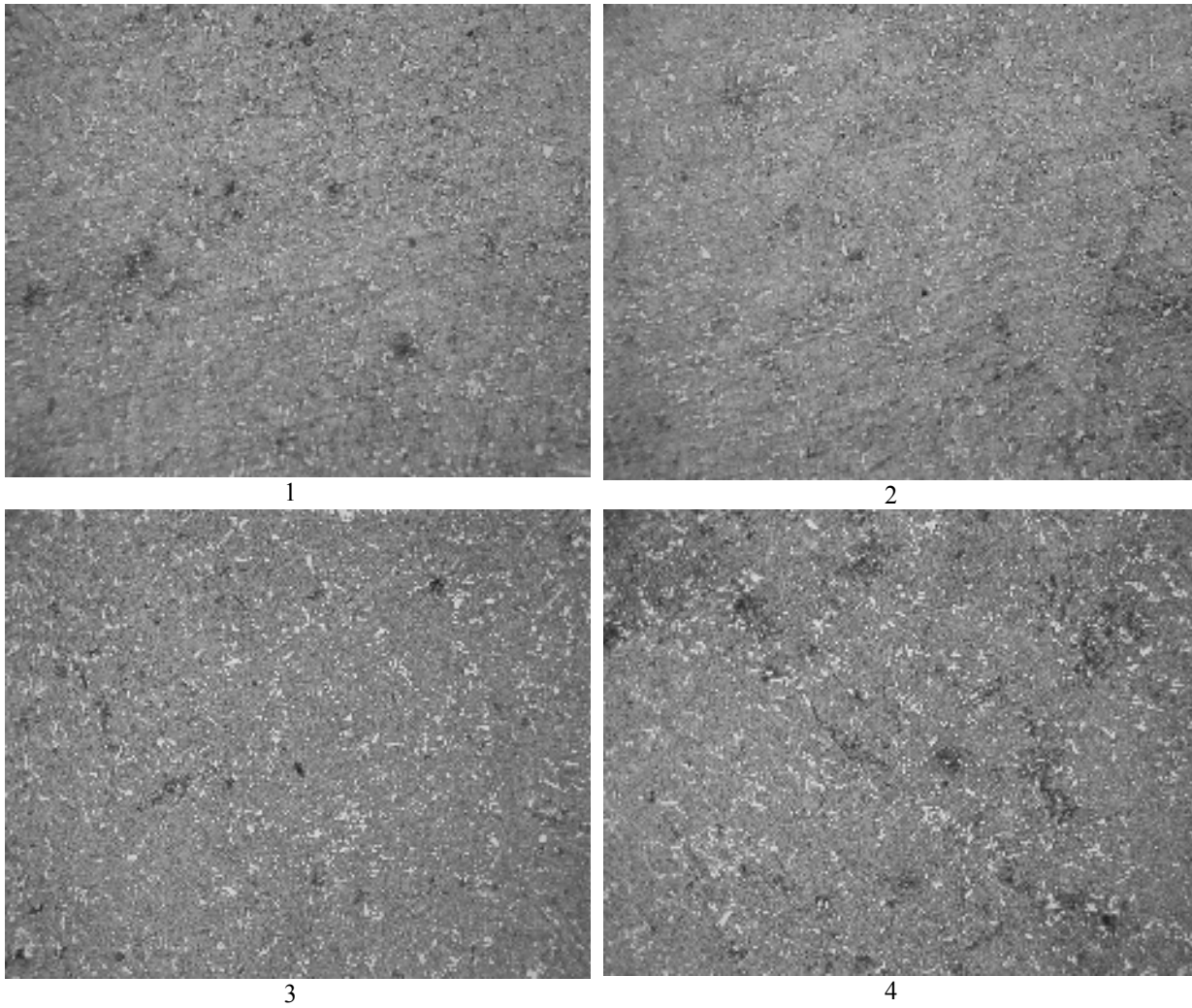
Fig.3. *Microstructures of high-speed steel Rp5 classically heated at different temperatures for samples code 1 - 450 ℃, 2 - 550 ℃, 3 - 650 ℃, 4 - 700 ℃ (x500). Nital attack 2%.*
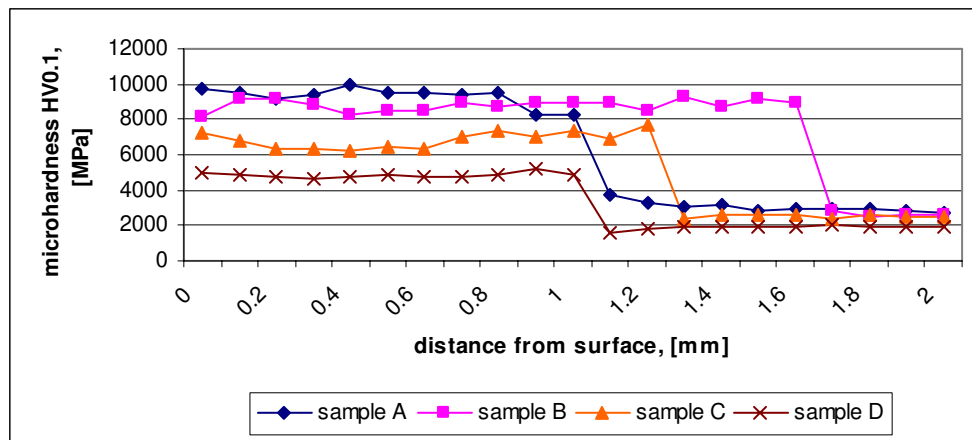
Fig.4. *Variation of microhardness of the cladding layer after heating for samples code A – 450 ℃, code B – 550 ℃, code C – 650 ℃, code D – 700 ℃.*

According to qualitative phase analysis [3], the microstructure of the deposited layers heated at different temperatures contain martensite, residual austenite and eutectic colonies of carbides interdendritically spaced and at the grain limit, the basic hardening phase being Cr_7C_3. Variation of microhardness of the laser layer with high - speed steel type M2 obtained after heating the samples code

A, B, C, D at 450°C, 550°C, 650°C, 700°C with a four hour exposure time.

Results are given in Fig.4. Table 3 presents results from wear tests (mass wear, mass wear/length of path covered) in rotating disk with abrasive paper both laser cladding samples and those classically hardened in volume.

Tabel 3. *The samples abrasive wear behaviour after heating at several temperatures*

Sample cod	Heating temperature	Keeping time	Initial mass	Final mass	Mass wear	U/L
	[°C]	[h]		[g]		[g/m]
A	450		2.9865	2.9030	0.0835	0.00104
B	550		2.9781	2.8929	0.0852	0.00107
C	650		3.1055	2.9881	0.1174	0.00136
D	700	4	3.1118	2.9478	0.164	0.00202
1	450		2.6625	2.5599	0.1026	0.00123
2	550		2.5827	2.4792	0.1035	0.00126
3	650		2.7234	2.5982	0.1252	0.001502
4	700		2.6004	2.4306	0.1698	0.002093

It is noted that heating at different temperatures affects the wear behaviour of the deposit.

Thus as the temperature increases the wear resistance decreases at temperatures higher than 650°C, which is due to coalescence carbides and decrease in their dispersion. Fig. 5 and Fig. 6 show the variation of mass wear and the ratio of wear mass/length of path covered with the heating temperature for samples: code A, B, C, D and code 1, 2, 3, 4.
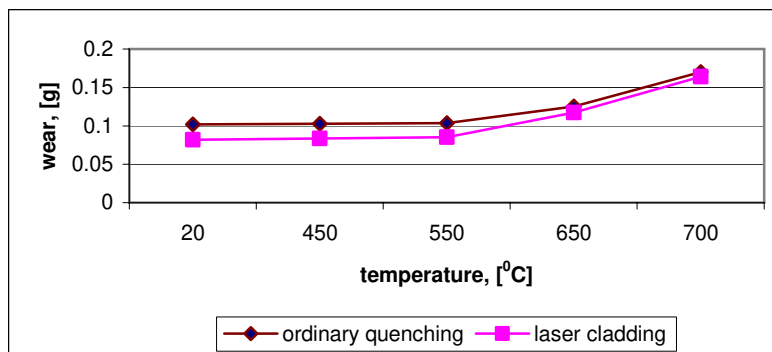
Fig.5. *The variation of mass wear with the heating temperature for samples:*
code A, B, C, D and code 1, 2, 3, 4.
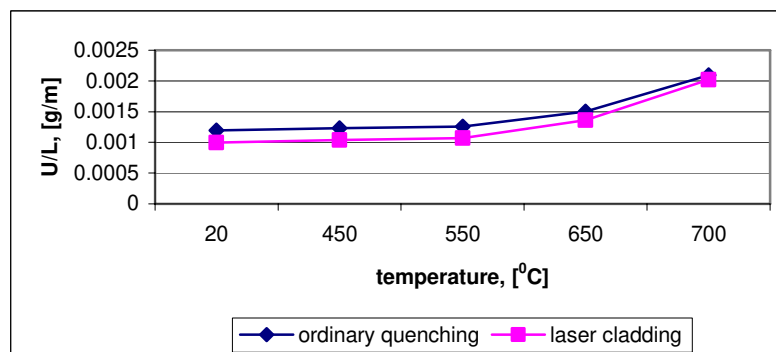
Fig.6. *The variation of the ratio of wear mass / length of path covered with the heating temperature*
for samples: code A, B, C, D and code 1, 2, 3, 4.

Analyzing the above figures it may be noted that the wear mass and wear ratio mass/length of the path covered increase with increasing temperature, more pronounced at values higher than 650°C, which is due to coalescence carbides and decrease in their dispersion.

4. Conclusions

As regards thermo-stability of the laser cladding with high - speed steel powder M2 and heat treated samples in volume it was found that as heating temperature increases there is a decrease in their hardness because of coalescence carbides and their decreased dispersion.

Abrasive wear behaviour of laser cladding layers of high - speed powder M2 showed a higher resistance compared to steel 1C45, and Rp5 classically hardened steel.

The ultra rapid cooling speed in laser cladding causes hardening since the liquid phase with the formation of more alloyed austenite by dissolution of the secondary and part of the primary carbides, chemically non homogenous, finer grains and increased amount of structural defects.

High cooling speed guaranteed martensite transformation that inherits the austenitic characteristics, together with an increased amount of residual austenite.

Recrystallization at overlaps favored dispersed precipitation of the carbides and diminished the amount of residual austenite.

With respect to abrasive wear resistance of the laser cladding layers, heated at different temperatures it can be observed that the mass wear and the ratio of mass wear/length of the road covered increase with higher temperature, even more at values higher than 650°C, which is due to coalescence carbides and their decreased dispersion.

Also the dilution zone is changed which is visible due to the decrease in the difference in hardness between the cladding layer and the substrate.

Reference

[1]. **M.F. Schneider** - *Laser cladding with powder*, Ph. D. Thesis University of Twente, Enschede, Olanda, 1998.

[2]. **H. Gedda** – *Laser surface cladding - a literature survey*, Lulea University of Technology, Division of Materials Processing, iulie 2000, Suedia.

[3]. **D.T. Levcovici, R. Boiciuc, S.M. Levcovici, C. Gheorhieş** – *Laser cladding of M2 steel on a steel substrate*, The International Thermal Spray Conference and Exposition (ITSC), may 15th – 17th, 2006, pp. 1333-1338 Seattle, USA (ISBN 0-87170-836-1).

[4]. 1. **D.T. Levcovici, S.M. Levcovici, I. Onea** – *Procedure of laser cladding of high speed steel*, Patent 121477 B1 din 30.04.2007.

COMPOSITE COATING IN COPPER MATRIX WITH MOLYBDENUM IN DISPERSION PHASE OBTAINED BY ELECTROCHEMICAL METHODS

**Olga MITOSERIU, Florentina POTECASU,
Stela CONSTANTINESCU, Lucica ORAC**

"Dunarea de Jos" University of Galati
email: lucia_orac@yahoo.com

ABSTRACT

The paper describes reviews referring to determination of working parameters of the development processes of composites in copper matrix, obtained by electrochemical deposition methods.

The molybdenum particles having particle sizes of 3μm, respective 7μm have been used as a complementary phase. The optimal conditions for codeposition were determined, the structure and chemical composition of the obtained coatings were presented and the coating characteristics were tested.

KEYWORD: electrochemical deposition, structure, coating

1. Introduction

The present study refers to the obtaining of composite coatings in the copper matrix by electrochemical co-deposition of molybdenum. The particles used were of 3μm and 7μm in size.

There is no data in the literature on composite coatings of copper and molybdenum in disperse phase.

The composite coatings obtained by including the dispersed-phase particles in the matrix material have a wide technological interest for many fields of applications. These materials have a wide range of new properties, in particular improved mechanical properties [1].

2. Results and experimental researches

An ELLY BUDAPESTA type electrolyser, a magnetic stirring machine and an electrolyte tank (receiver) were used in order to obtain the copper coatings.

It was used a solution volume of 250 ml, and the experiments took place at 20ºC.

Like in Cu electrodeposition with a view to determining the optimal electrodeposition parameters use was made of copper samples - base metal,

substances for the preparation of electrolytic solutions, molybdenum powder (size 3μm and 7 μm) solutions and substances for preparation of surfaces.

By electrodeposition composite materials were obtained with molybdenum disperse phase. Concentrations of molybdenum powder of 7μm and 3μm respectively were 20%, 40%, 60% in the electrolyte solution [2].

The coppering electrolyte used had the following chemical composition:

$$CuSO_4 \cdot 5H_2O : 200g/L; \ H_2SO_4 : 80 \ g/L.$$

Since the composite materials Cu-Mo are entirely new, the electrochemical deposition technology was established. In copper electrodeposition, certain parameters were kept: orientation of electrodes, distance between electrodes 2cm. A high purity cooper anode and cathode of cooper tape having an active area of 16 were used.

The cathode face that did not come in direct contact with the anode was insulated.

The presence of particles was highlighted by EDX tests. By electron microscopy in cross section and EDX spot analysis it was observed a homogeneous distribution of the additional phase (Mo 3 micrometres and 7 μm) in the copper matrix (Figures 1, 2).
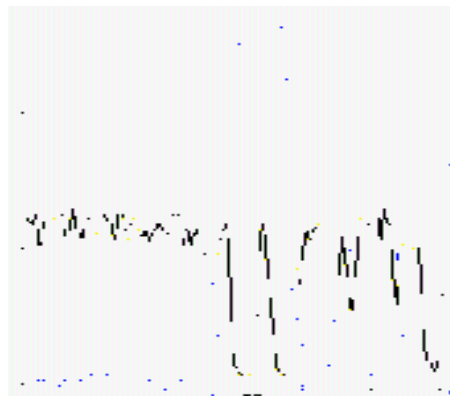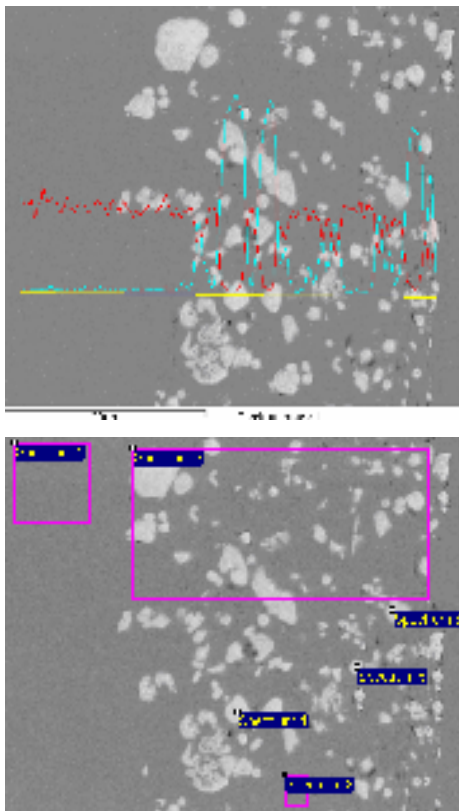
Processing option : All elements analysed (Normalised)			
All results in weight%			
Spectrum	O	Cu	Mo	Total
Spectrum 1		100		100
Spectrum 2		76.4	23.6	100
Spectrum 3		100		100
Spectrum 4	2.11	4.24	93.65	100
Spectrum 5	2.01	14.36	83.64	100
Spectrum 6	3.41	6.18	90.4	100

Fig. 1. *EDX analysis in cross- section and spot for Cu-Mo composite coatings obtained at 1.5 A/dm^2, 60min, 500rpm, 40g/L particles in electrolyte solution, particle size 3µm.*
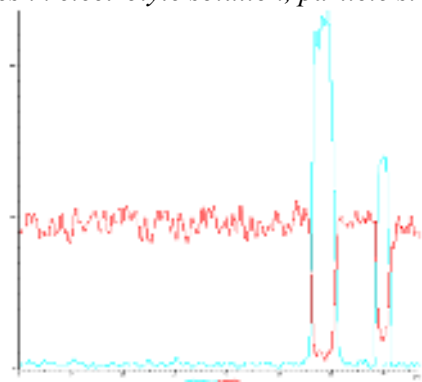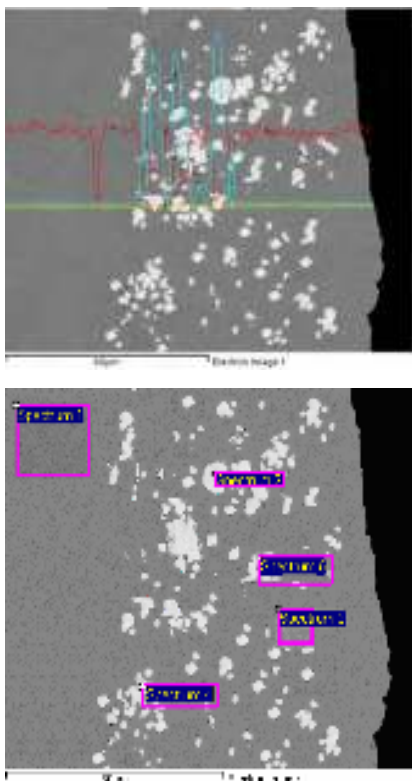
Processing option : All elements analysed (Normalised)			
All results in weight%			
Spectrum	O	Cu	Mo	Total
Spectrum 1		100		100
Spectrum 2		93.45	6.55	100
Spectrum 3		100		100
Spectrum 4	2.35	11.76	85.89	100
Spectrum 5	2.1	31.19	66.7	100

Fig. 2. *EDX analysis in cross section and spot for Cu-Mo composite coatings obtained at 2 A/dm^2, 60min, 500rpm, 40g/L particles in electrolyte solution, particle size 7 m.*

The concentration of particles in the composite layer increases with increasing current density up to a certain value (Imax) and then decreases [3]. Figure 3 illustrates the relationship of interdependence betwee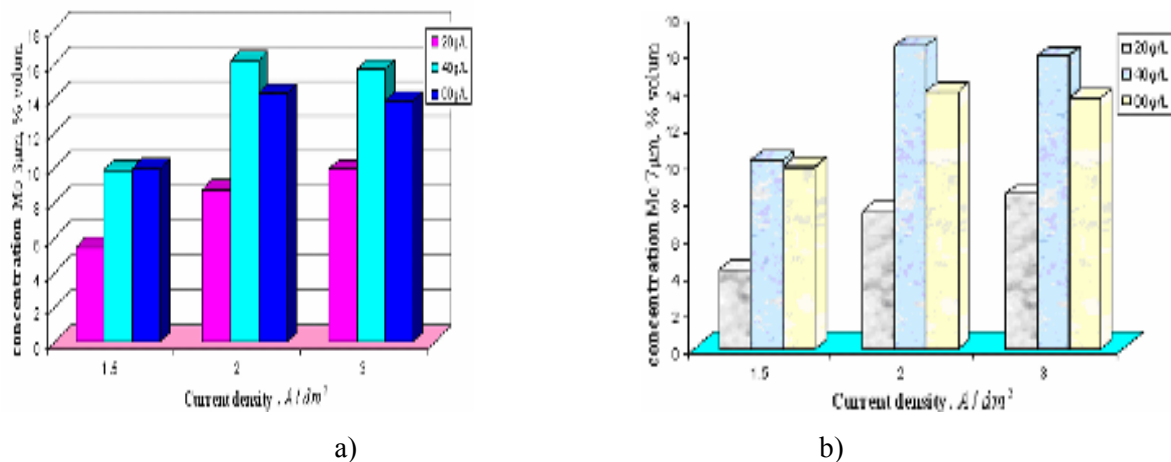n the concentration of Mo 3µm, 7 µm particles in the composite layer and current density for different amounts of particles contained in the electrolyte.

It is noted that the percentage of inclusion increases with increasing current density to a concentration of 20g/L, and the concentrations of 40, 60g/L particles in the electrolyte solution increases with increasing inclusion rate of current density and reaches a maximum at $i_{max} = 2\ A/dm^2$ then decreases

[4]. The highest degree of inclusion has been determined for Cu-Mo composite coating obtained at $2\ A/dm^2$, 180 min, 500rpm, 40g/L, and the minimum degree of inclusion of molybdenum particle, size of 3µm (size 7µm) in copper matrix was obtained at 1.5 A/dm^2, 30 min, 500rpm, 20g/L.

Analyzing the cross-section microstructures it is observed the uniform distribution of the molybdenum layer. For concentrations of 40g/L and 60g/L Mo agglomerations of particles of molybdenum can be observed [5].

a)

b)

Fig. 3. *Variariation of the percentage content of Mo particles in the composite deposit as a function of current at a concentration of 20g/L, 40g / L, 60g/L Mo in the electrolyte solution, 180min: a) Mo size 3µm, b) Mo size 7µm.*

The Cu-Mo composite coatings with a size of 3 µm and 7 µm appear very well distributed, they are compact, continuous with a finishing tendency of

crystals as compared with pure copper, leading to the formation of fine, compact and continuous deposits (Figures 4,5,6,7).

a)   b)   c)   d)
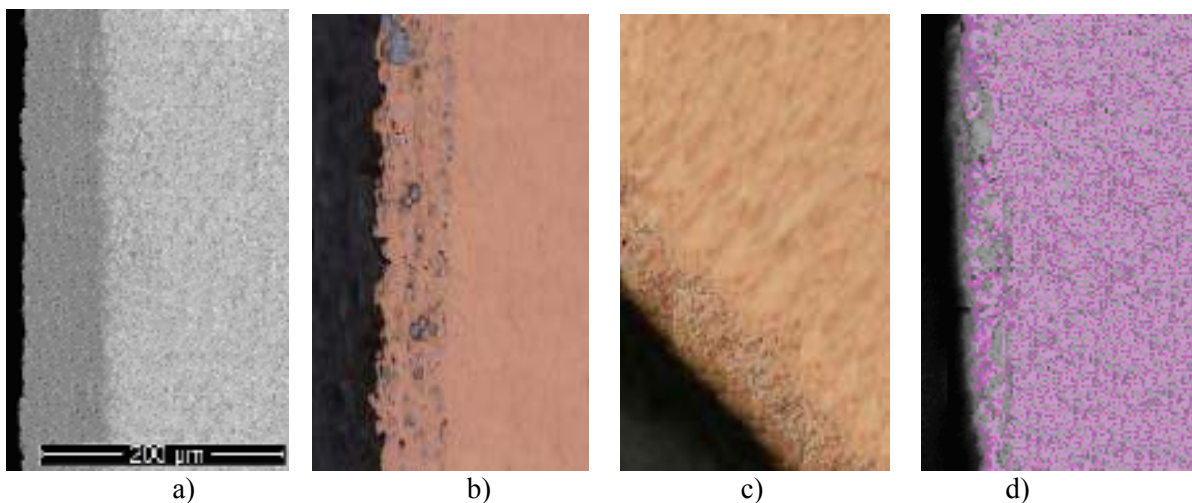
Fig. 4. *Cross-section microstructures for the Cu- Mo coatings with particle size 3µm , 180min, 500rpm, i= 2 A/dm^2: a) pure Cu, b)Cu- Mo, 20g/L; c)Cu-Mo 40g/L; d)Cu-Mo, 60g/L, magnifying x 500.*
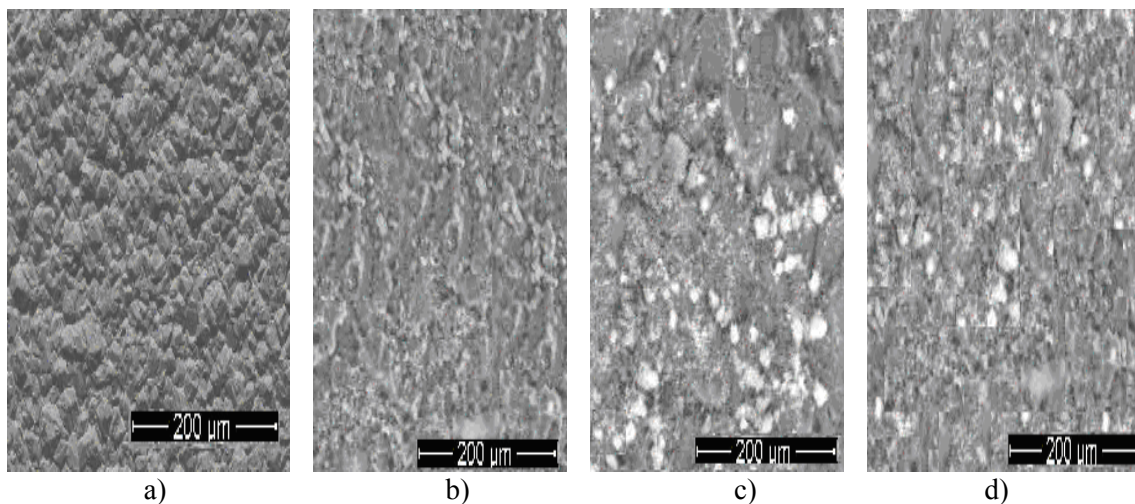
Fig. 5. *SEM surface microstructures for Cu- Mo coatings , particle size 3μm , 180min, 500rpm, i= 2 A / dm^2 : a) pure Cu , b)Cu- Mo, 20g/L; c)Cu-Mo 40g/L; d)Cu-Mo, 60g/L, magnifying x 500.*
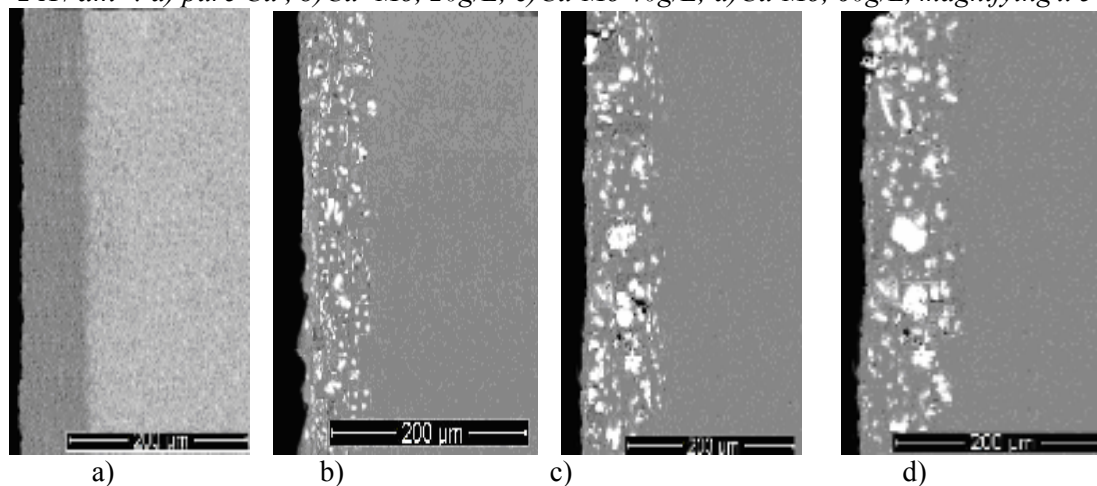
Fig. 6. *Figure 6. SEM surface microstructures for Cu- Mo coatings, particle size 7μm, 180min, 500rpm, i= 2 A / dm^2 : a) pure Cu , b)Cu- Mo, 20g/L; c)Cu-Mo 40g/L; d)Cu-Mo, 60g/L, magnifying x 500.*
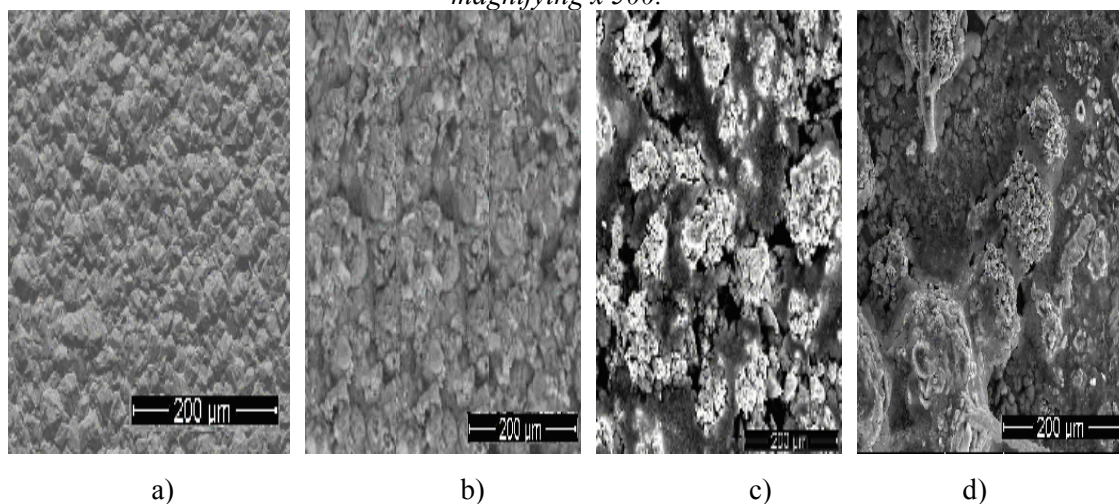
Fig. 7. *Cross-section microstructures for the Cu- Mo coatings with particle size 7μm, 180min, 500rpm, i= 2 A / dm^2 : a) pure Cu, b)Cu- Mo, 20g/L; c)Cu-Mo 40g/L; d)Cu-Mo, 60g/L, magnifying x 500.*

It is noted an increase in the inclusion of molybdenum, particle size of 3 micrometres and 7 μm, in the copper matrix with increased concentration in the electrolyte up to 40g/L and for a concentration of 60g/L, a decrease of particle inclusion. The presence of particles in the deposited layers will change both their structure and properties. Layer thickness values are given in Table 1. For the layer thickness metallographic examinations were made in the middle of the sample on portions of 10 mm. The sample was divided into 10 equal parts and each time three measurements were made [6].

As regards roughness of the coatings obtained by adding molybdenum particles in the electrolyte solution there are quite large variations in the level of roughness for composite coatings obtained under different conditions.

Table 1. *Thickness of Cu – Mo layer*

Current density, I A/dm^2	Conc. Fd. in electrolyte [%]	Thickness [μm]			
		30 [min]	60[min]	90[min]	180[min]
I=2 A/dm^2 (Cu-Mo 3μm)	M	9	25	36	50
	20g/L	9	13	19.5	37
	40g/L	9.5	14	34	45
	60g/L	11.5	15	20	30
I=2 A/dm^2 (Cu-Mo 7μm)	M	9	25	36	50
	20g/L	7	13	17	28
	40g/L	10	16	30	42
	60g/L	12	19	29	40

These values are lower compared to the roughness values determined for pure copper. The presence of molybdenum particles has catalytic role in the copper reduction reaction. The immediate effect of this phenomenon is the modification of the structure deposited by decreasing the size of crystals which implicitly leads to lower surface roughness.

It is noted that the average absolute roughness ranges from 2.9 to 1.6 μm for Cu-Mo 3 μm and 2.7 to 2μm for Cu-Mo 7 μm.

3. Conclusion

By electron microscopy in cross section and the EDX spot analysis it was observed the inclusion of the dispersed phase and homogeneous distribution of the additional phase (Mo 3 μm and 7 μm, respectively) in the copper matrix, when the electrochemical method is applied.

The degree of inclusion of molybdenum particle size of 3 μm and 7 μm in the copper matrix increases with increasing their concentration in the electrolyte up to 40g/L.

The presence of molybdenum particles has catalytic role in the copper reduction reaction.

References

[1]. O. Mitoseriu, S. C. Cocindau, F. Potecasu, L. Orac - *Composite coatings obtained through electrodeposition of Cadmium and short ceramic fibers*, Metalurgia International,

[2]. O. Mitoseriu, S. C. Cocindau, F. Potecasu, L. Orac - *Composite coatings obtained through zinc electrochemical codeposits and short ceramic fibers*, Metalurgia International, 19-26.

[3]. O. Mitoseriu, I. Rusu, S. C. Cocindau, F. Potecasu, L. Orac - *The method of obtaining zinc coating matrix composites and ceramic fibers dispersed phase*, Meridian engineering, Moldova, Ed. U.T.M, vol. 2/ 2009, p. 37-43.

[4]. O. Mitoseriu, S. Constantinescu, L. Orac - *Study and researches regarding binaring system with tiobis- β- naftol*, The Annals of "Dunarea de Jos" University of Galati, Fascicle IX Metallurgy and Material Science, Vol. Nr. 1 2007

[5]. O. Mitoseriu, S. Constantinescu, L. Orac - *Identification and measurement of copper from special alloys and waste waters,* Proceedings of the 4th Conference Black Sea Basin, Bulgaria, 2007, p.55-60

[6]. O. Mitoseriu, S. Constantinescu, L. Orac - *Electrochemical deposition method to obtain composites coatings with metal matrix,* Conferinta internationala TEHNOMUS, Universitatea „Stefan cel mare" Suceava, 2009, p. 479- 484.

THIN LAYERS OBTAINED BY ELECTRIC SPARK IN LIQUID MEDIUM

Ion HOPULELE, Carmen NEJNERU, Manuela Cristina PERJU, Mihai AXINTE

Technical University "Gheorghe Asachi" of Iasi, Romania

ABSTRACT

This paper is a study about the thin layers obtained by metallic deposition method in liquid medium. For this we studied the structure and composition of different deposition regimes, in different liquid mediums. Liquid medium is chosen depending on the purpose. Thus, use was made of protective environments that aim at achieving a more compact layer without many oxides, reactive environments whose components, due to sparkle reactions, combine with elements of basic material to obtain carbides and complex carbonitrides with good wear resistance properties.

KEY WORDS**:** thin layers, liquid mediums, vibrating electrode

1. Introduction

Electrical processing of metallic materials based on electrophysical and electrochemical phenomena includes a wide variety of technological fields. Because the application of electrical processes is not always an advantage, such devices can not replace the heating treatments, only in limited cases. These methods are defined on one side of the current state in science development, and secondly by the quality requirements in building machinery [4].

Electrotechnological metal processing methods can be divided into two main categories:

- processing methods which change shape or properties of the metal piece. These treatments do not alter the volume of materials (plastic deformation and heat treatment);

- processing methods which change the piece volume (cutting or deposition of material).

To achieve material processing operations are performed by electric spark in order to remove a part of the material (cutting, drilling, polishing, etc.) using direct polarity where the piece is the anode. For deposition the piece is the cathode (layers deposition).

The processes can take place in the air, protective gas environment or liquid medium. Comparing to other metal coating methods, deposition and metal surfaces alloying method by electric spark has some advantages [1]:

- It provides a layer with good adhesion to the base material;

- There is no need for special surface preparation;

- High melting point metals depositions can be made (Mo, W, Ti);

- Alloying elements may be supplemented in the discharge environment (nitrogen, carbon, boron);

- Quenching occurs from the liquid phase of metal deposition.

It follows that the electric spark deposition principle creates a layer with special properties according to used electrodes and discharge environment.

An important requirement of the method is the electric spark discharge energy in the space between the electrode and the piece. The process starts by approaching the electrode from the part. To a specified distance the space is broken by the electric spark, which continues until the electrode-part contact.

Due to electric spark energy, erosion craters appear on the electrode surface, caused by melting and evaporation. The material deposits on the work piece surface under the action of hydrodynamic pressure plasma jet. The process has a particular electrode vibration frequency and determined vibration amplitude. By electric spark deposition it alters its chemical composition and mechanical properties. Total depth for treated layer is 0,02 mm to 0,25 mm containing 20 to 30% of the cathode material and discharge environment [3].

Environmental influence between electrodes to the electric spark process is manifested in two ways. On the one hand, high temperatures in the discharge areas, the electrode gas ionization, and on the other,

the presence of vaporized and liquid phases contribute to increasing interaction between electrode material and medium elements therefore they change the physical and chemical properties of the layer. Electric spark process in mediums such as: hydrogen, argon, nitrogen or other protective environments allows us to obtain high quality layers. Magnetic fields and electrical discharge overlapping effects substantially alter the deposited layer features; ultrasonic oscillations have also a positive influence.

2. Obtaining electric spark deposition layers

Compared to other metallic coating achieving methods, electric spark metal deposition is based on using simple equipment and technologies. The installation contains a DC source and an electric spark discharge circuit (Fig. 1). Power supply has a voltage below 60 V and a current of $1 \div 20$ A depending on the working regime. The discharge circuit includes a variable resistance and a capacitor. The electrode is vibrated at a frequency of $50 \div 200$ Hz.
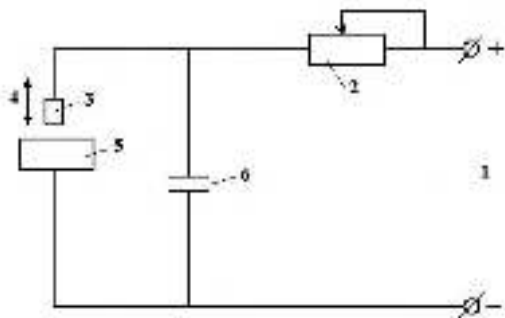
Fig. 1. The method principle for electric spark deposition layers, 1- current source, 2-electrical resistance, 3-electrode, 4-vibrator electrode, 5-piece, 6-capacitor

Electrical discharge can be achieved in air, in different gases, in liquid medium or by deposition on the piece surface of a fixed composition zone. In the case of discharge the liquid medium, it can be used a liquid insulator or an electrolyte with a given composition, according to alloying elements needed into the layer. The electrolyte can be stationary or a jet on the piece surface. Electric spark alloying and deposition facilities are manufactured in a wide range of types and models according to the treated parts and used technologies. Installations can be manual, mechanical or automatic.

3. Experimental researches

Artistic or household items made by plastic deformation or machining ask to have some rough-looking surfaces. This can be achieved by using the deposition electric spark method.

Thin layers were obtained using the electric spark deposition device type Elitron 22A [5]. Nickel electrode was used as filler material. Glossy surface treatment of stainless steel with nickel electrode provides both artistic appearance and corrosion protection. We used 20Cr130 type steel as a base material to determine the liquid environment influence to electric spark deposition with nickel electrode.

Chemical composition was determined with Foundry Master spetrometer and it was presented in Table 1 [2]:

Table 1. The chemical composition of the base material 20Cr130

C	Si	Mn	Cr	Ni%
		[%]		
0.2	0.2	0.3	12.4	0.2

The study was to compare the effects of environments in which we worked. Both the environments were:
-the gas medium-air;
-the liquid medium - oil.

Photographs of surface areas obtained for the surface quality highlight were made by scanning electron microscopy (SEM).

Deposions made in air were with a layer and two layers, and the oil depositions were made with two layers.

3.1. Air medium deposition with nickel electrode, one layer

It is observed an uneven layer to one layer air medium deposition, confirmed also by nickel distribution (Figures 2 and 3).
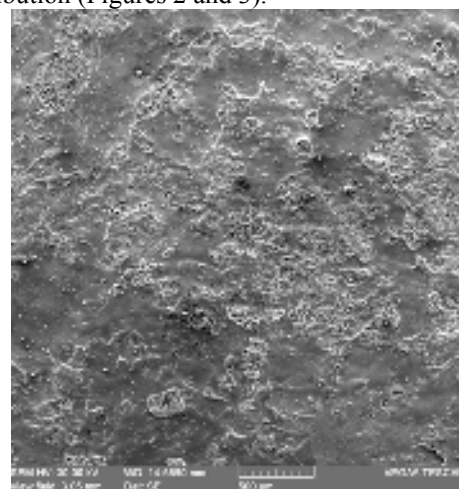
Fig. 2. SEM photographs for relief highlight, 500 μm.
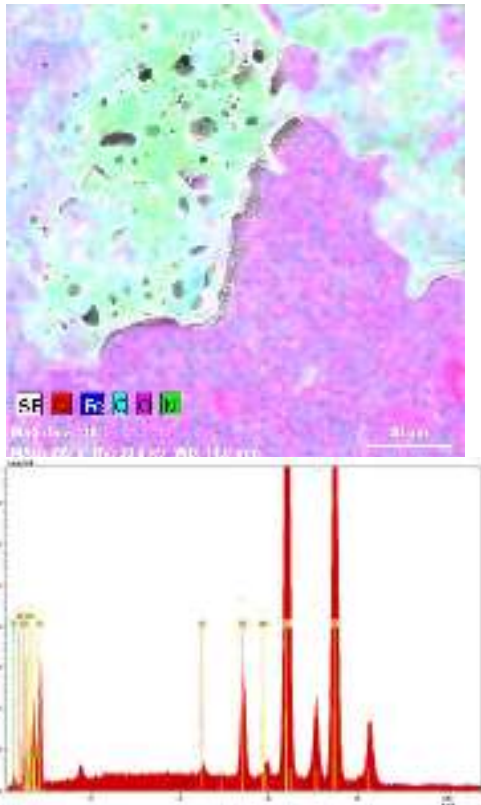
Fig. 3. *Elements distribution: Cr, Fe, C, A, Ni.*

The analyzed area chemical composition is given in Table 2.

Table 2. *The chemical composition for the analyzed area, %*

Element	Atomic Number	Mass percent	Atomic percent
		[%]	
Nickel	28	50.940	46.261
Iron	26	40.882	39.019
Chromium	24	5.017	5.143
Carbon	6	1.852	8.220
Titanium	22	0.604	0.672

Studying the inline analysis, it appears that nickel has a massive presence, but with little continuity, violent reaction to deposition and gas releasing.

This gives the surface a spongy appearance. Oxides are also observed, highlighted in Figure 4.
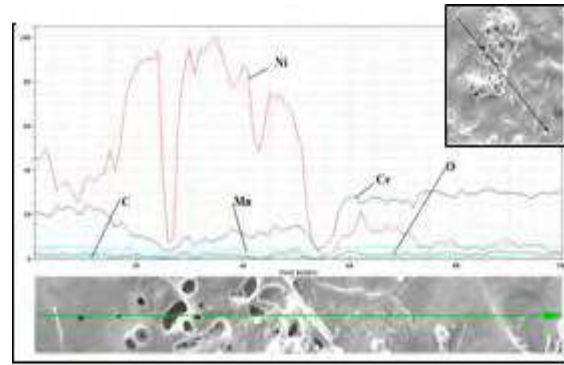

Fig. 4. *Inline analysis for one layer nickel electrode deposition.*

3.2. Air medium deposition with nickel electrode, two layers

The two-layer deposition (Fig. 5) produces uniformly deposited layer, achieving a more uniform distribution of nickel (Fig. 6).

For macrostructure analysis of a single layer deposition (Fig. 7.a) showed inconsistent filling, but to the two-layer deposition (Fig. 7.b) the unevenness is partially removed.

This makes the area look much more pleasant.

For the two layers deposition, the second layer had the effect of remelting to the first filing.

Nickel drops which weren't trapped into the micro area of the first passages were embedded in the melted metal by the second pass.
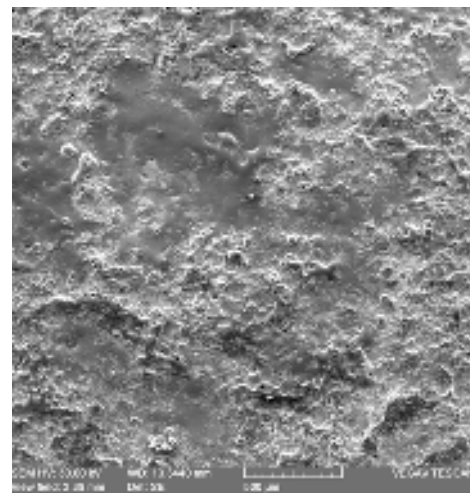
Fig. 5. *SEM photographs of the highlight relief, 500 μm.*

Fig. 6. *Elements distribution: Cr, Fe, Ni*

a)

b)

Fig. 7. *Macrostructure photos obtained upon deposition in the air environment;*
a) one layer deposition, b) two-layer deposition.

In this case also, a chemical composition analysis was made (Table 3), for the investigated area using scanning electron microscope.

Table 3. *The chemical composition for the analyzed area*

Element	Atomic Number	Mass percent.	Atomic percent.
		[%]	
Nickel	28	41.694	35.819
Iron	26	45.694	41.038
Chromium	24	7.601	7.332
Carbon	6	1.667	6.965
Titanium	22	2.426	7.606

Nickel is more evenly represented than the one layer deposition case, but the appearance remains spongy because of intense degassing effect due to reactions occurring on the work piece surface. The relatively high quantity of oxygen presence (2.426%) is highlighted.

3.3. Oil medium deposition with nickel electrode, two layers
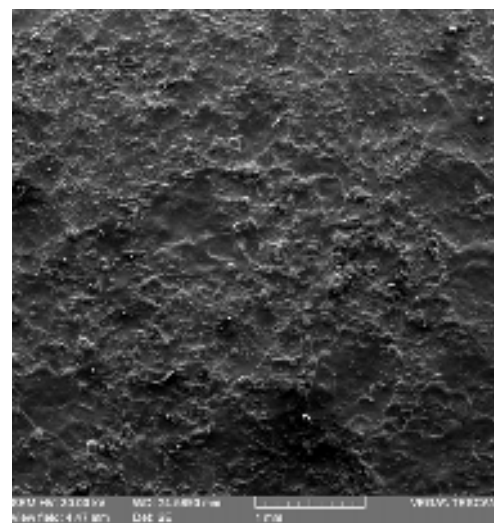
Fig. 8. *SEM photographs of the highlight relief, 1 mm.*

To improve the quality of the deposited layer, two-layer depositions into oil medium were made resulting in a more uniform surface (Fig. 8) and a more uniform distribution of nickel (Fig. 9).

Into the liquid medium deposition process, layer absorbed a larger amount of carbon, which resulted in increased hardness by quenching from the liquid phase. Chemical composition for the analyzed area is presented in Table 4.
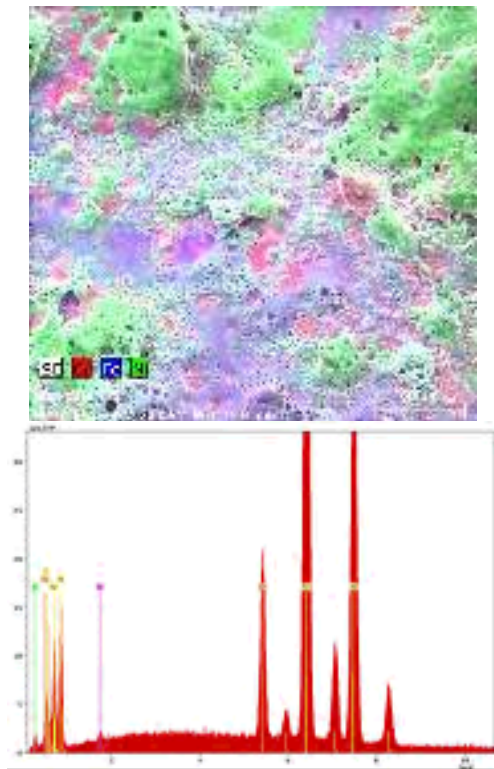
Table 4. *The chemical composition for the analyzed area*

Element	Atomic Number	Mass percentage	Atomic percentage
		[%]	
Nichel	28	25,345	22,022
Fier	26	62,154	56,757
Crom	24	9,239	9,061
Carbon	6	2,566	10,898
Siliciu	22	0,693	1,259

Fig. 10. *Macrostructure photograph obtained with oil medium deposition method, two layers*

The main problem in oil medium deposition by electrical spark method is that once the process is started black carbon occurs which disturbs the process visibility.

4. Conclusions

1. Electric spark treated artistic objects and household gain a pleasant casting aspect, with low roughness.

2. Stainless parts surfaces treated through electric spark maintain their stainless characteristics.

3. Oil medium electric spark method provides better quality for treated surfaces, protecting them from oxides.

Fig. 9. *Elements distribution: Cr, Fe, Ni.*

A positive aspect of the oil deposit is accurate filling, strong environmental protection work due the lack of oxygen. Thus, oxidation disappears, contrary to the air medium deposition case.

From the macrostructure analysis, it result a uniform layer, without oxides (Fig. 10).

References

[1]. **Alexandru A., Strugaru S. I.** - *Alierea şi depunerea superficială prin scânteie electrică - Influenţa tratamentelor termice asupra caracteristicilor straturilor,* Editura Tehnopress, Iaşi, 2008, pg. 5-30

[2]. **Perju Manuela, Nejneru Carmen, Răileanu Tudor, Axinte Mihai, Hopulele Ion -** *Researches concerning the hardening of the grey cast iron through the vibrating electrode method using a WC electrode and in combination with TiC and Ti electrode,* The Annals of "Dunarea de Jos" University of Galati, Fascicle IX. Metallurgy And Materials Science N0. 1, 2008, ISSN 1453-083X, pg.55-59

[3]. **Topală Pavel -** *Electrical charges as mesure for removed metal mass the eelectrical discharge machining,* Iasi, Editura PIM, Nonconventional Tehnolgies Reviev, nr.4, 2007, pg. 103-108

[4]. **Vermesan, G., Vermesan, E., Jichisan-Matiesan, D., Cretu, A., Negrea, G., Vermesan, H., Vlad, M. -** *Introducere în ingineria suprafeţelor,* Editura Dacia, 1999, pg. 272

[5]. ******* *Instalatie Elitron 22,* Academia de Stiinte, Republica Moldova, Chisinau, 1992.

MORPHOLOGICAL ASPECTS OF THERMOSETTING POLYMERS/Zn COMPOSITE COATINGS

Alina – Crina CIUBOTARIU[1], Lidia BENEA[1],
Olga MITOŞERIU[1], Wolfgang SAND[2]

[1]Dunarea de Jos University of Galati,
[2]University of Duisburg Essen, Biofilm Centre,
Aquatic Biotechnology, Duisburg, Germany
email: Alina.Ciubotariu@ugal.ro

ABSTRACT

The present work has the purpose of studying the morphological aspects of composite coatings having zinc matrix and thermosetting polymers (PF resin type NOVOLAC - RESITAL 6358/1 and epoxy resin type DINOX 110L) as dispersed phase obtained during the electrodeposition process of zinc. The composite coatings layers were electrodeposited from a suspension of resin particles in aqueous zinc sulphate electrolyte by adding 10g/L resin particles with size 0.1 - 5μm into electrolyte solution. The structure of the coatings was investigated by scanning electron microscopy (SEM) and atomic force microscopy (AFM) methods. The surface morphology of thermosetting polymers/Zn composite coatings layers is different compared with pure zinc coatings: the regular crystal structure characteristic of electroplated zinc coatings was disturbed. The decreases in the roughness of composite coatings layers compared to roughness of pure zinc layers can be determined by the fine structure of the composite coatings.

KEYWORDS: electrodeposition**,** thermosetting polymers/Zn composite coatings, scanning electron microscopy, atomic force microscopy, roughness

## 1. Introduction

Early humans realized that for some uses, combinations of materials often produced properties in the mixed material, or composite, that were superior to those of the component materials themselves. A more useful but narrower definition of a composite intended for structural applications (i.e., a ''structural composite'') is that it is a combination of a structural reinforcing material in a binder or matrix material.

The key to this definition is that the component materials act together, in concert, to help one another, often synergistically. An enveloping matrix provides protection from damage to reinforcements and adds structural stability to the reinforcements under compressive loading. At the same time, the reinforcing material or reinforcement enhances the strength, hardness, stiffness, and/or toughness of the matrix material.

Modern synthetic composites include every imaginable combination of metals, intermetallics, ceramics, glasses, polymers, and carbonaceous materials (e.g., graphite). A simple pictorialization of possible combinations is shown in Fig. 1 under the form of a Venn diagram.
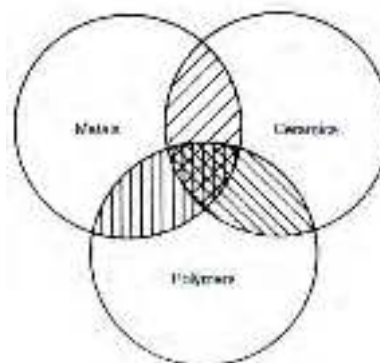
Fig. 1. Venn diagram showing where composites fit among the fundamental materials of metals, ceramics (and glasses) and polymers.

The intersection between any two, as well as among all three, fundamental materials represents a possible composite in which any material could be the

matrix that surrounds the reinforcement, which could be any material. While the matrix material or phase is used to designate the category of composite, the reinforcement-surrounding matrix tends to give the composite its highest level properties (e.g. metallic qualities, ceramic qualities, polymeric qualities). This makes the reinforcing material or reinforcement extremely important, as it usually imparts the functionally specific properties (e.g., strength, hardness, stiffness, toughness, sensing, actuation, etc.) [1 – 4].

Direct structural information on the surface changes due to dissolution and deposition can be obtained by sensitive techniques, such as scanning electron microscopy (SEM) and atomic force microscopy (AFM). Each of these techniques resolves surface structure down to the nanometer scale. However, the image formation mechanisms are quite different, resulting in different types of information about the surface structure.

Since its invention in 1986 [5] atomic force microscopy AFM has become the most widely used form of scanning probe microscope (SPM) with applications in surface, materials and biological sciences [6 – 7]. AFM can create three-dimensional topographic images of surfaces in nanometer resolution and is capable to probe forces in the nanonewton range [8 – 9].

The present work has the purpose of studying the morphological aspects of thermosetting polymers/Zn composite coatings having zinc matrix and two types of thermosetting polymers: first - PF resin type Novolac with commercial name RESITAL 6358/1 synthesized by Hüttenes – Albertus Group (Germany) and the second - epoxy resin type DINOX 110L synthesized by S.C. AZUR S.A. Timişoara (Romania) as dispersed phases obtained during electrodeposition process of zinc.

2. Experimental research

For electrodeposition it was used a zinc plating bath [10]. The pure zinc and composite coatings were obtained at current density of 4 A/dm^2, time for electrodeposition 30 minutes, a stirring rate of 1000 rpm, electrolyte temperature of 25^0C and pH of 3.8 – 4.4.

The PF resin/Zn composite coatings were electrodeposited from a suspension of phenol – formaldehyde (PF) resin particles in aqueous zinc sulphate electrolyte by adding 10g/L PF resin dispersed particles. The size of dispersed particles was of 0.1 – 5 μm.

Phenol-Formaldehyde resin is a highly cross linked thermosetting material that is produced by the poly-condensation of phenol and formaldehyde in the presence of either acidic or basic catalyst. An acid catalyst is usually used in preparing Novolac type resin. A Novolac resin is produced if the mole ratio of formaldehyde to phenol (F/P) is greater than one [11]. This method produces relatively linear chains with molecular weights typically between 500g/mol and 1000g/mol (see Fig. 2).
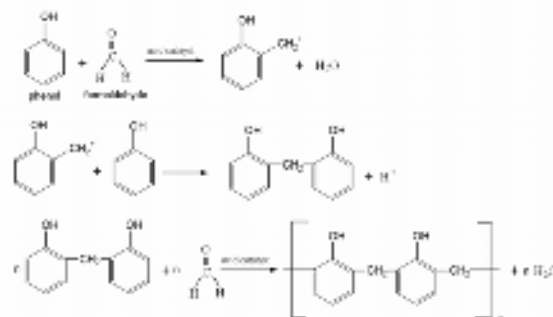
Fig. 2. *The schematic formation of the Novolac type structures.*

The properties of PF resin type Novolac (RESITAL 6358/1) used for obtaining composite coatings are presented in Table 1.

Table 1. *The properties of PF resin (RESITAL 6358/1)*

Property	Value
Molecular weight, g/mol	3392 – 3816
Melting point (DIN 53181)	70 – 80º C
Sliminess at 120^0C (DIN 53081/1)	35 – 45 Pa.s
Free phenol (DIN 16916/2)	< 1% (usually 0.7 – 0.8%)
Water (DIN 51777/1)	< 0.5 %
Flow length at 125^0C melting with 10% hmt (DIN 16916/2)	35 – 44mm
The product is not esterificated	

The epoxy resin/Zn composite coatings were electrodeposited from a suspension of epoxy resin particles in aqueous zinc sulphate electrolyte by adding 10g/L epoxy resin dispersed particles. The size of dispersed particles was of 0.1 – 5 μm.

The epoxy resins (also widely known as epoxide resins and, occasionally, as ethoxyline resins) are characterized by the possession of more than one 1,2 - epoxy group per molecule. This group may lie within the body of the molecule but is usually terminal. The large family of epoxy resins represents some of the

highest performance resins of those available at this time. Epoxies generally out-perform most other resin types in terms of mechanical properties and resistance to environmental degradation, which leads to their almost exclusive use in aircraft components [12].

The schematic formation of the epoxy resin from bisfenol A and epichlorohidryn is presented in Fig. 3 [13] and the properties of epoxy resin type DINOX 110L used for obtaining composite coatings are presented in Table 2.
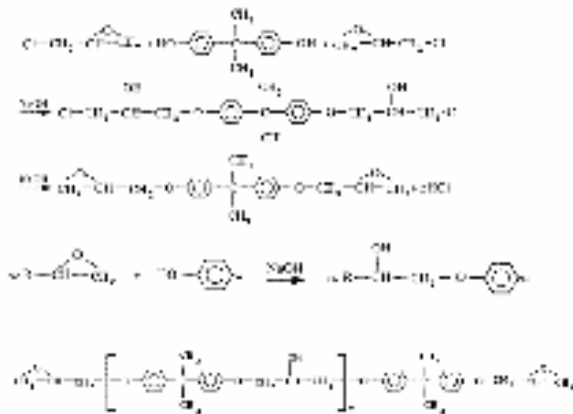
Fig. 3. *The schematic formation of the epoxy resin structures.*

Table 2. *The properties of epoxy resin type DINOX 110L*

Property	Value
Molecular weight, g/mol	500
Density	$1.18 – 1.25$ g/cm^3
Epoxy parameter	$0.185 – 0.220$ equivalents in 100g resin 100%
Melting point	$64 – 76$ºC
Color of iodine	$2 – 4$ mgI$_2$/100cmc
Ash	Maximum 0.05%
Volatile substances contained	Maximum 1%

The morphologies of deposits were examined by Scanning Electron Microscope type JEOL, JSM-T220 A and Atomic Force Microscope type NanoWizard II.

3. Results and discussions

The morphological aspects of pure zinc coating and thermosetting resin/Zn composite coatings obtained by scanning electron microscopy method are compared in Figs. 4 – 6.
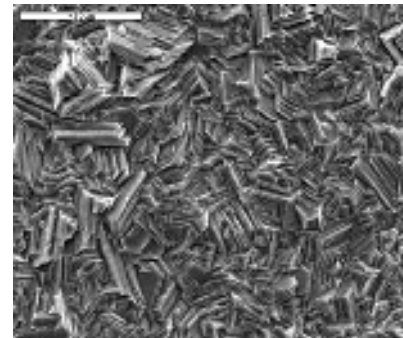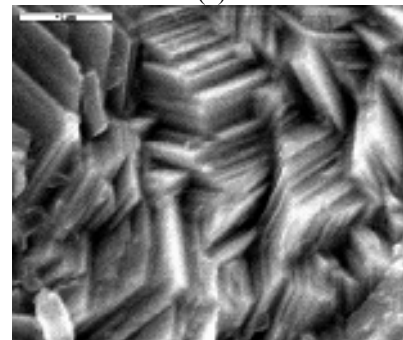
Fig.4. *SEM surface morphology of pure zinc coatings a - x 2000, b – x 15000*
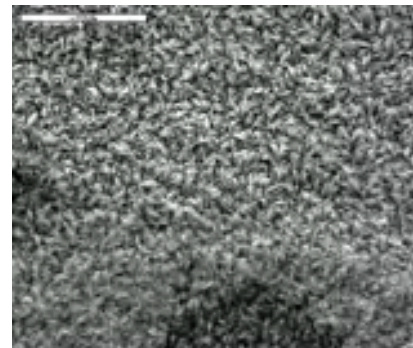
Fig.5. *SEM surface morphology of PF resin/Zn composite coatings a - x 2000, b – x 15000.*
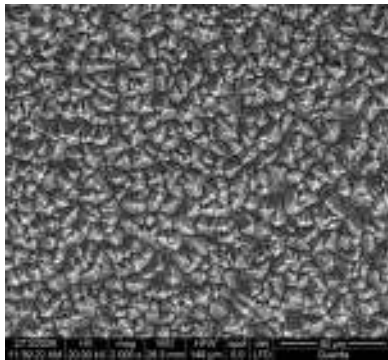
(a)
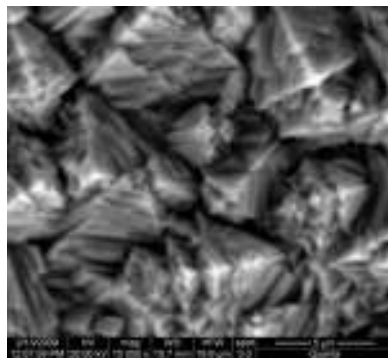
(b)

Fig.6. *SEM surface morphology of epoxy resin/Zn composite coatings*
a - x 2000, b – x 15000.

It can be observed that the surface of zinc is made up of regular crystals. The resin particles codeposited with zinc radically change the structure of the metal: they disorder the regular crystal structure and the structure of the zinc matrix becomes finely crystalline. The pure zinc coatings have a rather regular surface, whereas the composite coating surfaces have finer grains structure with particles of resin uniformly distributed on the surfaces.

The surface structure of pure zinc coatings and thermosetting resin/Zn composite coatings under atomic force microscope are presented in Figs. 7 – 9.

(a)
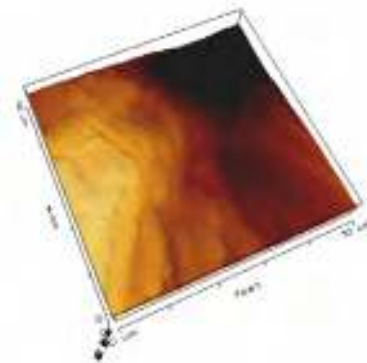
(b)

Fig.7. *AFM 3D images of surface morphology for pure zinc coatings*
a – 25μm x 25μm, b – 10μm x 10μm.
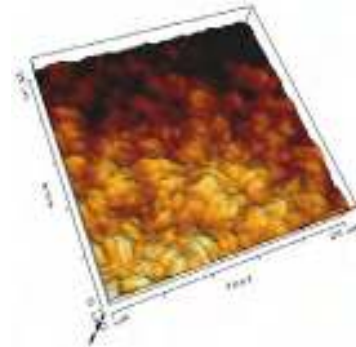
(a)

(b)

Fig.8. *AFM 3D images of surface morphology for PF resin/Zn composite coatings*
a – 25μm x 25μm, b – 10μm x 10μm
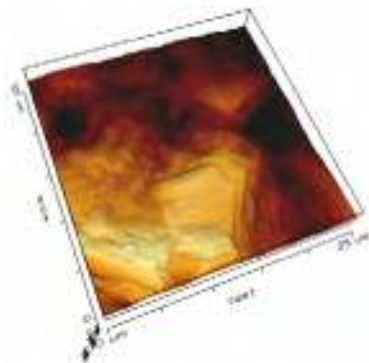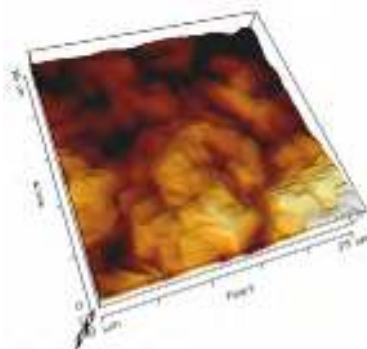
(a)

(b)

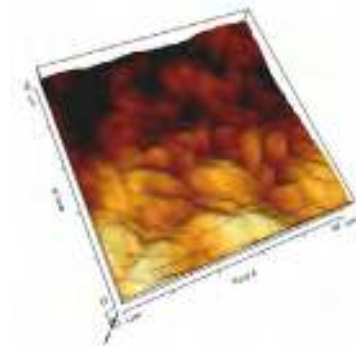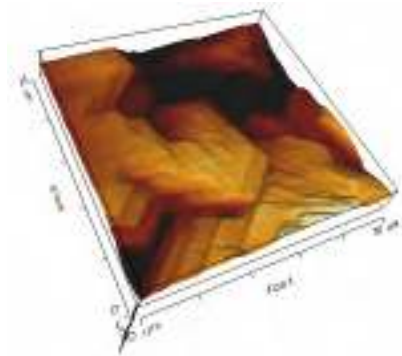**Fig.9.** *AFM 3D images of surface morphology for epoxy resin/Zn composite coatings a – 25 x 25μm, b – 10 x 10μm.*

From the AFM images, it can be said that the surface of zinc is made up of regular hexagonal crystals with a uniform grain size. The PF resin and epoxy resin particles codeposited with zinc radically change the structure of the metal: they disorder the regular crystal structure and the structure of the zinc matrix becomes finely crystalline.

The histograms of the scanned surfaces are presented in Fig.10.
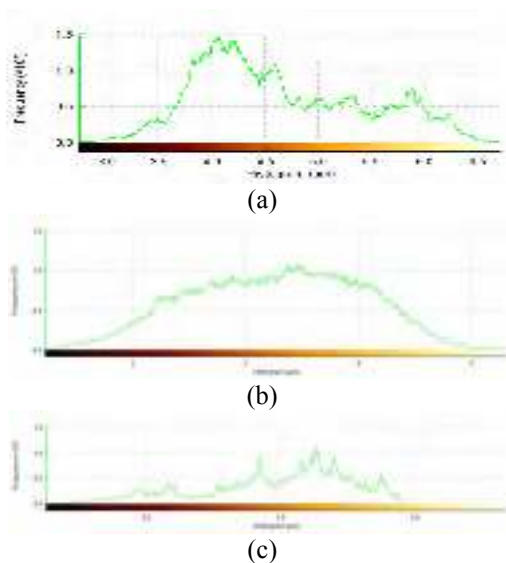
(a)

(b)

(c)

Fig. 10. *The histograms of the scanned surfaces 25μm x 25μm for pure zinc (a), PF resin/Zn (b) and epoxy resin/Zn (c)*

Roughness is a measure of the texture of a surface and plays an important role in determing how a real systtem will interact with the environment. It is quantifed by the vertical deviations of a real surface from its ideal form. If these deviations are large, the surface is rough; if they are small the surface is smooth.

The variation of roughness is presented in Fig. 11.
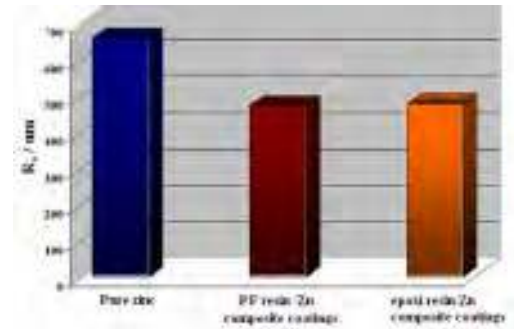
Fig. 11. *Variation of roughness for pure zinc coatings and thermosetting/Zn composite coatings.*

The thermosetting polymer type PF resin and epoxy resin acts as reducing the crystals size of electrodeposited zinc during co-deposition.

The thermosetting polymer could have an inhibition effect on zinc crystals growth and a catalytic effect in increasing nucleation sites.

4. Conclusions

It has been demonstrated that the thermosetting polymer type PF resin and epoxy resin particles could be codeposited with zinc to obtain composite coatings.

The surface morphology of PF resin/Zn and epoxy resin/Zn composite coatings layers is different compared with to pure zinc coatings: the regular crystal structure characteristic of electroplated zinc coatings was disturbed.

The resin particles embedded in the zinc matrix perturb the zinc crystals growth during electrodeposition.

From the analyses of histograms and variation of roughness it can be concluded that by adding the PF resin and epoxy resin particles in the zinc electrolyte solution the roughness of the composite coatings layers compared to the roughness of pure zinc layers decreases.

These decreases in the roughness of composite coatings determined changes the surface structure of composite coating to finer crystallites and smoothness.

References

[1]. R. A. Flinn and P. K. Trojan - *Engineering Materials and Their Applications*, 4th ed. Boston, Houghton Mifflin Company, 1990

[2]. F. L. Matthews - *Joining Fibre-Reinforced Plastics*, London, Elsevier Applied Science, 1987

[3]. A. B. Strong - *Fundamentals of Composites Manufacturing: Materials, Methods and Applications,* Dearborn, MI, Society of Manufacturing Engineers, 1989

[4]. Robert W. Messler Jr - *Joing of advanced Materials*, Butterworth-Heinemann, Stoneham, UK, 1993

[5]. G. B. Binnig, C. F. Quate and Ch. Gerber - *Atomic Force Microscope*, Phys. Rev. Lett., vol. 12, p.930 – 933, 1986

[6]. J. K. H. Horber and M. J. Miles - *Scanning Probe Evolution in Biology*, Science, vol. 302, nr. 5647, p. 1002 - 1005, 2003

[7]. F. Oesterhelt, D. Oesterhelt, M. Pfeiffer, A. Engel, H. E. Gaub and D. J. Muller - *Unfolding Pathways of Individual Bacteriorhodopsins*, Science, vol. 288, nr. 5463, p. 143 - 146, 2000

[8]. G.W. Reynolds, J. W. Taylor, *Correlation of Atomic Force Microscopy Sidewall Roughness Measurements with Scanning Electron Microscopy Line-Edge Roughness Measurements on Chemically Amplified Resists Exposed by X-ray Lithography*, J. Vac. Sci. Technol. B., vol. 17, issue 6, p. 2723 - 2729, 1999.

[9]. R. Nessler - *Scanning Microscopy Technologies: Scanning Electron Microscopy and Scanning Probe Microscopy*, Scanning, vol. 21, issue 2, p. 137, 1999

[10]. A. C. Ciubotariu, L. Benea, O. Mitoseriu, P. Ponthiaux, F. Wenger - Influence of particles size on the structure and corrosion behavior of phenol – formaldehyde/Zn composite coatings obtained by electrodeposition, J. Optoelectron. Adv M., vol. 11, nr. 6, p. 892-897, 2009

[11]. W. Wei, H. Hu, L. You, G. Chen - *Preparation of carbon molecular sieve membrane from phenol-formaldehyde Novolac resin*, Carbon, vol. 40, issue 3, p. 465 - 467, 2002

[12]. J. A. Brydson - *Plastics Materials: Seventh Edition, Chapter 26 Epoxide Resins*, ISBN- 13: 9780750641326, Elsevier Butterworth-Heinemann, UK, 1999

[13]. A. Clayton May - *Epoxy Resins: Chemistry and Technology*, New York: Marcel Dekker Inc, ISBN 0824776909, 1987.

INVESTIGATION OF TITANIUM HYDRIDE PRODUCED FROM TITANIUM WASTE

Yavor LUKARSKI[1], Jordan GEORGIEV[1], Lubomir ANESTIEV[1], Rositsa GAVRILOVA[2], and Simona BEJAN[3]

[1]Institute of Metal Science, Bulgarian Academy of Sciences, Sofia, Bulgaria
[2]University of Chemical Technologies and Metallurgy, Sofia, Bulgaria
[3]Politechnica University of Bucharest, Romania
e-mail: lukarski@ims.bas.bg

ABSTRACT

The work presents an original method for titanium hydride production by hydrogenation and dehydrogenation of titanium waste in a specially designed for this purpose vacuum chamber. Laboratory quantities of titanium hydride were prepared using LaNi$_5$ hydrogen accumulator as a source of pure hydrogen. Chemical, X-ray, DTA, TG and granulometric analysis of the obtained hydride were made. The analyses carried out in the temperature range, 680-1070 K, DTA, TG and mass-spectrometry analysis allowed determining the activation energy of decomposition of the obtained TiH$_2$ which was approximately E= -135.5 kJ/mol and the standard enthalpy of formation ΔH= -140 kJ/mol.

KEYWORDS: hydrogen, titanium waste, titanium hydride

1. Introduction

The use of titanium and titanium alloys grows by 8-10% per year [1]. This also leads to increasing the amount of produced titanium wastes. For this reason, the problem of utilizing these wastes comes to the fore. There are different methods for utilization but the recently most widely applied one is hydrogenation of titanium in the presence of hydrogen to titanium hydride (TiH$_2$) formation. The latter represents grey-black powder with molecular weight of 49.53-49.90 g/mol, specific density of 3.75 g/cm^3 and hydrogen content within the range of 3.85-4.02 % (by weight).

The results from the investigation on some characteristics of the titanium hydride produced by the team are given in this work.

2. Methodology of the experiment

The experiments were carried out using specially constructed equipment for this purpose [2]. Fig. 1 shows the photo of this equipment. The main feature is the use of a hydrogen accumulator as a hydrogen source, which solves the problems with hydrogen utilization.

The main elements of the equipment are: heating furnace, programmable thermoregulator, reaction chamber, vacuum system, hydrogen source, system for hydrogen feeding, system for temperature measurement, system for recording the pressure in the hydrogen accumulator and the reaction chamber, system for charging the hydrogen accumulator.

The initial raw materials subjected to hydrogenation are shavings of pure titanium and titanium alloy. The chemical composition is obtained according to the ACP-AES method and is shown below:

• Pure Ti: 0.081% Al, 0.0014% Mn, 0.0034% V;

• Titanium alloy: 0.504% Al, 0.0065% Mn, 0.0197% V.

The experiments were carried out at three different temperatures of the furnace, adjusted by the thermoregulator–873, 923 and 973 K. The sequence of operation of this installation is as follows:

The titanium crucible wastes in the form of briquettes and a thermocouple is placed in the reactor, which is closed hermetically under vacuum. Another thermocouple is placed in the zone of the crucible, which measures the temperature defined by the thermoregulator.

The vacuum in the reactor is achieved by a vacuum pump with all turn-cocks closed. Then the intermediate cock to the vacuum pump is closed and the cock to the hydrogen accumulator is opened.

Fig. 1. *Installation for producing TiH₂.*

Hot water is fed into the accumulator cylinder and the transfer of hydrogen to titanium is started. The furnace heater is switched on, the temperature regime of heating and soaking being preliminarily set by means of the programmable thermoregulator. The heating rate is 10°C/min. When reaching the maximum temperature, the feeding of hydrogen by the accumulator has ceased. The titanium hydrogenation reaction is started at a definite temperature and the pressure of hydrogen in the reactor is decreased. At the moment, when hydrogen pressure stops falling, a new portion of hydrogen is fed to the set pressure.

The procedure is continued until hydrogen pressure remains unchanged after the consecutive feeding of hydrogen. This is an indication that the hydrogenation process is completed and the furnace is switched off.

After cooling of the reaction zone to 50°C cold water is fed to the hydrogen accumulator in order to absorb the non-reacted hydrogen.

For this purpose, the turn-cock of the accumulator is opened.

After evacuating the hydrogen the turn-cock of the accumulator is closed, the reaction zone is subjected to vacuum and the reactor is filled with SO_2 or argon to protect titanium hydride against combustion.

The reactor is opened and the ready product is taken out. The change of the actual temperature in the reaction zone is shown in *Fig. 2*.

The exothermal peaks of the titanium hydrogenation process are clearly outlined.
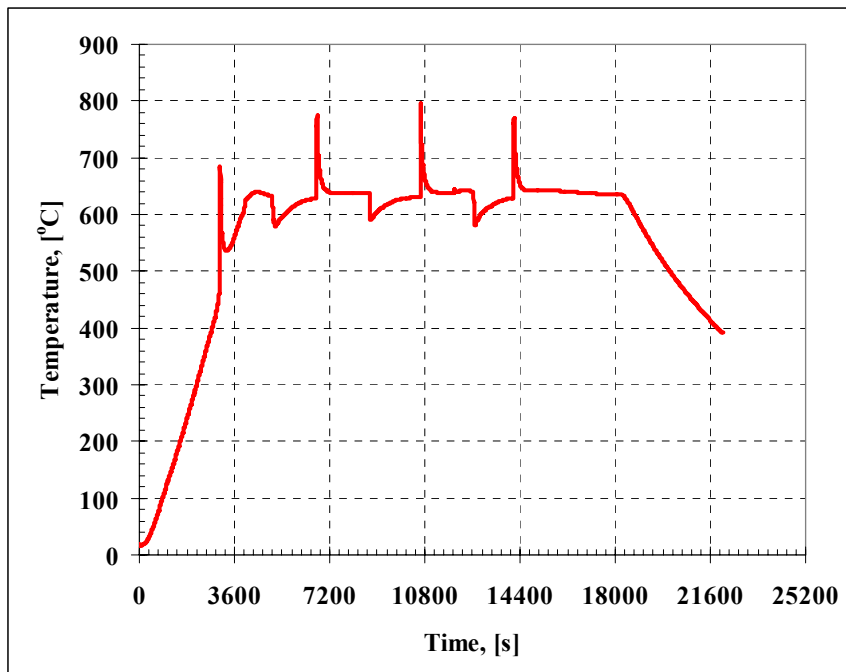
Fig. 2. Temperature change in the reaction zone.

3. Results and analysis

3.1. Granulometric analysis

The performed granulometric analysis of the produced and ground titanium hydride shows that 93.45 % of the product has a grain-size lower than 20 μm.

3.2. X-ray structural analysis

Figure 3 shows the results from the X-ray structural analysis of a titanium hydride sample using a Bruker D8 Advance diffractometer.

The only phase is $TiH_{1.924}$. No lines of titanium are observed, which shows that practically the whole titanium quantity is bound into titanium hydride.
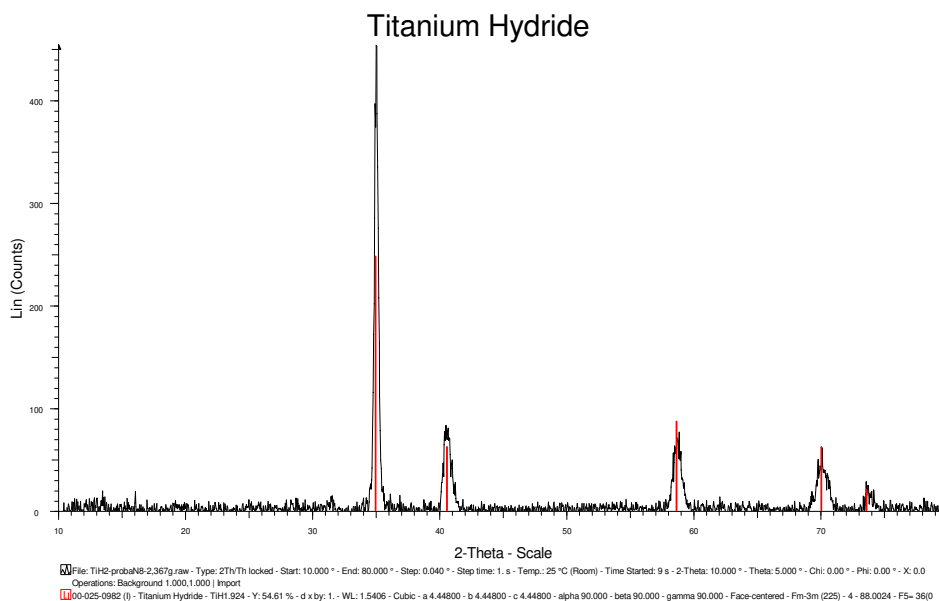
Fig. 3. X-ray diagram of a titanium hydride sample.

3.3. Thermal analysis

Samples of the produced titanium hydride are subjected to thermal and mass-spectrometric analysis. It is performed by a DTA-analyzer LABSYS-evo, combined with a mass-spectrometer of the Setaram Company. The differential thermal analysis (DTA) is carried out for five heating rates of 5, 8, 10, 12 and 15 K/min in argon atmosphere to a maximum temperature of 800°C. Figure 4 presents the obtained DTA-curves for 5 and 12K/min. The temperatures with local extremum – T_{max}, are determined for the five curves.

They are processed according to the method of Kissinger [3] (the equation shown below) and the value of the activation energy of titanium hydride decomposition is determined from the slope of the straight lines in Fig. 5–E=-135.5 kJ/mol. Here β designates the heating rate, E – the activation energy, R–the gas constant.

$$\frac{E}{RT_{max}^2} = \frac{A}{\beta} \exp\left(-\frac{E}{RT_{max}}\right)\left(-\frac{df(\alpha)}{d\alpha}\right)_{T=T_{max}}$$

a *b*
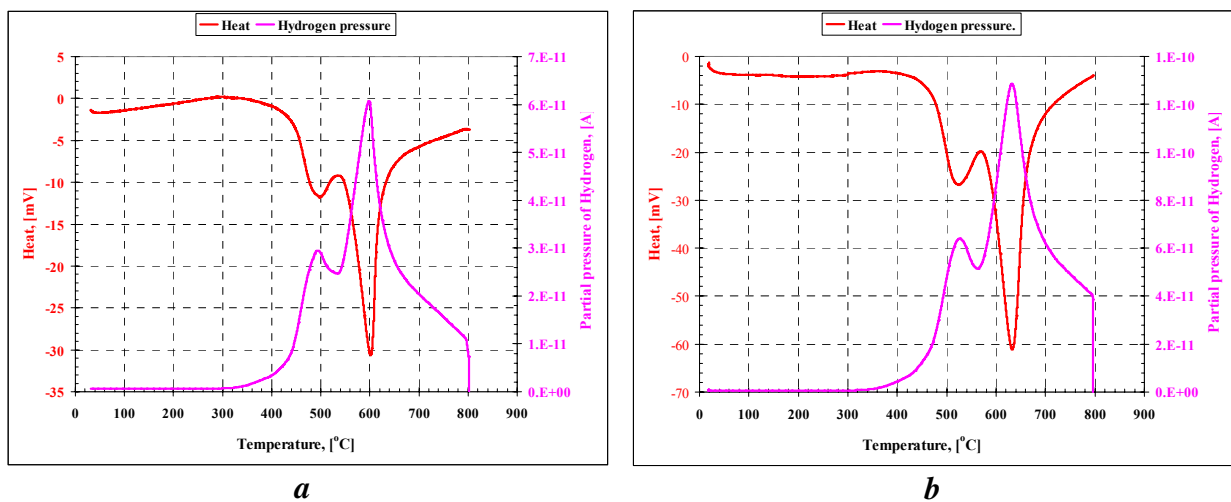
Fig. 4 (a, b). *DTA curves of TiH$_2$ decomposition for different heating rates,*
(a) -5 K/min, (b) - 12 K/min.
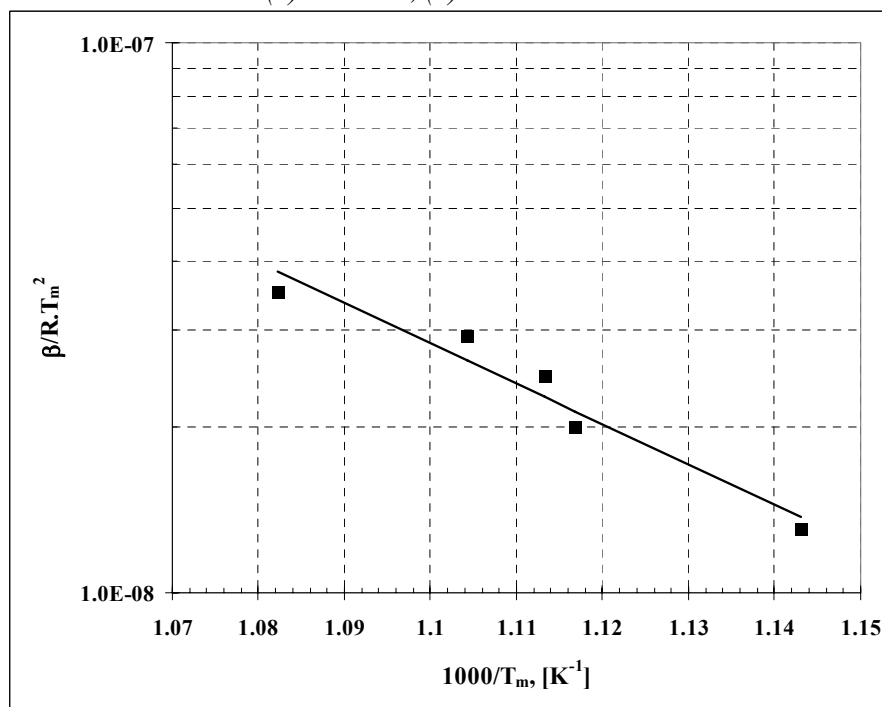
Fig. 5. *Kissinger plot of the data for T$_{max}$ obtained for the DTA curves.*

4. Conclusion

A laboratory installation has been developed for producing titanium hydride by treatment of titanium wastes with hydrogen and laboratory quantities of the hydride have been obtained. An original method is applied for feeding the hydrogen from a hydrogen accumulator. The granulometric composition of titanium hydride has been determined. The X-ray structural analysis shows the existence of only the $TiH_{1,924}$ phase.

The carried out thermal analysis provided the possibility of determining also the enthalpy of the produced titanium hydride. The value of standard enthalpy of formation obtained by us -140 kJ/mol is in agreement with the value found by other authors [4-6]. On the basis of the results from thermal, thermogravimetric and mass-spectroscopic analysis of titanium hydride samples the activation energy of decomposition of the produced titanium hydride is determined. It is approximately E= -135.5 kJ/mol.

Acknowledgment

References

[1]. www.*roskill.com.*

[2]. **Georgiev, J., Y. Lukarski**. *Laboratory Installation for Producing TiH₂ by Hydrogen*. Processing. 5th Congress of the Society of Metallurgists of Macedonia with International Participation, Sept. 17-20, 2008, Ohrid, Macedonia, CD ISBN 978-9989-9571-4-7, M8-02-E.

[3]. **Kissinger, H. E**., Reaction kinetics in differential thermal analysis, *Anal. Chem.* **29** (1957) 1702-1706.

[4]. **Jing-wei Zhao, Hua Ding, Xue-feng Tian, Wen-juan Zhao and Hong-liang** *Hou Chin*. *J. Chem. Phys*. 21 (2008) 569-574.

[5]. **E. Koenigsberger, G.Eriksson and W. A. Oates**, *Journal of alloys and Compounds*, 299 (2000) 148-152.

[6]. **A. San-Martin and F. D. Manchester**, *Bulletin of Alloy Phase Diagrams*, 8(1) (1987) 30-42.

DIMENSIONLESS NUMBERS IN THE ANALYSIS OF HYDRODYNAMIC INSTABILITY OF INTERFACE STEEL - SLAG AT MICROSCALE IN REFINING PROCESSES

Petre Stelian NITA

"Dunarea de Jos" University of Galati
email: pnita @ugal.ro

ABSTRACT

In evaluation of the local hydrodynamics of interface, in steel-slag refining processes influenced by solutal effects, adequate scales of length and time satisfying certain conditions are necessary to get a correct and suggestive image of the weight of factors possible to be used in industrial technologies. These could be obtained based on already established common dimensionless numbers but carefully applied in a specific manner, taking into consideration particularities of the established interface and the main involved process. Based of the general philosophy of building dimensionless artificial conglomerates, a new dimensionless group $Ni = Ma \cdot Bo$ is proposed in this paper as a consequence of needs to evaluate particularly the effects of capillarity actions at interface, especially of solutal origin, in presence of other physico-chemical and physical actions, especially when the effects of capillarity prevail over all others.

KEYWORDS: steel refining, hydrodynamic instability of interface, length scale, time scale, dimensionless numbers.

1. Introduction

Despite the fact that capillarity is recognized as an important phenomenon in hydrodynamics of interface, only extremely rare and more than prudent approaches of this subject are present in scientific and technical papers dealing with process at interfaces in metallurgical systems steel-slag. Therefore in the following paragraphs there is a short introduction in the specific problems and aspects of this class of systems and this represents an attempt of the author to open in a certain measure new doors in the fundamentals of some new metallurgical processes of refining based on the advanced knowledge. As a main approach, specific dimensionless numbers are presented and comments are made on the connections with the hydrodynamics of interface steel-slag.

Solutocapillarity plays an important and particular role in the hydrodynamics of interface between liquid phases of technological interest in steel refining under slags.

The amplitude of the local fluctuations of concentrations at interface between steel and slag is limited compared to the possible local fluctuations of temperature in other systems or when strong gradients of temperature are imposed externally by special techniques or devices. Supplementary, the depths of the layers of steel and slag are of a certain established

extend because of the final purpose of the applied treatments which is to provide a certain appreciable high amount of refined steel, presenting a high level of purity concerning harmful elements. Oxygen, sulphur and phosphorus are the most frequently target elements of treatments applied to steels using slags. Several problems in analyzing the influence exerted by the presence of surface active solute in the liquid phases composing the refining system steel-slag are analyzed in a simplified manner due to their low specific concentrations [1][2].

At low levels of concentrations of surface active solutes, their influence on density is insignificant, also the corresponding aspects of buoyancy due to variations of density. Up to values of maximal concentrations of 2 mass% sulphur in slags and 0.02% mass% sulphur in steel, which are specific to desulphurization process at industrial scale, there are not reported sensible variations of density in the respective liquid phases, compared to the densities of the same liquids in absence of sulphur. Therefore it is possible that aspects of buoyancy could be totally neglected.

The solutocapillarity due to surface tension gradient produced by perturbation of concentration is a factor of instability while the surface tension acts to stabilize the interface; viscosity, diffusion and gravitation are also stabilizing actions. Viscous

diffusion acts to dampen the concentration fluctuations and the associated fluid flow. The gravity acts physically to flatten the interface and thus to stabilize the deformational perturbations. The presence of a heavier liquid phase below a lighter one (as it is the case of steel under slag) is also a stabilizing factor.

If it is intended to put in evidence the absolute role of the destabilizing factor–solutocapillarity in promoting flow, it is necessary that other destabilizing factors or factors damping the solutocapillarity effects to be minimized at certain level, bellow a certain threshold value of the involved parameter. This could be performed selecting or imposing values of different parameters in a physically acceptable range and leading finally to an adequate time scale. Several general remarks regarding properly named operations in scaling and in its preliminary stages and considerations are useful by their close relation with the technological and physical reality and utility. In this sense, in an such analysis principle of in acts a certain incertitude; imposing too restrictive conditions to obtain favorable conditions of prevalence of a certain physical action, compared to another, not only that this could not serve too much, but it could block the utility of the respective scale. For example, the characteristic time scale which is dependent upon the characteristic length at different powers. These negative aspects could be totally avoided by a correct scaling operation based on a correct meaning of the processes and on an adequate selection of the dimensionless numbers used in these cases. Further going there is also the possibility to introduce a new dimensionless number taking into account the need to evaluate the simultaneous complex action of many several forces involved in interfacial flow and dynamics as it is more and more encountered in literature.

2. Dimensionless numbers involved in the interfacial hydrodynamic instability

2.1 Principles and particularities

Technological systems in steel refining under slags could be included in the class of complex process of multi-phase flow, where a fluid interface separates immiscible phases, presenting a certain surface tension(σ_{steel} ,σ_{slag}) and leading to certain interface tension(σ_i).The fluid interface is deformable, it has an unlimited extend, reported to the dimensions of the interfacial layer thickness and it is unbounded at wall, that means the interface is in the free-slip condition. This is generally valid if the friction at interface could be neglected or included in other quantified physical factors. Therefore, there is a force balance at slag-steel interface and this could be decomposed into normal components (normal stress and pressure) and a tangential component (shear stress). Boundary conditions at interface lead to the following physical considerations [3]:

1. jump in fluid pressure is balanced by interface tension;

2. jump in fluid stress is balanced by surface gradient of interface tension (gradient along the interface) $\nabla_S \sigma_i$.

Macroscopic interfacial no-slip conditions break when at microscale, processes due to surface tension gradient, become relevant as magnitude. Analysis of this class of processes could be performed in conditions of the existence of a deformable interface but which doesn't deform because of the small weight of factors leading to deformations. This situation could be encountered at least in the incipient state of considered flow, or during time intervals where required conditions are accomplished. This is the case when physical actions producing deformations are not dominant in comparison to others. It results that, in conditions of adequate scaling of length and time of different actions, computations of parameters regarding the resulting particular and specific flow are realistic and possible to be made.

The known dimensionless numbers are limited as possibilities to give a good image of the physical reality in the problems mentioned in title. Several of them use a characteristic length with a certain specificity which differs from a phenomenon to another (it is well known that there are different independent scales of length). In fact, the main problem in the analysis of local instability produced by different actions, including the mass transfer of a surface active element, consists in a correct and specific scaling of length, velocity and time. It is known that every physical or physicochemical action is characterized by scales of length, time and velocity which are almost independent among them, but when actions are simultaneous, the fastest action has the largest probability to occur. If it is analyzed the occurrence of a certain physical or a physicochemical action it is necessary to scale the time and the conditions when it is the dominant action with a certain high degree of certitude. This is usually made establishing the condition when the time scale is shorter with at lest an order of magnitude, compared to other concurrent actions. From this condition a characteristic length scale results, and in certain conditions, also a velocity scale results. Other times it is possible to start the scaling from velocity, instead of time and then the characteristic length and time result on this base.

This kind of analysis is often the single way to get some information on the possible behavior of a system and to perform a simulation concerning the behavior of the considered system. In the system

steel-slag at liquid phases temperature it is obvious the difficulty of any direct observation. Some enough valuable data could be obtained using the rapid solidification method of samples containing portions of interface steel-slag.

Many dimensionless numbers represent ratios of two physical actions (forces) or of two families of actions. This level of synthetic representations despite extremely useful, does not satisfy the actual necessities, mainly consisting in the enlargement of the set of actions evaluated in such manner.

At small time and length scales, different phenomena leading to thermodynamic equilibrium exhibit strong particularities affecting the hydrodynamics in a dramatic manner. Local fluctuations of temperature and concentration at the interface or at free open surface alter locally the surface tension and if these local inhomogeneities are continual and persistent enough time, they could give a spontaneous flow (Marangoni effect). Therefore it is necessary always to relate the analyzed processes to adequate scales of time and of length. In such conditions the surface tension gradients $\partial\sigma/\partial x$ contribute to a force proportional to the thermal coefficient $|\partial\sigma/\partial T|$ or to the concentration coefficient $|\partial\sigma/\partial c|$ of interface tension. In this paper only the influence of concentration will be considered, based on the physical reality consisting in much more values of the thermal diffusion and conductivity in slag and steels, compared to their mass equivalents.

2.2. Dimensionless numbers derived from the normal component of the free slip boundary condition

The normal component of the free-slip boundary conditions gives by scaling the **Laplace number(La)**; it represents a ratio of surface tension and inertia forces to the viscous forces, expressing the momentum-transport (especially dissipation) inside a fluid. **La** dimensionless number is linked to the free convection inside of immiscible fluids and is defined by the relation:

$$La = \frac{\sigma \cdot \rho \cdot L}{\mu^2} = \frac{\sigma \cdot L}{\rho \cdot v^2} \qquad (1)$$

where: σ – is surface tension; ρ – is density; L – is characteristic length; μ – is dynamic viscosity; v – is kinematic viscosity, also called momentum diffusivity.

Another form is Ohnesorge number **Oh=La⁻²**.

Bond dimensionless number (Bo), also called the static Bo number in opposition with another form called dynamic Bond dimensionless numb er is given by the following ratio [5]:

$$Bo = \frac{\rho \cdot a \cdot d^2}{\sigma} \qquad (2)$$

Where: ρ – is the density, or the density difference between fluids; a – is the acceleration of the body force.

Mainly Bo dimensionless number could be derived from the general dimensionless number N introducing gravitation scaling of the pressure P.

It quantifies the importance of body forces over the surface tension forces, connected with the role of equilibrium capillarity (σ). When the acceleration a is gravity acceleration g, The Bo number is the most common comparison of gravity and surface tension effects, usually used to find the characteristic length scale in complex scaling problems.:

$$Bo = \frac{\rho \cdot g \cdot d^2}{\sigma} \qquad (3)$$

Surface tension dominates the flow at small values of d, this being the single parameter of a given system where the density, and gravity acceleration are constant and there is a certain variability of surface tension upon the concentration of a surface active solute. At interface steel-slag the competition between stabilizing factors of interface is from far in favor of surface tension if the length scale is small enough. A value $Bo<1$ indicates that surface tension dominates. The problem which is still persistent is to establish the length scale d. At $Bo=1$ the capillary length scale is obtained:

$$L_c = (\sigma/\rho \cdot g)^{1/2} \qquad (4)$$

At an interface between two immiscible superposed liquids of density $\rho_{top} = \rho_1$ and $\rho_{bottom} = \rho_2$ the capillary length is obtained replacing ρ by $\Delta\rho = \rho_2 - \rho_1$:

$$L_c = (\sigma/\Delta\rho \cdot g)^{1/2} \qquad (5)$$

If the interface tension gradient is persistent enough time and is continual on interface, it could be taken into account also in the relation giving the capillary action of the interface tension gradient of solutal origin:

$$L_c = (\Delta\sigma/\Delta\rho \cdot g)^{1/2} \qquad (6)$$

At lengths $L \leq L_c$ the capillarity prevails over gravity. This limit extend of action of capillarity must be corrected, taking into consideration the values where the capillarity prevails over other competing actions.

Other forms expressing the ratio between gravity forces and surface tension are also used in the form of other dimensionless numbers.

Influences exerted by the solutal effects, reflected in the interfacial tension coefficient, using the Rayleigh number and the dynamic Bond (Bo_d) number, where the relative importance of buoyancy is

evaluated, are difficult to be put into evidence. Despite the fact that the Rayleigh dimensionless number usually refers to thermal effects on buoyancy due to the modifications of concentration, it can also refer to the solutal effects but only related to the modifications of the density due to this kind of effects.

Capillary dimensionless number (Ca), also called as **crispation dimensionless number (C)** [6] is specific to situations where the scale of stresses in presence of surface tension is a viscous one.

It is given by the relation:

$$Ca = \sigma/\mu \cdot V \qquad (7)$$

Where V – is the velocity scale.

If the velocity scale is given by the mass diffusion (D-isothermal mass diffusion coefficient), in a layer of depth d:

$$V = D/d \qquad (8)$$

Which gives:

$$Ca = \frac{\sigma \cdot d}{\mu \cdot D} = Bo \cdot Ga \qquad (9)$$

Another form using the same notation is the inverse form:

$$Ca = \frac{\mu \cdot D}{\sigma \cdot d} = Bo/Ga \qquad (10)$$

If the velocity scale is Marangoni velocity V_{Ma}, the capillary number can be written in the form:

$$Ca = \frac{(-\partial\sigma/\partial C) \cdot \beta \cdot d}{\sigma} \qquad (11)$$

In fluid dynamics, the Ca number in the form of rel.(10) expresses the relative effect of viscous forces versus surface tension acting across an interface between a liquid and a gas, or between two immiscible liquids. When $Ca < 10^{-5}$ it is possible to neglect the effects of viscous forces compared to surface tension and this is specific to many liquids.

The dimensionless number Ca is useful but needs again a specified value of the characteristic length d which remains also to be established at an adequate magnitude, corresponding to necessities.

The inversely written is convenient in treating the Ca and Ga in the same way in the stress balance at boundaries.

Weber dimensionless number (We) [7] characterizes the relative importance of the deformability of an interface, giving a measure of the relative importance of the inertia of fluids compared to its surface tension, according to the relation:

$$We = \frac{\Delta\rho \cdot V^2 \cdot d}{\sigma} \qquad (12)$$

Where: ρ- is the density of the fluid; V- is the fluid velocity; d-is the characteristic length; σ- is the surface tension. In conditions of terrestrial gravity g,

replacing $V^2 = g \cdot d^2$, the dimensionless number We can be written as:

$$We = \frac{\Delta\rho \cdot g \cdot d^2}{\sigma} \qquad (13)$$

The characteristic length in the case of a drop is its diameter. When inertial effects dominate over viscous effects, the stress could be expressed in dimensionless form based on the inertial scale. We number, which expresses the relative influence of inertia and hydrodynamic pressure related to the capillary pressure, it is particularly useful in analyzing fluid flow where there is an interface between two different fluids, especially for multiphase flows presenting curved surfaces, as it is the case of drop or bubble migration with significant surface deformation.

Apart from the above dimensionless numbers there are others expressing also relations between important physical actions involved in hydrodynamic stability/instability of interfaces between fluids. These numbers could be obtained as composites of some already established dimensionless numbers. **Galilei dimensionless number (Ga)** is one of them and results as the ratio of gravity forces divided by viscous forces[8], as ratio of dimensionless numbers Bo and Ga, or more simply forming a dimensionless group of quantities g, v, D related to the same characteristic length scale d:

$$Ga = \frac{Bo}{Ca} = \frac{g \cdot d^3}{v \cdot D} \qquad (14)$$

In terms of characteristic time scales, the dimensionless number Ga could be written as it follows:

$$Ga = \frac{\tau_{diff} \cdot \tau_{visc}}{\tau_{grav}^2} \qquad (15)$$

Where:

$\tau_{diff} = d^2/D$ – is the time scale of mass diffusion; $\tau_{visc} = d^2/v$ – is the time scale of viscosity; $\tau_{grav} = (d/g)^{1/2}$ – is the gravity time scale.

The Galilei number is used more frequently in viscous flow and thermal expansion calculations, for example to describe fluid film flow over walls. By extension it could be used for the case of fluid flow at interfaces on a side or the other side of interface. In these cases the mass diffusion coefficient of the considered solute and the kinematic viscosity of the considered fluid will be taken into account in calculations.

The gravity time scale considered τ_{grav} represents in this case the time needed for a body to travel a distance d under the gravity acceleration g.

Considering the Boussinesq approximation and using the definitions of Rayleigh dimensionless number and Galilei dimensionless number, a parameter called Boussinesq parameter could be computed:

$$Ra/Ga = \alpha \cdot \Delta T \qquad (16)$$

From here it follows that

$$\tau_{grav}/\tau_{buoy} = (\alpha \cdot \Delta T)^{1/2}$$

Further, other useful expressions of Ga number will be presented in the context of the present paper.

2.3. Dimensionless numbers derived from the tangential component of the free slip boundary condition

The Marangoni dimensionless number (Ma) is linked to the Marangoni effect (sometimes also called the Gibbs-Marangoni effect) which consists in the mass transfer along an interface due to surface tension gradient. The surface tension gradient can be caused by a concentration gradient or by a temperature gradient. The presence of a gradient in surface tension will naturally cause the liquid to flow away from regions of low surface tension. The Marangoni number for the solutal case, valid for isothermal conditions, is the ratio of capillary force due to the surface tension gradient of solutal origin to the viscous drag in the flow. It can be defined in several ways but an accepted form of larger utility is the following [9]:

$$Ma = \frac{(-\partial\sigma/\partial C) \cdot \Delta C \cdot L}{\mu \cdot D} \qquad (17)$$

Where: $\partial\sigma/\partial(C)$-is the concentration coefficient of the surface tension or of the interfacial tension, related to the surface active solute C, in $N \cdot m^{-1} \cdot (mass\%)^{-1}$ or in $N \cdot m^{-1} \cdot (mole \ fraction)^{-1}$; $\Delta(C)$-is a characteristic concentration difference across the liquid layer of slag or, after case, along its surface, expressed in terms of solute (C) content, in mass% or mole fraction, or a characteristic concentration of the liquid phase $(C)_0$; L - is a characteristic length, in m; ρ-is the density of the phase, in kg/m^3; D - is the mass diffusion coefficient of solute, m^2/s; $\mu=\rho\cdot\nu$ - is the dynamic viscosity of the considered phase, in $Pa \cdot s$; ν-is the kinematic viscosity of the considered phase, m^2/s.

Dealing with solutal surfactant problems the corresponding Marangoni dimensionless number is also called elasticity number and is generally defined accordingly for diffusion and adsorbtion processes. If there are adsorbed surfactants, the product $(\partial\sigma/\partial C)C_0$ can be taken as a coefficient of elasticity in compression of the surfactant monolayer, where C denotes the excess surfactant surface concentration and C_0 is a reference value.

In the solutal Marangoni number can be identified a group presenting dimensions of velocity, called Marangoni velocity:

$$V_{Ma} = \frac{(-\partial\sigma/\partial C) \cdot \Delta C \cdot (d/L)}{\mu} \qquad (18)$$

Where L is the horizontal, lateral extent of the liquid layer and d is the layer depth where there is a difference of concentration ΔC. The ratio d/L represents the coefficient of slenderness of the liquid system and is used mostly in liquid bridges. If it is considered $d=L$, which is acceptable for continuity reasons and equal conditions of comparison, it results:

$$V_{Ma} = \frac{(-\partial\sigma/\partial C) \cdot \Delta C}{\mu} \qquad (19)$$

This is the case of many situations encountered in interfacial mass transfer of surface active solute soluble in immiscible liquid including the systems steel-slags. In order to specify this and to keep the importance of dimension scale, if the solutal Marangoni effect is present on a depth d of the layer, a parameter can be written:

$$\beta = \Delta C/d \qquad (20)$$

Or generally, using cartezian coordinate z instead of d, this became the slope of concentration profile:

$$\beta = \frac{\partial C}{\partial z} \qquad (20')$$

The Marangoni dimensionless number reaches the form:

$$Ma = \frac{(-\partial\sigma/\partial C) \cdot \beta \cdot d^2}{\mu \cdot D} \qquad (21)$$

In this form the Marangoni number represents the ratio between the capillary force due to the surface tension gradient and the viscous drag in the flow.

It is interesting to show that noting:

$$\gamma_{\sigma(c)} = \frac{\partial\sigma(C)/\partial C}{\sigma(C)} \qquad (22)$$

The dimensionless solutal Marangoni number could be written using the form of Ca dimensionless number from rel. (10) in the following form:

$$Ma = \gamma_{\sigma(c)} \cdot \Delta C \cdot Ca^{-1} \qquad (23)$$

Using the form of Ca dimensionless number from rel. (9), the following form is obtained:

$$Ma = \gamma_{\sigma(c)} \cdot \Delta C \cdot Ca \qquad (24)$$

This last relation remembers formally, in a certain measure, to $Ra = \alpha \cdot \Delta T \cdot Ga$ from rel.(16) which refers to buoyancy effect.

The characteristic time scale of the capillarity due to solutal gradient of surface tension is given by:

$$\tau_{Ma} = \left(\frac{\rho \cdot d^3}{|\partial\sigma(C)/\partial C| \cdot \Delta C} \right)^{1/2} \qquad (25)$$

The time scale associated with capillary forces acting at a deformable interface (Laplace force in the normal stress boundary condition) is the following:

$$\tau_{cap} = \left(\frac{\rho \cdot d^3}{\sigma} \right)^{1/2} \qquad (26)$$

It results the ratio:

$$\frac{\tau_{cap}^2}{\tau_{Ma}^2} = \frac{|\partial\sigma(C)/\partial C| \cdot \Delta C}{\sigma(C)} = \gamma_{\sigma(C)} \cdot \Delta C \qquad (27)$$

3. Other possible groups proposed to evaluate particularly the effects of capillarity actions at interface in presence of other physico-chemical and physical actions

A dimensional number called Marangoni coefficient N_{Ma}, in [m^{-2}] was introduced and argued by D. Agble and T.A.Mendes-Tatsis[10] based on a phenomenological approach as having the ability to express, in a quantitative manner, the influence of factors that initiate or inhibit Marangoni convection, when surfactant transfers from an aqueous phase A into an organic phase B. High values of N_{Ma} are obtained in conditions that promote Marangoni convection and smaller values when conditions that inhibit Marangoni convection are prevalent.

It presents a high numerical sensitivity and was proven as being able to predict stability in 29 cases from 30 studied cases, when $N_{Ma} > 10^{-9} m^2$. According to its definition it represents a ratio between the surface tension and its associated effects which produce surface motion and the viscous and related effects that restrict the surface movements:

$$N_{Ma} \propto \frac{\left(\dfrac{d\gamma}{\gamma}\right)d\gamma}{\mu_B D_{AB}\left(RMM_{surfactant}/RMM_{phase}\right)} \cdot$$

$$\frac{C_{surfactant}}{\Gamma} \qquad (28)$$

There is a certain touch of tautology at the numerator in the expression of the Marangoni coefficient N_{Ma} established according to [10], which seems to be due mainly because of the non-linear dependence of the surface tension upon the concentration of the surface active and transferable solute.

Starting from these aspects, but following the philosophy used in forming the Marangoni coefficient, interfacial instability versus stabilization actions could also be well characterized by a new dimensionless number (Ni) introduced in the following paragraphs in this paper for the case of complex effects of capillarity force at a unique length scale in depth and along the interface. It could be derived combining the specific actions involved in the Marangoni dimensionless number and in the Bond dimensionless number (or Weber dimensionless number according to the case), rearranging the specific actions in order to put into evidence the ratio between destabilizing effect of capillarity force (solutal, thermal or both two) due to the gradient of the surface tension, in the form containing the concentration coefficient of the surface/interface tension or the temperature coefficient of the surface/interface tension and the stabilizing effect of interface tension force.

Unfortunately, the total difference from the other dimensionless numbers, made impossible the nomination of this new proposed dimensionless number in other way than it was made in this paper. Otherwise, it is known that nomination of dimensionless numbers using the same basic symbols, even when using sub-scripts, already introduces frequently strong confusions with negative effects in understanding and handling in complex relations. When it is written only for soluto-capillarity effect, the new proposed dimensionless number symbolized (Ni) by the author of the present paper, reach the form:

$$Ni = Ma \cdot Bo =$$

$$= \frac{solutocapillarity\ force}{viscous\ forces} \cdot \frac{gravity\ force}{interface\ tension\ force} =$$

$$= \frac{solutocapillarity\ force}{interface\ tension\ force} \cdot \frac{gravity\ force}{viscous\ forces}$$

$$(29)$$

$$Ni = Ma_{solutal} \cdot Bo = \gamma_{\sigma(C)} \cdot \Delta C \cdot Ga \qquad (30)$$

Replacing the solutocapillarity effect by the thermocapillarity effect an equivalent form could be obtained.

$$Ni = Ma_{thermal} \cdot Bo = \gamma_{\sigma(T)} \cdot \Delta T \cdot Ga \qquad (31)$$

In terms of the corresponding time scales of the included physico-chemical actions, the dimensionless number Ni reaches the following form:

$$Ni = \frac{\tau_{cap}^2 \cdot \tau_{visc} \cdot \tau_{diff}}{\tau_{Ma}^2 \cdot \tau_{grav}^2} \qquad (32)$$

The new dimensionless number could quantify better, the contributions of stabilizing actions versus destabilizing actions at interface between immiscible liquids in conditions when the action of capillarity force (solutal or thermal) prevails over the other physico-chemical or pure physical actions.

The new proposed dimensionless number *Ni* addresses sharp interfaces, evaluating separately in each phase the possibilities of instability to occur in established conditions. This is possible if a convenient length scale is established for all physico-chemical actions. Also, it allows a computation of the major factor relevant in industrial technology – the characteristic concentration (ΔC) or temperature (ΔT) which could vary or could be modified by different internal or external processes or by different intended actions. This dimensionless number, in the mentioned conditions, leads to a more suggestive comparison between the thermal and solutal capillarity effect because it contains simultaneously both the interfacial tension and the concentration coefficient of this quantity, or after the case the thermal coefficient.

This kind of treating specific problems based on new proposed dimensionless groups is not an isolated one especially when particular cases of flow must be evaluated.

As an example is the dimensionless number Bejan in fluid mechanics and heat transfer representing the dimensionless pressure drop along a channel of length *L* and playing the same role in forced convection as Rayleigh dimensionless number in natural convection [11].

4. Conclusions

Various dimensionless numbers derived from the normal component of the free slip boundary condition present a limited capability to express quantitative aspects at interface involved in hydrodynamic of interface with interfacial tension, because they are simple ratios of separate physical actions. Nevertheless they are able to give a characteristic length scale and time scale if physical factors involved in their computations are well evaluated.

Marangoni dimensionless number, despite useful as proved until now in many cases, presents the major difficulties in obtaining results of high degree of validity and generality because it does not include the effects due to the presence of gravity as state and of interfacial tension, both exerting stabilizing effects.

Proposal of the dimensional number under the form of Marangoni coefficient, besides the fact it is unusual compared to the requirement and benefits of the dimensionless analysis, it is difficult to be used in other systems than those aqueous-organic, and it takes into account neither the whole panel of physico-chemical actions present at interface, nor a whatever characteristic length scale.

The new proposed dimensionless group $Ni = Ma \cdot Bo$ and its different expressions showed in this paper, exhibits many and improved possibilities to evaluate the occurrence of Marangoni flow and convection.

This new dimensionless number, in one of its computation forms contains the Galilei dimensionless number which introduces a convenient characteristic length scales allowing keeping the interface flat. Also it contains the coefficient expressing the ratio between the product of the characteristic concentration and the concentration coefficient of interfacial tension and the interfacial tension as in the dimensional Marangoni coefficient.

References

[1]. Nita P.S. - Materials Science and Engineering A, 495(2008) 320–325

[2]. Nita P.S. - The Annals of "Dunarea de Jos" University of Galati Fascicle IX Metallurgy and Materials Science 2, 2006, 112-115.

[3]. Ruzicka M.C. - Chemical Engineering Research and Design, 86(8) 2008, 835-868.

[4]. Nita P.S. - The Annals of "Dunarea de Jos" University of Galati Fascicle IX Metallurgy and Materials Science 2 – 2009, ISSN 1453 – 083X

[4]. Nita P.S., Butnariu I, Constantin, N. - Revista de Metalurgia (Madrid), 46, 1(2010), 5-14.

[5]. Mahajan P.M.,Tsige M., Zhang S, Iwan D.A. Jr, Taylor P.L., and Rosenblatt C. - Physical Review Letters 84(2) 2000, 338-341.

[6]. Scriven L.E., Sterling C.V. - Journal of fluid mechanics, 19(1964), 321-340.

[7]. L.R. Weast, Astle D., Beyer W. - CRC Handbook of Chemistry and Physics.(1989-1990), 70th ed. Boca Raton, Florida, CRC Press, Inc.. F-373,376.

[8]. Wagner W. - Wärmeübertragung, 5th revised Edition; Vogel Fachbuch (1998) 119.

[9]. Molerkamp T. - Marangoni convection, mass transfer and microgravity, doctoral thesis, ISBN 90-367-0982-2, Chapter 1 Rijksuniversiteit Groningen, (1998), 6.

[10]. Agble D., Mendes-Tatsis M.A. - International Journal of Heat and Mass Transfer 44 (2001) 1439-1449.

[11]. S. Petrescu - International Journal of Heat Transfer and Mass Transfer, Vol. 37, 1994, p. 1283.

MANUSCRISELE, CĂRŢILE ŞI REVISTELE PENTRU SCHIMB, PRECUM ŞI ORICE CORESPONDENŢE SE VOR TRIMITE PE ADRESA:

MANUSCRIPTS, REVIEWS AND BOOKS FOR EXCHANGE COOPERATION, AS WELL AS ANY CORRESPONDANCE WILL BE MAILED TO:

LES MANUSCRIPTS, LES REVUES ET LES LIVRES POUR L'ECHANGE, TOUT AUSSI QUE LA CORRESPONDANCE SERONT ENVOYES A L'ADRESSE:

MANUSCKRIPTEN, ZIETSCHRITFTEN UND BUCHER FUR AUSTAUCH SOWIE DIE KORRESPONDENZ SID AN FOLGENDE ANSCHRIFT ZU SEDEN:

UNIVERSITATEA "DUNĂREA DE JOS" DIN GALAŢI
REDACŢIA ANALELOR
Str. Domnească nr. 47 – 800036 Galaţi,
ROMÂNIA
email: mbordei@ugal.ro

After the latest evaluation of the journals achieved by National Center for the Science and Scientometry Politics (**CENAPOSS**), as recognition of its quality and impact at national level, the journal is included in B category, 215 code (http://www.cncsis.ro/2006_evaluare_rev.php).
The journal is indexed in Cambridge Scientific Abstract
(http://www.csa.com/ids70/serials_source_list.php?db=materials-set-c).
The papers published in this journal can be visualized on the "Dunarea de Jos" University of Galati site, the Faculty of Metallurgy, Material Science and Environment, page: www.fmsm.ugal.ro.

Annual subscription (4 issues per year)

Edited under the care of
Faculty of
METALLURGY, MATERIALS SCIENCE AND ENVIRONMENT
and Research Center
QUALITY OF MATERIALS AND ENVIRONMENT